Research and development of a new neutrino detector for precise measurement of neutrino-nucleus cross sections

Taichiro Koga
Department of Physics, University of Tokyo

2015/01/12

Abstract

We have been preparing for a new experiment at the J-PARC neutrino beamline to measure the ratio of the charged current cross sections between water and plastic (CH) targets with a large angular acceptance. The main motivation of this new experiment, named WAGASCI, is to reduce the systematic uncertainty of T2K long baseline neutrino experiment. In this thesis, we report R&D of this new detector. We optimize the design of the new detector by using Monte Carlo simulation. Performance of detector components, thin plastic scintillators and new low noise MPPCs, are tested. The performance of the new detector is evaluated by Monte Carlo simulation based on the R&D of the detector components. The event selection criteria are developed to measure the cross sections. The expected number of charged current interaction is 7.23×10^3 per year and the cross section ratio will be measured with a total uncertainty of 3 %. Sensitivity to the neutrino interaction model is checked finally. This detector has a possibility to improve the understanding of the neutrino nucleus interaction and to reduce the associated uncertainties in neutrino oscillation measurements.

Contents

1 Introduction **4**
1.1 Neutrino oscillation 4
1.2 Current status of neutrino oscillation measurement 5
1.3 T2K experiment 6
1.3.1 J-PARC neutrino beam 7
1.3.2 Near detector 8
1.3.3 Far detector 8
1.3.4 Current status and future prospects 9
1.4 Goals of this thesis 10

2 Neutrino interaction with nucleus **12**
2.1 Neutrino interaction with a nucleon 12
2.1.1 Neutrino interaction mode 12
2.1.2 Binding energy and Fermi motion of nucleons 14
2.2 Secondary interaction in nucleus 15

3 New neutrino detector, WAGASCI **18**
3.1 Motivation 18
3.2 Requirements for the WAGASCI 19
3.3 Basic concept of the new detector 19
3.4 Neutrino flux and interaction at a candidate site of the WAGASCI 22
3.4.1 Neutrino flux at the candidate site 22
3.4.2 Neutrino interaction at the candidate site 23
3.5 Optimization of the detector 28
3.5.1 Size of target 28
3.5.2 Optimization of arrangement of H_2O and CH target . . 29
3.5.3 Size of the MRDs 32
3.6 Optimization of scintillators 36
3.6.1 Scintillators inside the central detector 36
3.6.2 Scintillators in the MRDs 37

3.6.3 Scintillators around the target 37
3.6.4 Summary of the design of the detector 38

4 Performance test of the detector components 40
4.1 Detector components of the WAGASCI 40
4.2 Performance test of MPPC 43
4.3 Performance test of the scintillator 45
4.3.1 Setup 45
4.3.2 Result of measurements of the 3.0 mm thickness scintillator 46
4.3.3 Summary 51

5 Expected performance of the detector 53
5.1 Detector simulation 53
5.1.1 The central detector 53
5.1.2 MRDs 55
5.1.3 Scintillator, wavelength shifting fiber and MPPC . . . 55
5.1.4 Experimental hall 55
5.1.5 Summary of parameters in the simulation 55
5.2 Track reconstruction 57
5.2.1 Two dimensional track reconstruction 57
5.2.2 Track matching with MRD and TOF plane 58
5.2.3 Three-dimensional track matching 58
5.3 Signal and background 58
5.4 Event selection 59
5.4.1 Vertexing 59
5.4.2 Short track search 59
5.4.3 Track direction cut 60
5.4.4 Fiducial volume cut 60
5.4.5 Iron plates cut 60
5.5 Summary of the event selection 61
5.5.1 Vertex 62
5.5.2 Reconstructed angle 62
5.5.3 Number of penetrating iron plates 62
5.5.4 Muon identification 65
5.5.5 Muon tagging efficiency 66

6 Cross section measurement and sensitivity to neutrino interaction model 67
6.1 Charged current cross section measurement 67
6.1.1 Charged current cross section on hydrocarbon 67

6.1.2 Charged current cross section on water 68
6.1.3 Sensitivity to neutrino interaction model 70
6.2 Charged current cross section ratio measurement 74
6.2.1 Estimation of error 74
6.2.2 Sensitivity to neutrino interaction model 76
6.3 Exclusive-channel measurement 81
6.3.1 Charged current quasi-elastic interaction measurement 81
6.3.2 future prospects 83

7 Summary and future prospects 86
7.1 Summary 86
7.2 Future prospects 86

A Flux and background measurement at the candidate site 90
A.1 INGRID 90
A.2 Data taking 91
A.3 Comparison between data and simulation 92

B Performance test of the sample of the new MPPCs 99
B.1 Gain 99
B.2 Dark noise rate 101
B.3 Crosstalk rate 105
B.4 Afterpulse rate 105
B.5 Photo detection efficiency 107
B.6 Comparison of performance 108

Chapter 1

Introduction

1.1 Neutrino oscillation

A neutrino is a neutral lepton. Three types of neutrinos are known to exist: electron neutrino (ν_e), muon neutrino (ν_μ), tau neutrino (ν_τ) and their antiparticles. The standard model of elementary particles assumes that mass of the neutrinos is zero and there is no mixing of the flavor. However, the discovery of the neutrino oscillation [1] shows that the assumption is incorrect. It indicates the existence of new physics beyond the standard model. The measurement of the neutrino oscillation will provide us with important information in order to investigate the origin of flavor.

Assuming that the neutrinos have non zero mass and their eigenstates of weak interaction, $|\nu_\alpha\rangle$ ($\alpha = e, \mu, \tau$), and mass eigenstates, $|\nu_i\rangle$ ($i = 1, 2, 3$), are mixed as follows:

$$|\nu_\alpha\rangle = \sum_i U_{\alpha i} |\nu_i\rangle \tag{1.1}$$

where $U_{\alpha i}$ is an element of 3×3 unitary matrix called Maki-Nakagawa-Sakata (MNS) matrix [2], given as follows:

$$\begin{aligned} U &= \begin{pmatrix} 1 & 0 & 0 \\ 0 & c_{23} & s_{23} \\ 0 & -s_{23} & c_{23} \end{pmatrix} \begin{pmatrix} c_{13} & 0 & s_{13}e^{-i\delta_{CP}} \\ 0 & 1 & 0 \\ -s_{13}e^{i\delta_{CP}} & 0 & c_{13} \end{pmatrix} \begin{pmatrix} c_{12} & s_{12} & 0 \\ -s_{12} & c_{12} & 0 \\ 0 & 0 & 1 \end{pmatrix} \\ &= \begin{pmatrix} c_{12}c_{13} & s_{12}c_{13} & s_{13}e^{-i\delta_{CP}} \\ -s_{12}c_{23} - c_{12}s_{13}s_{23}e^{i\delta_{CP}} & c_{12}c_{23} - s_{12}s_{23}s_{13}e^{i\delta_{CP}} & c_{13}s_{23} \\ s_{12}s_{23} - c_{12}s_{13}c_{23}e^{i\delta_{CP}} & -c_{12}s_{23} - s_{12}s_{23}s_{13}e^{i\delta_{CP}} & c_{13}c_{23} \end{pmatrix} \end{aligned} \tag{1.2}$$

where $c_{ij}(s_{ij})$ mean $\cos\theta_{ij}$ ($\sin\theta_{ij}$). θ_{ij} are mixing angles and δ_{CP} is a CP

phase. The probability of the neutrino oscillation after traveling the distance L is calculated by using Eq. 1.2 and Schrödinger equation.

$$\begin{aligned} P(\nu_\alpha \to \nu_\beta) = \delta_{\alpha\beta} \quad &- \quad 4\sum_{i>j} Re(U^*_{\alpha i}U_{\beta i}U_{\alpha j}U^*_{\beta j})\sin^2\left(\frac{\Delta m^2_{ij}L}{4E}\right) \\ &- \quad 2\sum_{i>j} Im(U^*_{\alpha i}U_{\beta i}U_{\alpha j}U^*_{\beta j})\sin\left(\frac{\Delta m^2_{ij}L}{2E}\right) \end{aligned} \tag{1.3}$$

where E is energy of the neutrino and $\Delta m^2_{ij} = m^2_i - m^2_j$. The existence of neutrino oscillation indicates non zero Δm^2_{ij} and existence of flavor mixing.

1.2 Current status of neutrino oscillation measurement

Each parameter of the MNS matrix and Δm^2 have been measured by neutrino oscillation experiments. The measured values are as follows [3].

θ_{12} and Δm^2_{21}

These parameters are measured by solar neutrino measurements and a reactor experiment, KamLAND [4]. The best fit values are $\sin^2 2\theta_{12} = 0.846 \pm 0.021$, $\Delta m^2_{21} = (7.53 \pm 0.18) \times 10^{-5} eV^2$.

θ_{23} and $|\Delta m^2_{32}|$

These parameters are measured by atmospheric neutrino measurement, Super-Kamiokande [5] and accelerator measurements, MINOS [6] and T2K [7]. The best fit values are $\sin^2 2\theta_{23} = 0.999^{+0.001}_{-0.018}$, $\Delta m^2_{32} = (2.44 \pm 0.06) \times 10^{-3} eV^2$ (normal hierarchy) and $\sin^2 2\theta_{23} = 1.000^{+0.000}_{-0.017}$, $\Delta m^2_{32} = (2.52 \pm 0.07) \times 10^{-3} eV^2$ (inverted hierarchy).

θ_{13}

θ_{13} is measured by reactor experiments, Daya Bay [8], Double Chooz [9] and RENO [10]. It is also measured by T2K [11]. The best fit value is $\sin^2 2\theta_{13} = (9.3 \pm 0.8) \times 10^{-2}$.

δ_{CP}

By combining the result of T2K and reactor experiments, it is limited with 90% confidence level and the excluded region is 0.19π–0.80π (normal hierarchy) and -π– -0.97π, -0.04π–π (inverted hierarchy) [11]. δ_{CP} can generate CP effects in the neutrino oscillation due to the non zero θ_{13}. δ_{CP} can be a key of a creation of matter dominant universe and it is important to measure δ_{CP}.

1.3 T2K experiment

T2K (Tokai to Kamioka) experiment is a long baseline neutrino oscillation measurement, started from 2009 [12]. The ν_μ beam produced by J-PARC in Tokai is detected by near detector (ND280) and far detector (Super-Kamiokande) to measure the probability of $\nu_\mu \to \nu_e$ appearance and $\nu_\mu \to \nu_\mu$ disappearance. The first-order approximate formula of the oscillation probabilities are given as follows:.

$$P(\nu_\mu \to \nu_e) = \sin^2 2\theta_{13} \sin^2 \theta_{23} \sin^2\Big(\frac{\Delta m^2_{31} L}{4E}\Big) \tag{1.4}$$

$$P(\nu_\mu \to \nu_\mu) = 1 - \sin^2 2\theta_{23} \sin^2\Big(\frac{\Delta m^2_{32} L}{4E}\Big) \tag{1.5}$$

The T2K experiment measures the mixing angles θ_{13}, θ_{23} and Δm^2_{32} by measuring these probabilities of the oscillation. In addition, $\overline{\nu}_\mu$ is produced to measure the probability of $\overline{\nu}_\mu \to \overline{\nu}_e$ appearance and $\overline{\nu}_\mu \to \overline{\nu}_\mu$ disappearance. The CP phase δ_{CP} is measured by the comparison between $P(\nu_\mu \to \nu_e)$ and $P(\overline{\nu}_\mu \to \overline{\nu}_e)$.

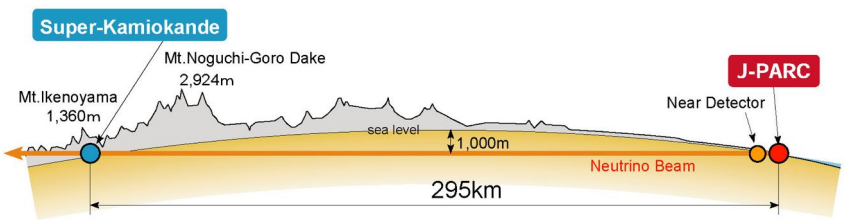

Figure 1.1: View of the T2K experiment [13]

1.3.1 J-PARC neutrino beam

J-PARC proton accelerator consists of three accelerators: a 400 MeV linear accelerator (LINAC), a 3GeV rapid cycling syncrotron (RCS) and a 30 GeV main ring synchrotron (MR).

To create the neutrino beam, 30 GeV protons are extracted from the synchrotron ring to strike a graphite target. Emitted pions are focused by three electromagnetic horns. The pions decay in a 96 m decay volume and produce a neutrino beam. The beam is aimed 2.5° away from the target to the far detector axis to optimize the neutrino energy spectrum. This configuration produces a narrow band beam by the kinematics of pion decays. The angle is set so that the spectrum has a peak at the first oscillation maximum, around 600MeV, as shown in Fig. 1.2.

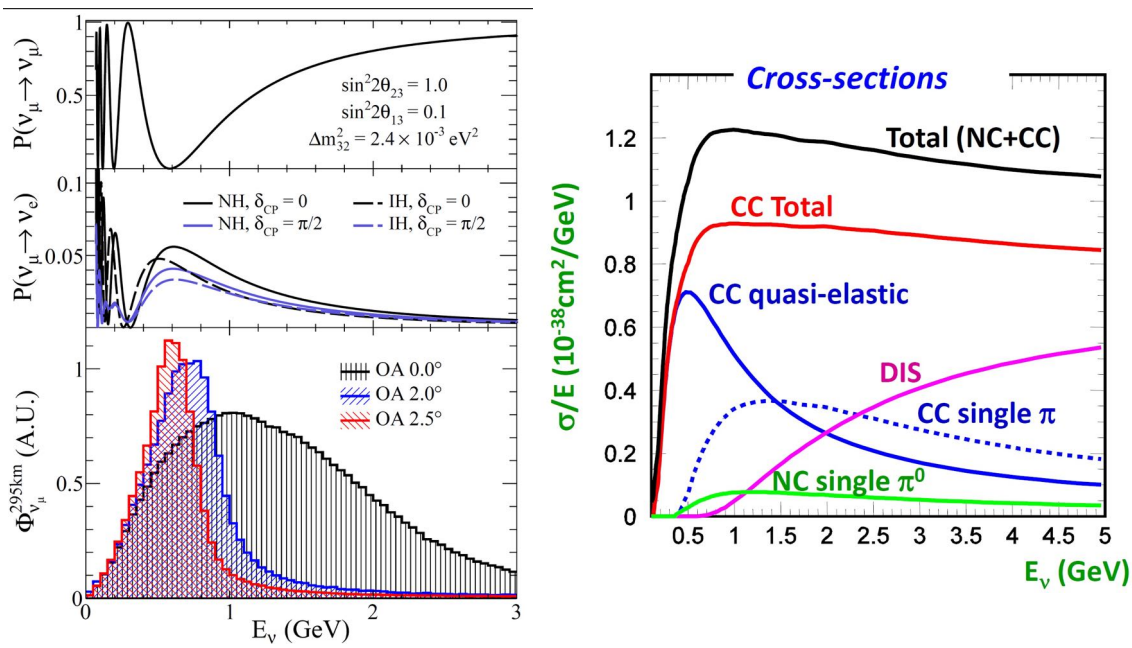

Figure 1.2: The probability of the oscillation and the muon neutrino spectrum (left). The cross section of the neutrino interaction is also shown (right). [14, 15]

The neutrino events which interact in charged current quasi elastic (CCQE, $\nu_l + n \to l + p$, l means a charged lepton) mode are selected at the far detector as a signal. As shown in Fig. 1.2, the main interaction mode at below 1GeV is CCQE and other modes can be reduced by off-axis method.

1.3.2 Near detector

There are two near detectors, on axis and off-axis detectors, as shown in Fig. 1.3. The on axis near detector, INGRID and Proton Module [16], measure the neutrino event rate and the direction of the neutrino beam. INGRID is composed of 16 modules and one module is composed of a sandwich structure of 9 iron plates and 11 plastic scintillator planes, as shown in Fig. 1.4. Proton Module is composed of 24 plastic scintillator planes and placed in the upstream of INGRID.

They also measure the neutrino cross section with iron and plastic and their ratio for study of the neutrino interaction. They succeed to measure the cross section ratio with an accuracy of 3.3% and check the nuclear effect for iron and hydrocarbon targets [16]. The uncertainty of the neutrino flux is canceled by taking ratio and such a high precision is achieved.

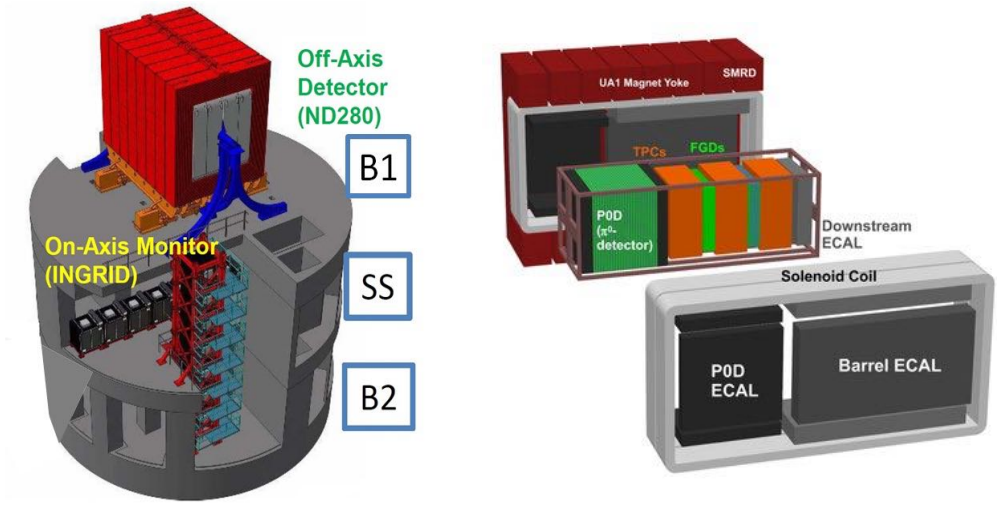

Figure 1.3: Place of the near detectors (left) and an exploded view of the ND280 (right) [17].

The off-axis near detector, ND280 (Near Detector at 280 m from production target) [17], measures the neutrino event rate and the cross section of the neutrino interaction. It consists of several detectors inside the magnet, as shown in Fig. 1.3. Its main target material is hydrocarbon and it detects mainly forward scattering muons produced by neutrino interaction.

1.3.3 Far detector

The far detector, Super-Kamiokande [18], consists of 50kt water target and 11,200 20-inch photo multiplier tubes (PMT) for the inner detector and 1185

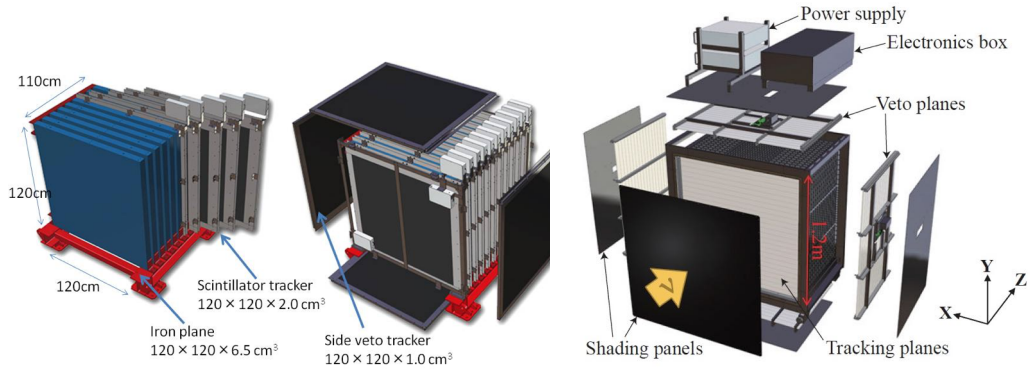

Figure 1.4: Schematic view of the INGRID (left and middle) and Proton Module (right) [16]

8-inch PMTs for veto. It measures the neutrino by detecting Cherenkov light emitted by a charged lepton produced in the neutrino interaction with water. The 20-inch PMTs cover inside the inner tank and realize the angular acceptance of 4π.

Figure 1.5: A schematic view of the Super-Kamiokande [19]

1.3.4 Current status and future prospects

The T2K experiment observes the ν_e appearance more than 7.3 σ significance [11]. A part of the parameter space of the CP phase δ_{CP} is excluded

with 90% confidence level by combining the result of the T2K and the reactor experiments for the first time in the world [20].

In addition, the current measured value of the mixing angle $\sin^2\theta_{23} = 0.514^{+0.055}_{-0.056}(0.511 \pm 0.055)$, measured by the ν_μ disappearance assuming normal (inverted) hierarchy, is the most strongest limit [7].

T2K will aim for the more precise measurement of the neutrino oscillation. In addition to reducing the statistical uncertainty with more data, the reduction of systematic uncertainty will become important. Table 1.1 shows the systematic errors in T2K oscillation measurement [21]. The largest component is the uncertainty of the neutrino cross section due to the difference of the nuclear targets between hydrocarbon and water. In addition, the near detector can measure mainly forward scattering events while far detector has 4π angular acceptance. The difference of the acceptance also contributes to the systematic errors. For the precise neutrino oscillation measurement, it is important to reduce these systematic errors. In order to reduce the systematic errors, the analysis of T2K near detector data is being improved to provide the cross section measurement such as the neutrino cross section on water and high scattering angle events.

Table 1.1: Summary of the systematic errors in T2K experiment [21]

		ν_μ sample	ν_e sample
ν flux and cross section	w/o ND measurement	21.8%	26.0%
		2.7%	3.1%
ν cross section due to the difference of nuclear target, water and hydrocarbon		5.0%	4.7%
Final or secondary hadronic interaction		3.0%	2.4%
Super-K detector		4.0%	2.7%
Total	w/o ND measurement	23.5%	26.8%
		7.7%	6.8%

1.4 Goals of this thesis

In order to reduce the systematic errors in the T2K experiment, we propose a new experiment at the J-PARC neutrino beamline to measure the ratio of the charged current cross sections between water and plastic (CH) targets with a large angular acceptance, based on the measurement with the Proton Module and INGRID. In this thesis, we report R&D of this new detector. We

optimize the design of the new detector by using Monte Carlo simulation. Detector components, thin plastic scintillators and new low noise MPPCs are tested. The performance of the new detector is evaluated by Monte Carlo simulation based on the result of the R&D of the detector component. The event selection criteria are developed to measure the cross sections and sensitivity to the neutrino interaction model is checked.

Chapter 2

Neutrino interaction with nucleus

In order to interpret the neutrino data, a modeling of neutrino interaction is indispensable. In the energy region of T2K experiment, around a few hundread MeV to one GeV, impulse approximation can be assumed and we can deal with neutrino interaction with a nucleus by two steps. First, neutrino interacts with a nucleon in a target nucleus by exchanging weak bosons in several modes and produce secondary particles. Second, the secondary particles interact with the nucleons in nucleus.

2.1 Neutrino interaction with a nucleon

2.1.1 Neutrino interaction mode

Figure 2.2 shows the neutrino interaction mode. The modes exchanging a W boson is called charged current interaction (CC). In CC, a charged lepton is produced, corresponding to the flavor of the neutrino. CC is separated into several interaction modes as follows:

CCQE

Charged current quasi elastic interaction (CCQE, $\nu_l + n \rightarrow l + p$, l is e or μ) is main interaction in the energy region of T2K. It is signal of T2K because it is two body scattering and the neutrino energy is reconstructed by the momentum of charged lepton and initial direction of the neutrino under an assumption that a target nucleon is at rest.

As shown in Fig. 2.1, the T2K near detector mainly detects forward scattering muons and predicts the neutrino energy spectrum at the far detector.

It may bias the result because the acceptance of the far detector is 4π. The large scattering angle muons are extrapolate by using neutrino interaction model and their uncertainty is estimated by changing the parameters of the model. Then, it is also important to check the reliability of the model. If CCQE is measured with a large acceptance, it can validate the model.

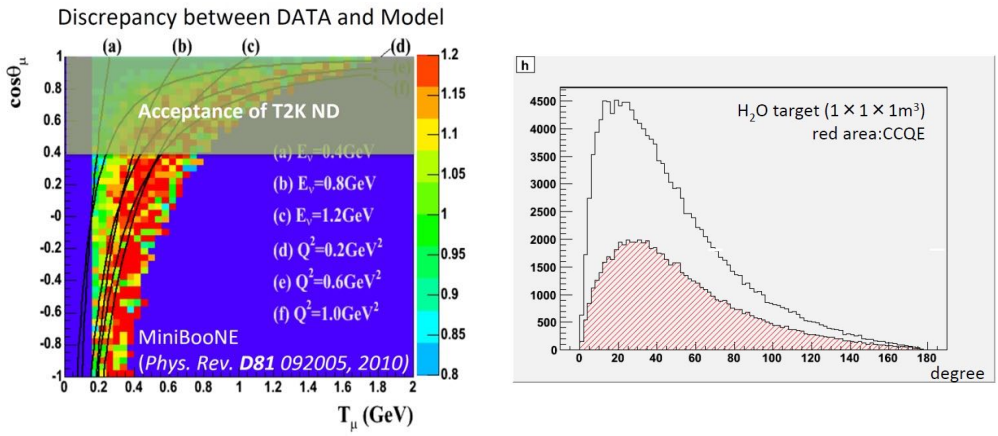

Figure 2.1: Discrepancy between observed CCQE like events and model in MiniBooNE experiment (left). Horizontal is muon kinetic energy and vertical is muon scattering angle. Gray part is an acceptance of T2K near detector. Right plot is scattering angle of produced muons in CC (black line) and CCQE (hatched).

CC1π

In charged current single π interaction (CC1π, $\nu_l + N \rightarrow l + N' + \pi$), a pion is produced. In interaction model, the production is mainly due to baryon resonance, mainly Δ. It can be main background when we select CCQE if the pion or proton are not reconstructed. Cross section of the produced pion with nucleons in nucleus is large and it often causes secondary interaction.

CCcoh

In charged current coherent pion production (CCcoh, $\nu_l + N \rightarrow \nu_l + N' + \pi_+$), a neutrino interacts with entire nucleus and produce a pion without changing state of the nucleus. The cross section is small for the neutrino energy below 1 GeV as the result of K2K and SciBooNE experiment. In T2K oscillation analysis, 100% uncertainty of the normalization of the CC coherent interaction is assumed because CCcoh can not be implemented by

an simple model for high energy neutrino interaction. In CCcoh, muons mainly have small scattering angle.

CCDIS, CCmultiπ

In charged current deep inelastic scattering (CCDIS, $\nu_l + N \rightarrow l + N' + hadrons$) and charged current multi π (CCmulti, $\nu_l + N \rightarrow l + N' + multipions$), many hadrons are produced. Their cross section is also small for the neutrino energy below 1 GeV.

The modes exchanging a Z boson is called neutral current interaction (NC). NC does not produce charged lepton. NC interaction can be background when we select CC.

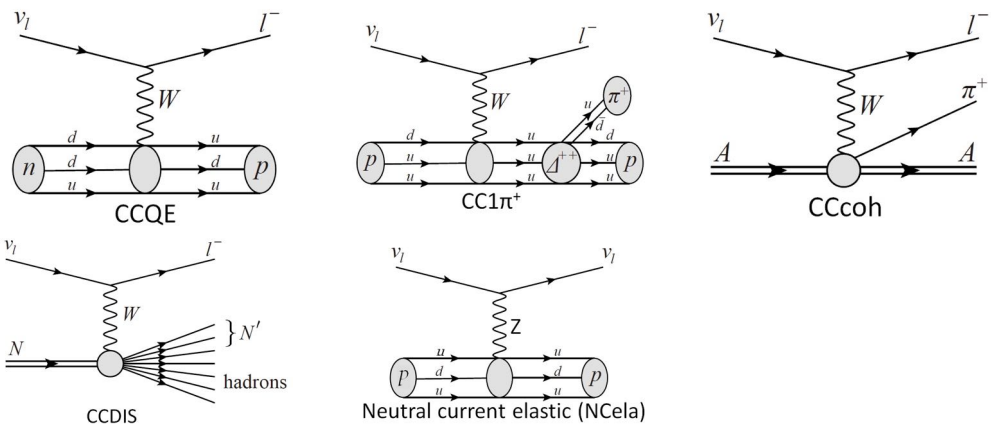

Figure 2.2: Neutrino interaction mode with a nucleon [19]

2.1.2 Binding energy and Fermi motion of nucleons

The neutrino cross section with a nucleon depends on the kind of the target nucleus because the momentum and binding energy of the nucleon in nucleus are different. There are some models to describe the momentum distribution.

The relativistic Fermi gas model (RFG) is a common and the most simplest model across Fermionic physical systems. The assumption is that all nucleons are in a potential and all states is filled up to a Fermi-level, above which no states are filled. This gives a flat distribution of states in momentum space and a constant binding energy, as shown in Fig. 2.3.

The spectral function (SF) is more complicated model. Momentum and removal energy of nucleons are reconstructed to duplicate an electron scattering data. The spectral function used in T2K is provided by O.Benhar. [22, 23]

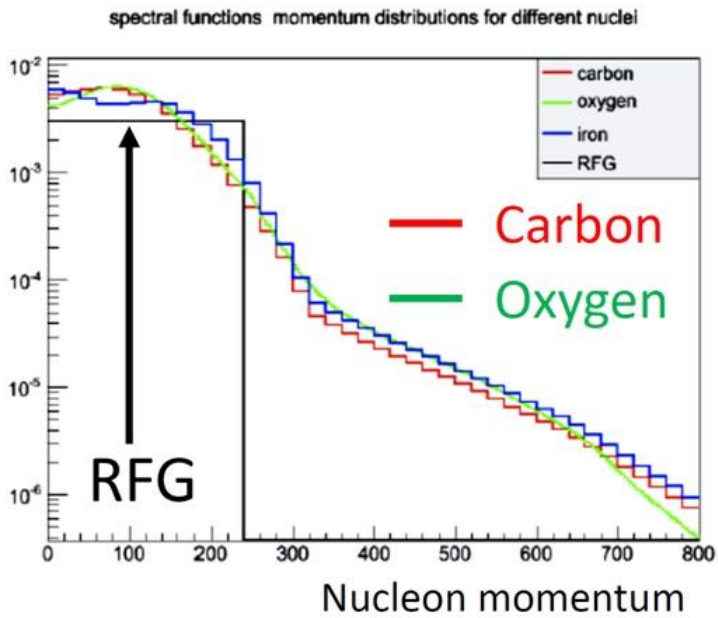

Figure 2.3: Momentum distribution of nucleons in nucleus [15]

Figure 2.4–2.5 (2.6–2.7) show the muon momentum and scattering angle distribution on H_2O (CH) target with each model. Both H_2O and CH, there is about 10% difference of the cross section between RFG and SF in forward scattering. No measurement has measured the neutrino cross section on H_2O with the accuracy of lower than ten percent and it is difficult to evaluate their effect precisely by existing data.

In the T2K oscillation analysis, the error of the nucleon momentum distribution model is assigned from the difference between the two models. No correlation is assumed between near and far detector and the uncertainty is not canceled. It is one of the dominant systematic errors and the size of the error strongly depends on their systematic treatment [21].

2.2 Secondary interaction in nucleus

As shown in Fig. 2.8, the secondary particles interact with the nucleons in nucleus. It depends on the number of the nucleons in nucleus and their state, so it also depends on the kind of the target nucleus. The produced charged lepton is almost unaffected. The number and momentum of the produced pions and protons emitted from the nucleus is changed by this effects. The

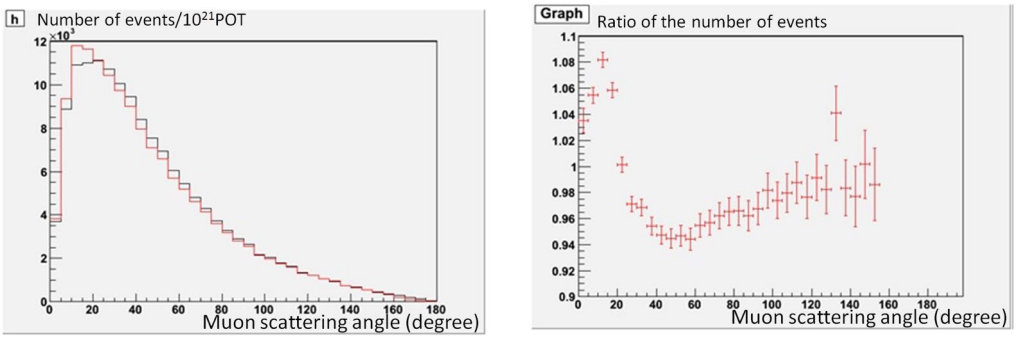

Figure 2.4: Scattering angle of produced muons on H_2O target (left) in the case of RFG (black) and SF (red) and their ratio (right). Error bar is the statistic of MC.

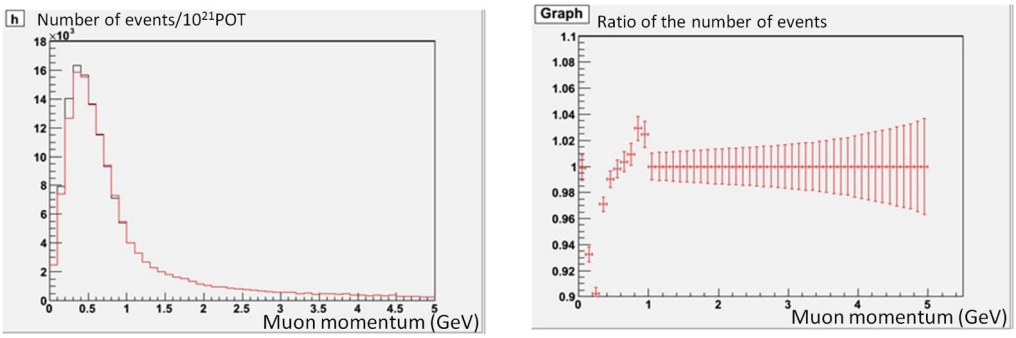

Figure 2.5: Momentum of muons on H_2O target (left) in the case of RFG (black) and SF (red) and their ratio (right). Error bar is the statistic of MC.

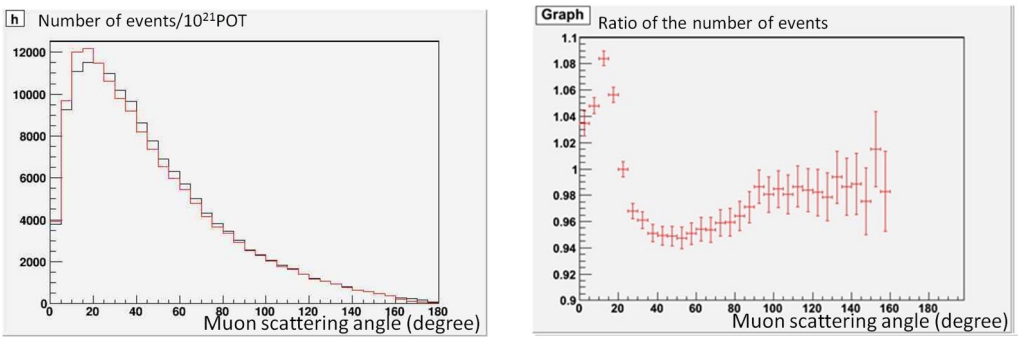

Figure 2.6: Scattering angle of muons on CH target (left) in the case of RFG (black) and SF (red) and their ratio (right). Error bar is the statistic of MC.

secondary interactions make it difficult to identify the interaction modes.

Many neutrino cross sections with nucleus have been measured recently,

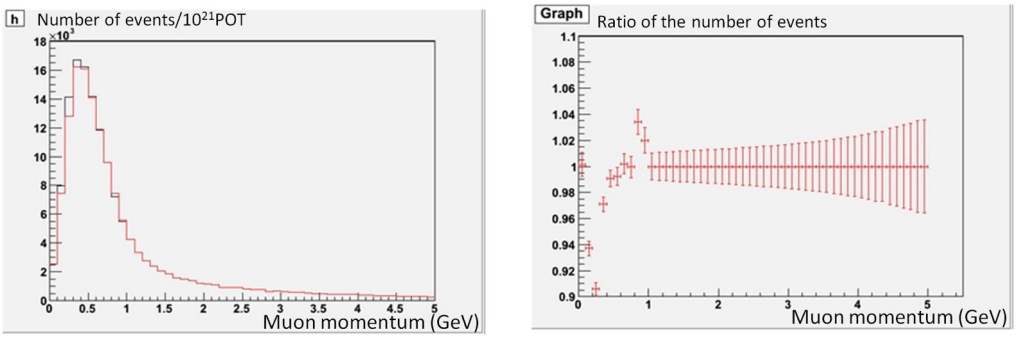

Figure 2.7: Momentum of muons on CH target (left) in the case of RFG (black) and SF (red) and their ratio (right). Error bar is the statistic of MC.

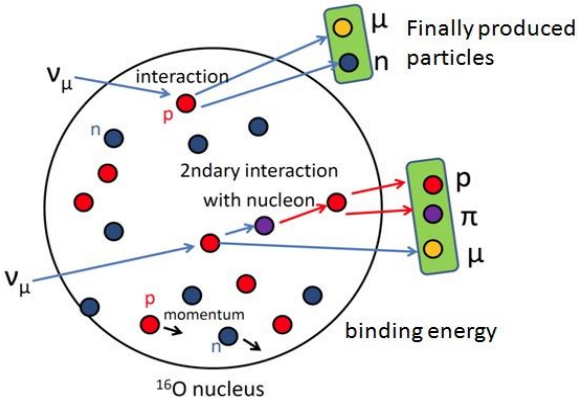

Figure 2.8: Neutrino interaction with nucleus

however, in many case the accuracy of the measurements is more than 10% due to the neutrino flux uncertainty. The current models predict that the effect of the difference of the kind of the target nucleus is small, so it is difficult to validate the model by the current result of the measurement. The energy range of the neutrino beam and kind of the target is different in each experiment and that also makes it difficult to validate the model in the case of the T2K.

Chapter 3

New neutrino detector, WAGASCI

3.1 Motivation

In order to reduce the systematic errors in the T2K experiment, we propose a new experiment at the J-PARC neutrino beamline to measure the ratio of the charged current cross sections between water and plastic (CH) targets with a large angular acceptance.

The absolute cross section measurements suffer from the uncertainty of the neutrino flux which is more than ten percent. However, by taking the ratio of the cross sections between different targets at the same position, we can cancel these uncertainties and achieve a precision of a few percents, as demonstrated by the measurement with the Proton Module and INGRID [16]. It enables us to validate the difference between H_2O and CH. The measurements with large angular acceptance are also important to validate the neutrino interaction model and compare the model and the measurement of the T2K and other experiments. The neutrino interaction model can be compared with precise data and constrained by this measurement.

The name of the project is WAGASCI (WAter Grid And SCIntillator detector) experiment. What we want to measure is as follows:

1. Total charged current cross sections on H_2O and CH and their ratio.

2. Their differential cross section and their ratio as a function of the muon momentum and scattering angle

3. Their exclusive cross section and their ratio, for example, CCQE.

3.2 Requirements for the WAGASCI

Requirements for the new detector are as follows.

1. The neutrino flux in the WAGASCI is as similar as possible to that in the T2K near and far detectors.

2. Enough statistics to measure the cross section ratio with one year run, corresponding to 3×10^{20} protons on target (POT). More than 3×10^{4} charged current interaction should take place per one year.

3. Enough statistics to measure the differential cross section ratio for 1×10^{21}POT run with a large acceptance. More than 1×10^{3} muons are detected per 10 degrees, around 90 degrees.

4. Muons momenta is measured with the accuracy of 10%, up to 1GeV/c.

5. The difference of the neutrino flux, structure of the detector, and detection efficiency between H_2O target part and CH target part is as small as possible to reduce the systematic uncertainty in the ratio measurements.

6. Background events such as cosmic rays and neutrino interaction with wall are rejected.

7. The total number of readout channels is less than 10000.

3.3 Basic concept of the new detector

Figure 3.1 shows a basic concept of the new detector. Muon range detectors (MRDs) composed of a sandwich structure of iron plates and plastic scintillators are placed around a target detector to detect neutrino interaction. A central detector contains the neutrino target materials, water and hydrocarbon, and plastic scintillator bars. When neutrinos interact with the target, secondary particles are generated. Neutrino interactions are identified by detecting tracks of the secondary charged particles through plastic scintillator bars. Muons are identified and their momenta are measured by MRDs. The main background is considered to be particles generated in neutrino interactions with MRDs and the wall of the detector hall. They are rejected by the time of flight (TOF) between the central detector and MRDs.

In the target region, thin plastic scintillators are used to reduce the fraction of non-water materials. They are aligned in a 3D grid like structure as shown in Fig. 3.2. Spaces between scintillators are filled with the

neutrino target materials, water or hydrocarbon cubes. This structure allows us to reconstruct a high angle track and obtain large acceptance. The scintillation light from the scintillators is collected by a wavelength shifting fiber and measured by a semiconductor photo detector, Multi-pixel Photon Counter(MPPC). The wavelength shifting fiber makes the attenuation length of the scintillation light longer. A new MPPC, which has low noise and high photo detection efficiency, is used to measure the low light yield of the thin plastic scintillator.

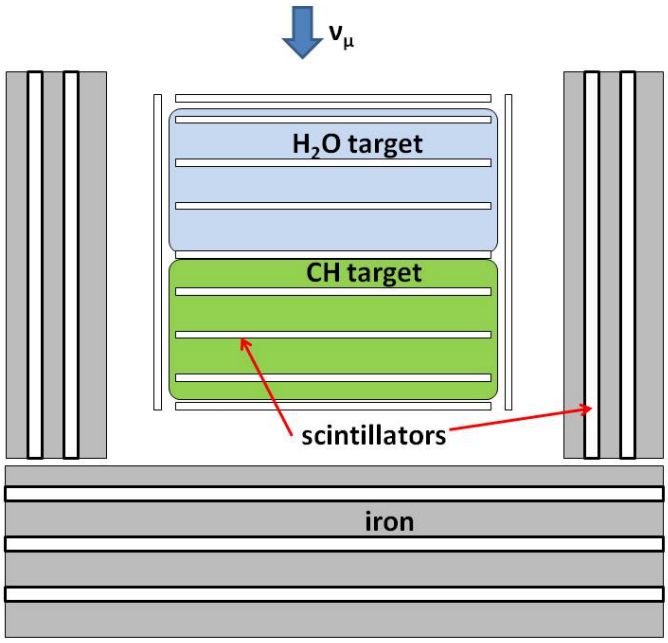

Figure 3.1: Schematic view of the new detector

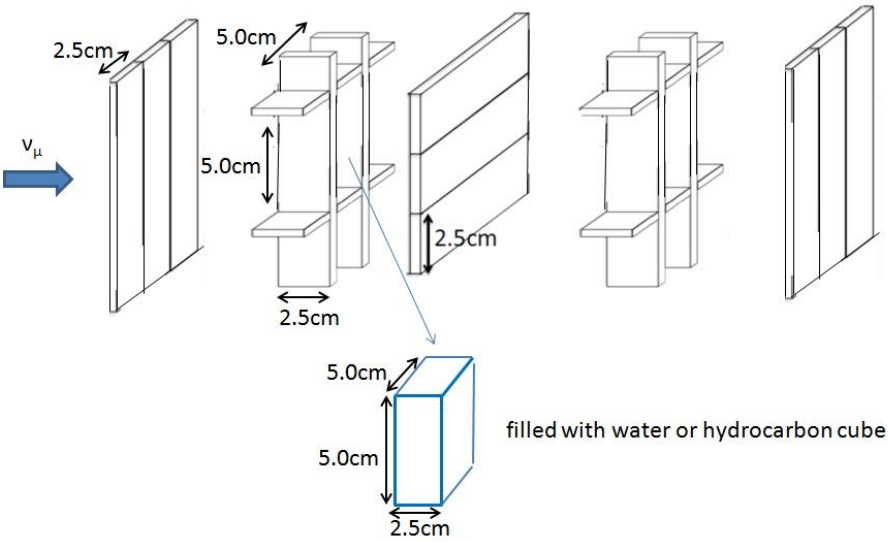

Figure 3.2: Schematic view of the scintillators inside the central detector

3.4 Neutrino flux and interaction at a candidate site of the WAGASCI

First, the neutrino flux and neutrino interaction rate are checked at a candidate site of the WAGASCI.

3.4.1 Neutrino flux at the candidate site

The candidate site of the WAGASCI experiment is the B2 floor of the T2K near detector hall at J-PARC, as shown in Fig. 3.3. The coordinate system is defined as shown in the right picture and the neutrino beam is injected along with z-axis. The expected neutrino flux at the candidate site is predicted by using a Monte Carlo simulation library, named JNUBEAM [24]. JNUBEAM is used to simulate the neutrino beam line in the T2K experiment. It simulates the collision of the primary proton beam with the graphite target, focussing of the secondary particles with the three electromagnetic horns, and the decay of them. It predicts the flux of the neutrino beam in each flavor at any place.

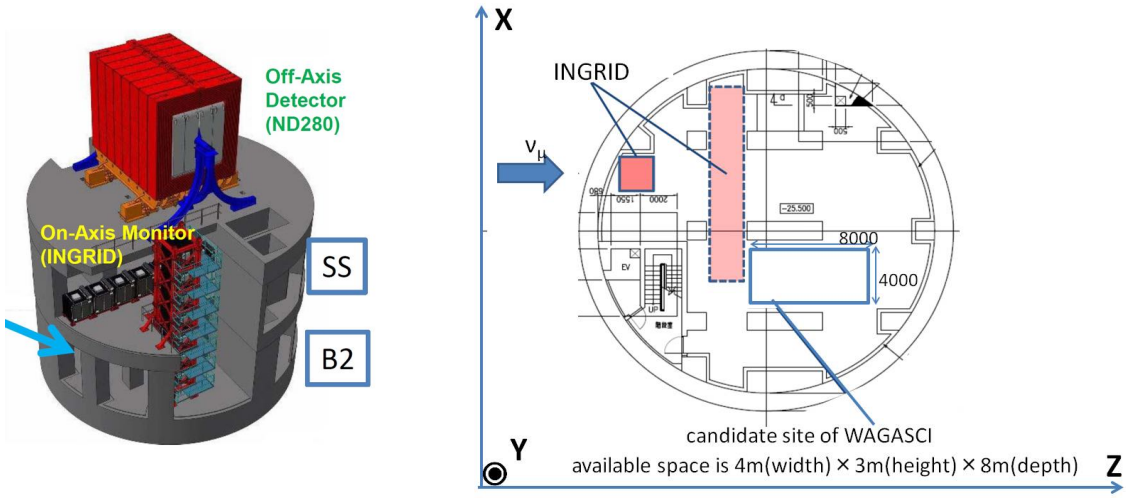

Figure 3.3: Candidate site of the WAGASCI. Right picture is a top view of the B2 floor of the T2K near detector hall.

Figure 3.4 shows the expected muon neutrino flux per 10^{21} protons on target (POT) at the candidate site of the WAGASCI and the T2K near detector. Both of the spectra have a peak around 600 MeV. The off-axis angle is 1.6 degrees at the candidate site and the T2K off-axis angle is 2.5

degrees. The position of the target is set to minimize the difference of the off-axis angles.

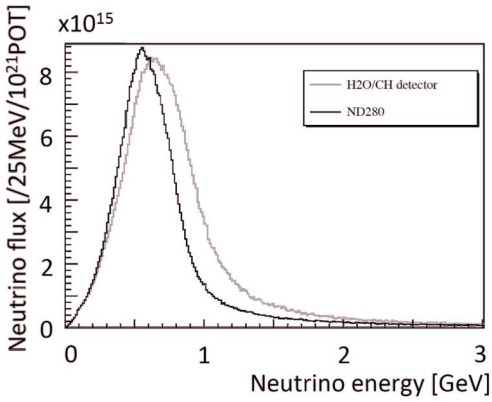

Figure 3.4: Expected neutrino flux at the candidate site of WAGASCI(gray line) and at T2K near detector(black line)

Figure 3.5 and Table 3.1 show the expected neutrino flux in each flavor per 1×10^{21} POT at the candidate site of the WAGASCI. Most of the neutrinos are muon neutrinos.

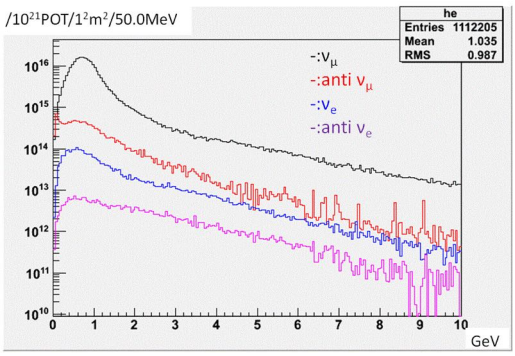

Figure 3.5: Expected neutrino flux at the candidate site of the WAGASCI

3.4.2 Neutrino interaction at the candidate site

The neutrino interaction with H_2O and CH target is predicted by NEUT [25]. NEUT is used to simulate the neutrino interaction with a target nucleus. It simulates the neutrino interaction with a target nucleon and behavior of the

Table 3.1: Expected neutrino flux at the candidate site of the WAGASCI

flavor	ν_μ	$\overline{\nu_\mu}$	ν_e	$\overline{\nu_e}$
$/10^{21}$POT/1m^2	2.67×10^{17}	1.42×10^{16}	2.79×10^{15}	3.21×10^{14}
fraction	93.9%	5.0%	1.0%	0.1%

secondary particles within a nucleus. It predicts the neutrino interaction rate and the kinematics of secondary particles emitted from nucleus by using the information of the neutrino flux given by the JNUBEAM as an input.

Table 3.2 shows the neutrino interaction event rates with 1ton H_2O target in each flavor. Fraction of the muon neutrino is more than 96% for all neutrino interaction. Hereafter, only the muon neutrino interaction is simulated.[1]

Table 3.2: Expected neutrino interaction rate at the candidate site of WAGASCI with 1ton H_2O target

flavor	ν_μ	$\overline{\nu_\mu}$	ν_e	$\overline{\nu_e}$
events/10^{21}POT/1ton	2.07×10^5	4.83×10^3	3.11×10^3	2.22×10^2
fraction	96.2%	2.2%	1.5%	0.1%

Table 3.3 shows the number of muon neutrino interaction events in each interaction mode per 10^{21} POT with 1ton H_2O and CH target at the candidate site. Figure 3.6 shows energy of interacted muon neutrinos in each interaction mode with 1ton H_2O and CH target at the candidate state. As a result of the simulation, there is no big difference for the event rate between H_2O and CH target. Hereafter, only interaction with H_2O is used for the optimization of the detector.

In WAGASCI experiment, neutrino interactions are identified by detecting muons. The design of the detector is optimized by momentum and angular distribution of muons. Figure 3.7 shows the momentum and scattering angle of the muons produced by charged current interaction. 1.48×10^5 muons are produced. The peak of the momentum is around 500MeV. As shown in Figure 3.7, 60% of muons have scattering angle less than 45 degrees. The scattering angle of 38% of muons are more than 45 degrees and less than 135 degrees while 2% muons are more than 135 degrees.

Figure 3.8 shows the kinetic energy of muons in each scattering angle. A part of the forward scattering muons have more than 1 GeV of energy.

[1] $\overline{\nu}_\mu and \nu_e$ are not negligible background, but it has not been studied.

Table 3.3: Expected neutrino interaction rate per 10^{21} POT with 1ton H_2O and CH target at the candidate site of WAGASCI. (%) is the fraction of each interaction mode.

interaction mode	events/10^{21}POT/ton with H_2O	events/10^{21}POT/ton with CH
All	2.07×10^5 (100 %)	2.10×10^5 (100 %)
CC	1.48×10^5 (71.6%)	1.56×10^5 (71.8%)
CCQE	6.98×10^4 (33.7%)	7.53×10^4 (34.5%)
CC1π	4.86×10^4 (23.4%)	4.97×10^4 (22.7%)
CCDIS,CCmultiπ	2.77×10^4 (13.3%)	2.89×10^4 (13.2%)
CCcoh	2.20×10^3 (1.0 %)	2.79×10^3 (1.2 %)
NC	6.90×10^4 (28.4%)	6.20×10^4 (28.2%)
NCela	3.04×10^4 (14.6%)	3.18×10^4 (14.5%)
NC1π	1.87×10^4 (9.0 %)	1.91×10^4 (8.7 %)
NCDIS,NCmultiπ	8.04×10^3 (3.8 %)	8.49×10^3 (3.8 %)
NCcoh	1.41×10^3 (0.6 %)	1.86×10^3 (0.8 %)

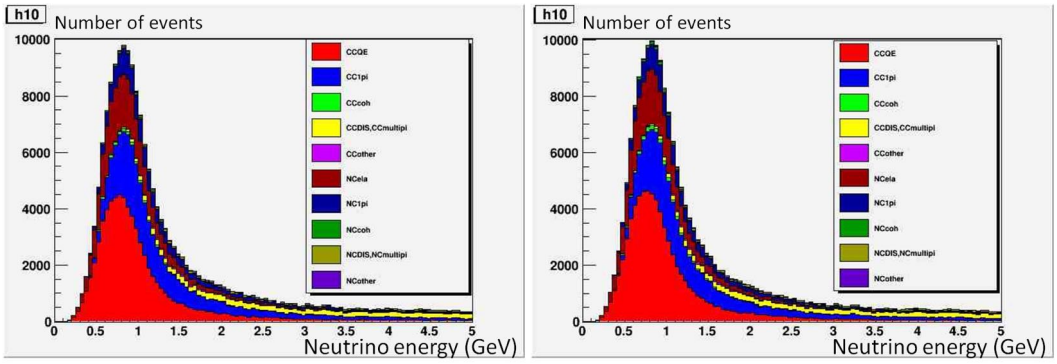

Figure 3.6: Energy of neutrinos interact with H_2O (left) and CH (right) target

The large scattering angle muons have relatively low energy, around a few hundreds MeV.

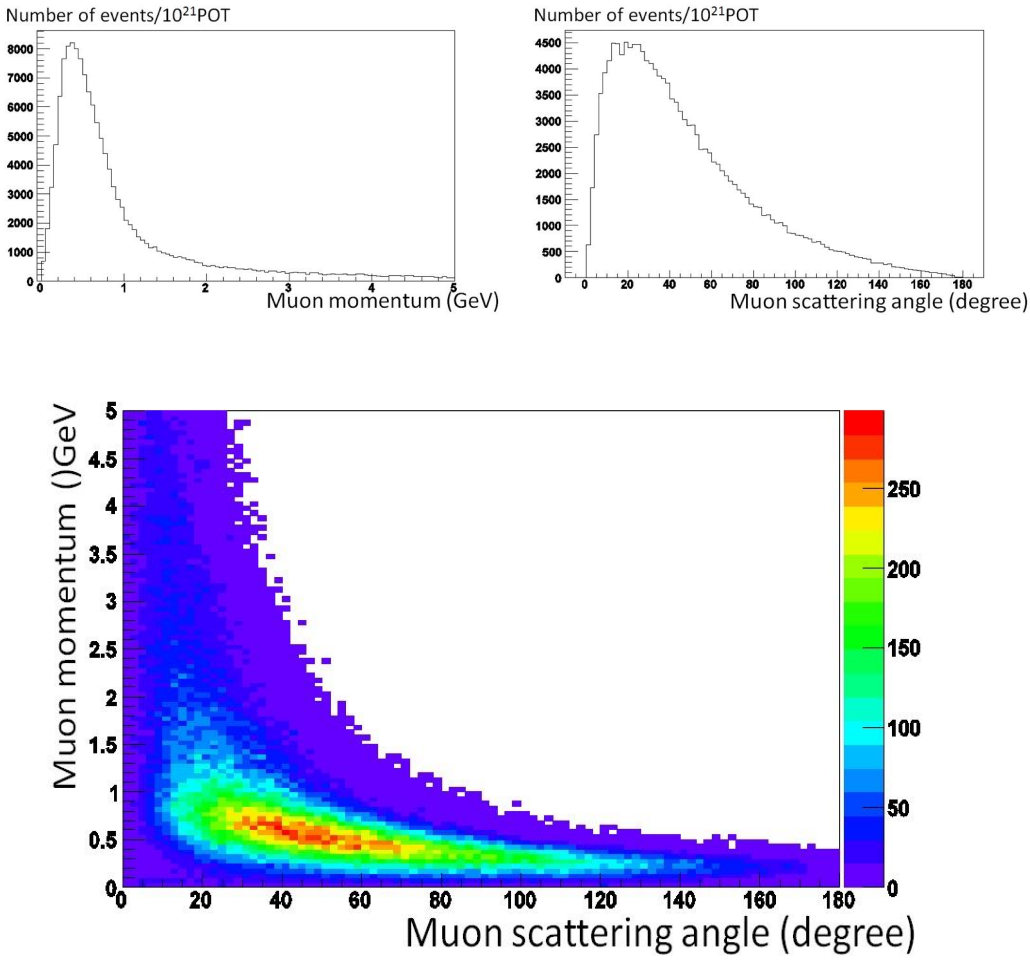

Figure 3.7: Momentum (upper left) and scattering angle (upper right) and both of them (lower middle) of the muons produced by charged current interaction

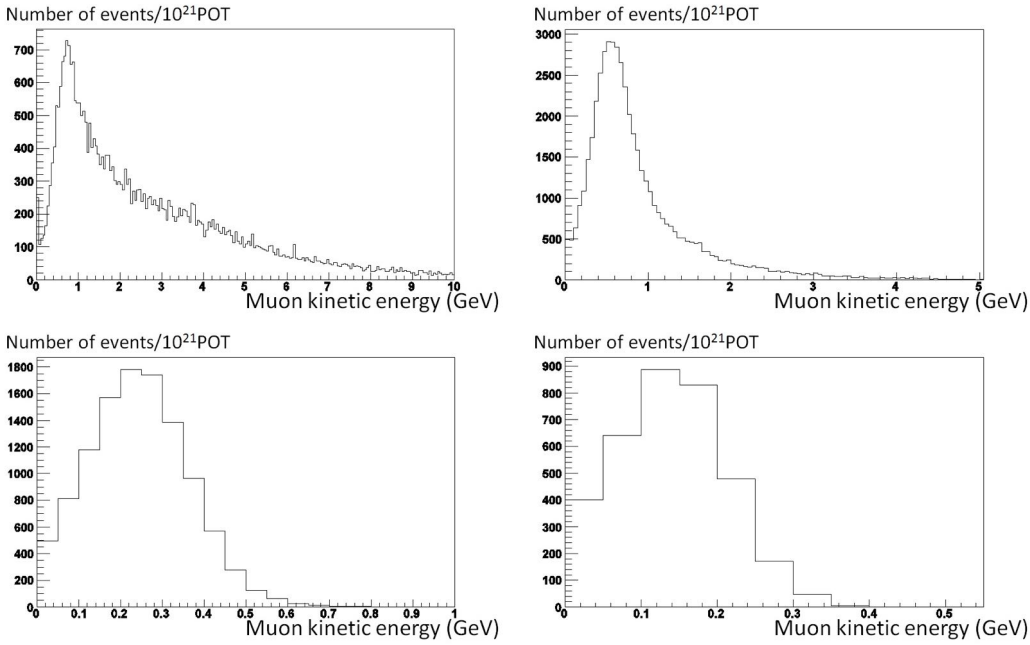

Figure 3.8: Kinetic energy of muons. Their scattering angle is 0–20 degrees (upper left), 20–45 degrees (upper right), 45–135 degrees (lower left) and 135–180 degrees (lower right).

3.5 Optimization of the detector

To optimize the size of the target and MRDs, we simulate the passage of the muons produced by neutrino interaction on water target by using Geant4 [26]. Geant4 is a toolkit for the simulation of the passage of particles through matter. Information such as vertex position, kind of particles, momentum and direction of the secondary particles is given by NEUT. Figure 3.9 shows the set up of the simulation. As a water target, $1.5 \times 1.5 \times 1.5\ m^3$ water is put. As side MRDs, $2.5 \times 2.5 \times 1.0\ m^3$ iron is put. As a downstream MRD, $2.5 \times 2.5 \times 2.5\ m^3$ iron is put.

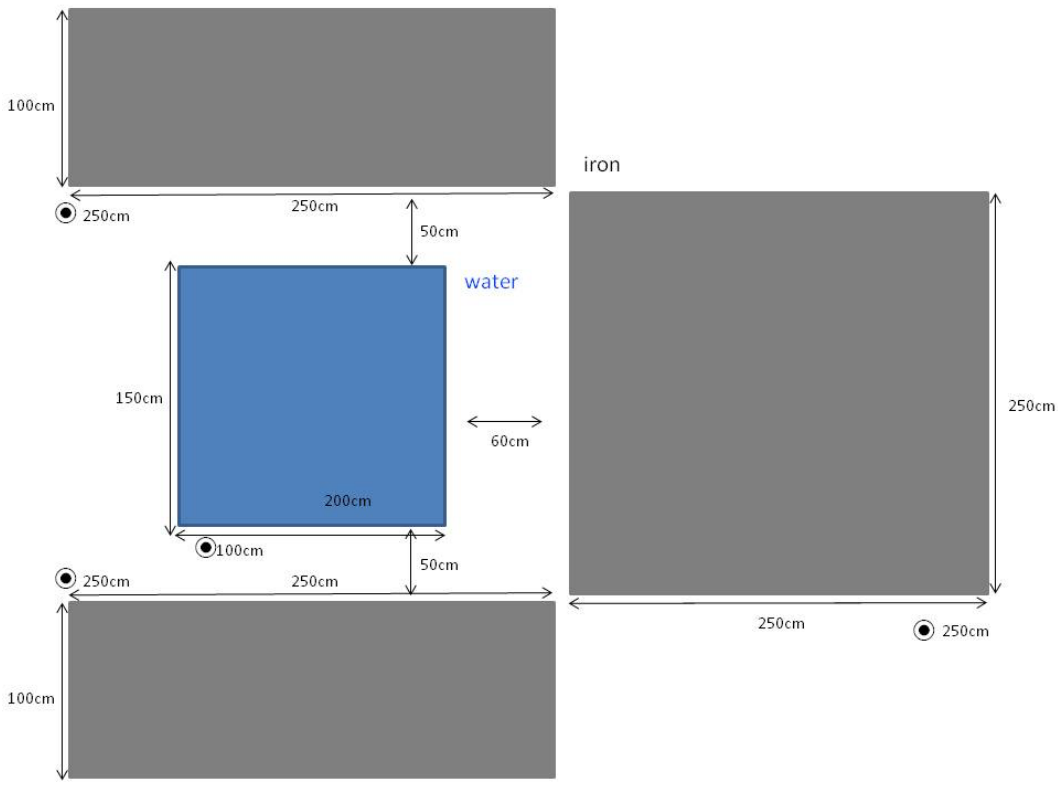

Figure 3.9: Set up of Monte Carlo simulation to optimize the target and the depth of the MRDs.

3.5.1 Size of target

The mass of the target is determined by statistics. The expected number of POT is $3.0\times\ 10^{20}$ per year and $1.48 \times 10^5 \times 0.3$ =$4.4\times\ 10^4$ muons are

produced per year per ton, as shown in Table 3.3. In order to accumulate 3×10^4 interactions in a year, the mass of the target should be more than 0.7 ton. Taking the fiducial volume into consideration, each mass of the H_2O and CH target is determined to be 1 ton.

As shown in Fig. 3.7, the number of the large scattering angle muons are relatively small. It should be maximized by the optimization. Figure 3.10 shows the initial point of muons stopped in the left side MRD. The number of muons becomes smaller as the initial point becomes farther from the left side MRD due to their acceptance and muons stopping inside the target volume. The initial x position for 90% of muons are within 1.0 m from the left side edge of the target. This plot and the available space at the candidate site considered, the width of the target along with x axis is determined to be 1.0 m. The height of the target along with y axis is also determined to be 1.0 m because of the space constraint and easiness of the detector construction. To keep the total mass of the each target 1ton, the depth of the target along with z axis is determined to be 2.0 m.

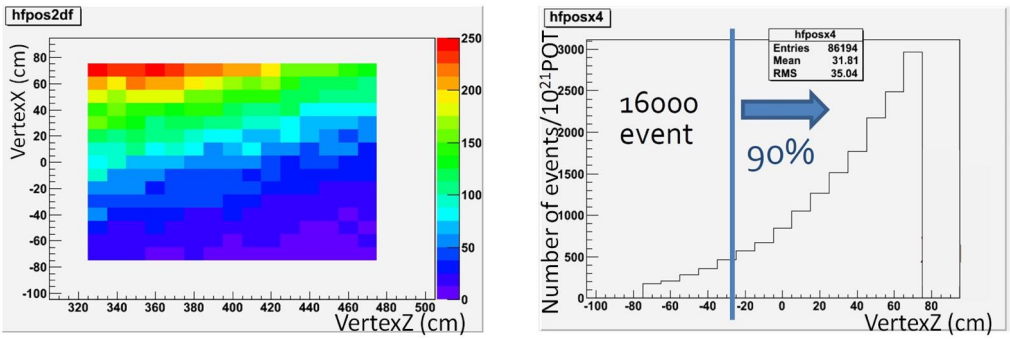

Figure 3.10: Vertex of the muons stopped in the left side MRD along with z-x axis (left) and x axis (right)

3.5.2 Optimization of arrangement of H_2O and CH target

To optimize the arrangement of H_2O and CH target regions, the passage of muons is simulated again with a resized $100 \times 100 \times 200$ cm^3 target. To reduce the difference of the neutrino flux between H_2O and CH target regions, each target should be arranged alternately along with z-axis. First, $100 \times 100 \times 100$ cm^3 water and $100 \times 100 \times 100$ cm^3 hydrocarbon are put alternately along with z axis. Figure 3.11 shows the angle of muons which is produced in a fiducial volume, the region excluding 5 cm from the edge

of the each target, and stop inside the MRDs. The efficiency of muons is different between targets due to the difference of the distance from the downstream MRD. To reduce this difference, $100 \times 100 \times 50\ cm^3$ water and $100 \times 100 \times 50\ cm^3$ hydrocarbon are put alternately along with z axis. In this case, as shown in Fig. 3.12, the difference is reduced and the number of muons are almost the same as the 100 cm depth case.

The neutrino flux on H_2O target and CH target with this configuration are shown in Fig. 3.13. The difference is less than 3 % for the neutrino energy of 0–1GeV. Finally, the targets are arranged as shown in Fig. 3.14.

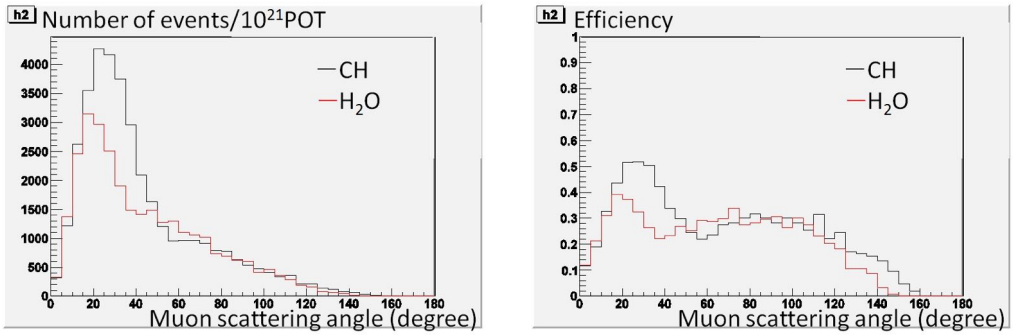

Figure 3.11: Scattering angle (left) and efficiency (right) of the muons stopped in MRDs. Black (Red) line is the muons produced on $CH(H_2O)$ target region. The depth of the each target is 100 cm.

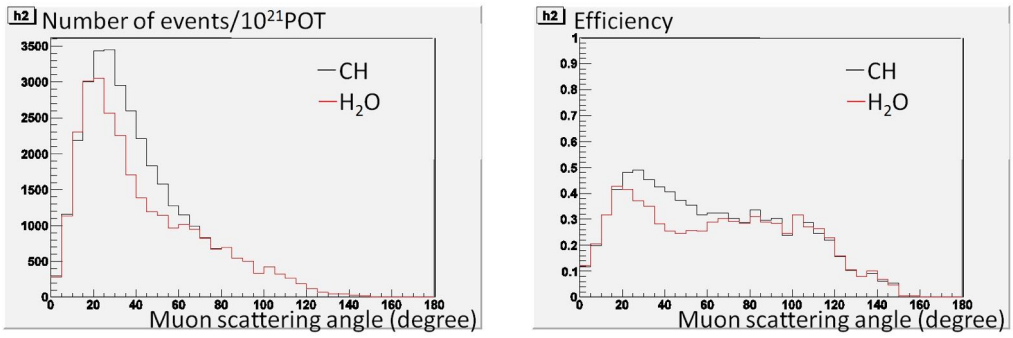

Figure 3.12: Scattering angle (left) and efficiency (right) of the muons stopped in MRDs. Black (Red) line is the muons produced on $CH(H_2O)$ target regions. The depth of the each target is 50 cm.

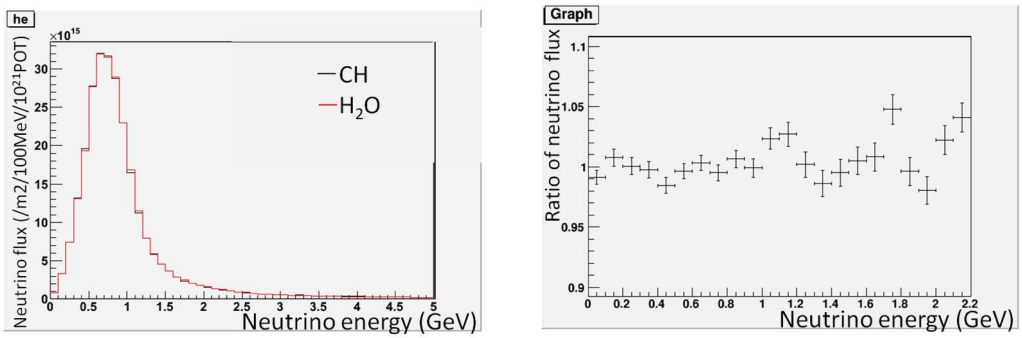

Figure 3.13: Neutrino flux at CH (black line) and H_2O (red line) target regions (left) and their ratio (right). Error bars of the ratio are due to the MC statistics.

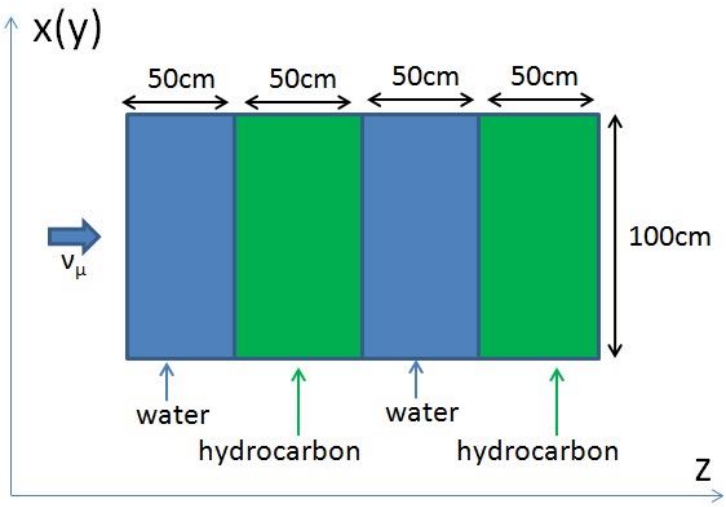

Figure 3.14: The final arrangement of the target. The size of the each target is $100 \times 100 \times 50\ cm^3$.

3.5.3 Size of the MRDs

Iron is used for the MRDs because it is cheap and heavy. Figure 3.15 shows the stopping point of muons in the simulation with the configuration shown in Fig. 3.9. In the downstream MRD, it is difficult to stop all muons. Figure 3.16 shows the relation between muon momentum and its path length in iron. We decide the depth of the iron in the downstream MRD to be 90 cm in order to stop muons with energy less than 1 GeV. The total thickness of the iron for the side MRDs is determined to be 30 cm to stop more than 90% of muons.

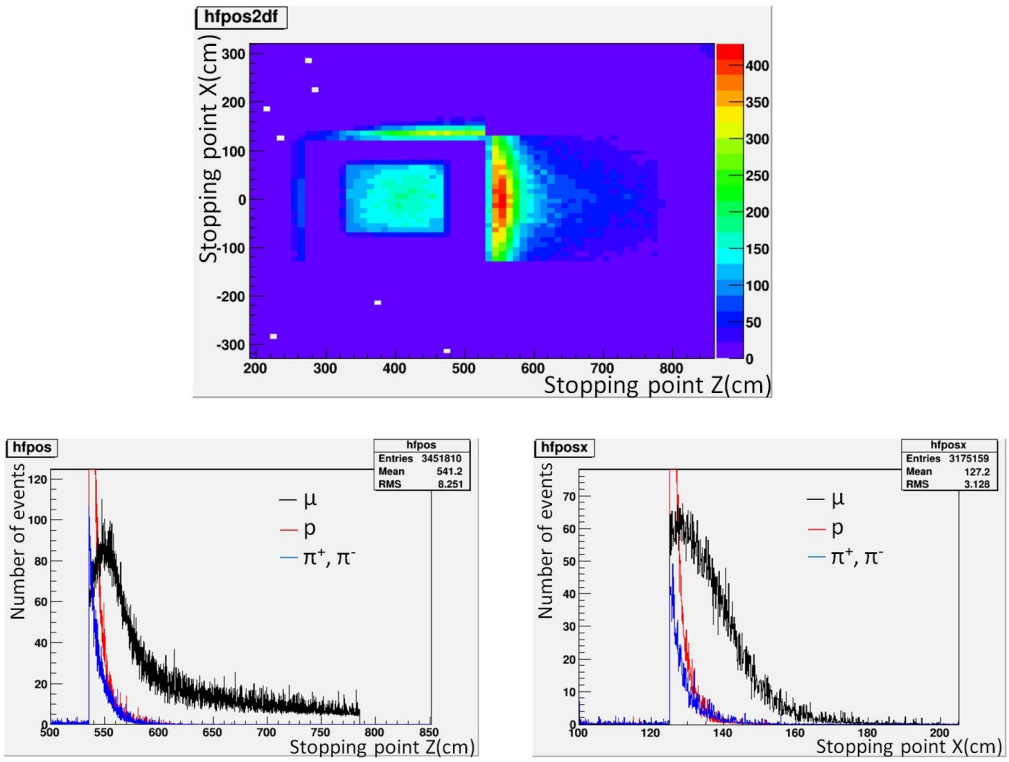

Figure 3.15: Stopping point of muons along with z-x axis (upper), z axis in the downstream MRD (lower left) and x axis in the left side MRD (lower right).

The MRDs are composed of a sandwich structure of iron plates and plastic scintillators. The thickness of an iron plate is determined by the required momentum resolution. As shown in Fig. 3.8, the mean kinetic energy of muons which have large scattering angle is around 250 MeV. In order to measure the kinetic energy of muons with the accuracy of $\pm$ 10%, the required resolution of the side MRD is $\pm$ 25 MeV i.e. 50 MeV interval. Then, thickness is determined to be 3 cm because the energy deposit of muons passing through

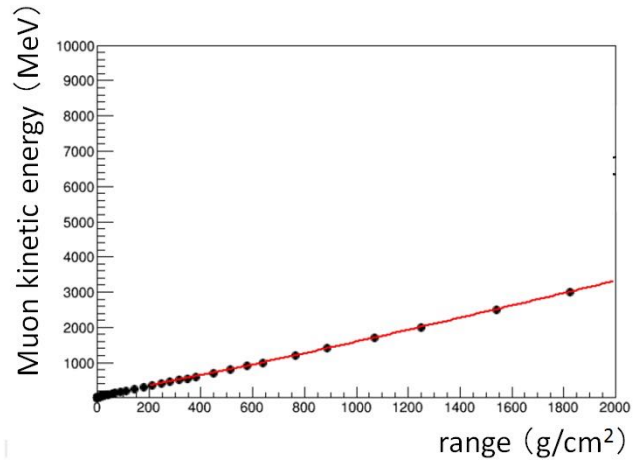

Figure 3.16: Muon kinetic energy vs path length in iron [3].

1 cm of iron with 45 degrees is 16.5 MeV. In the downstream MRD, the thickness of the first ten iron plates is 3 cm to be the same as the side MRD, while that of the last ten iron plates is 6 cm to reduce the number of the channels.

To determine the height and width of the MRDs, the passage of muons is simulated again with the resized target and irons as shown in Fig. 3.17. As a target, $100 \times 100 \times 200\ cm^3$ water is assumed. As side MRDs, $300 \times Y \times 3\ cm^3$ 10 iron plates are assumed where Y is changed to 150 cm, 200 cm and 250 cm. As a downstream MRD, $X \times Y \times 3\ cm^3$ 10 iron plates and $X \times Y \times 6\ cm^3$ 10 iron plates are assumed where X is changed to 200 cm, 300 cm and 400 cm.

The width of the side MRDs is determined to be 300 cm to detect the muons around 45–135 degrees. The height of the side MRDs is determined by statistics. We check the number of muons stopped in the side MRDs with varying the height of the side MRDs. Figure 3.18 shows the number of muons stop in the side MRDs, produced on the fiducial volume of the water targets. In order to obtain the enough statistics (1×10^3 muons per ten degree), the height should be around 200 cm. Due to a limit of the weight of the MRD for the installation, it is determined to be 180 cm. To simplify the design, the height of the downstream MRD is also determined to be 180 cm.

To determine the width of the downstream MRD, we check the number of muons stopping inside the MRDs with varying its width, as shown in Fig. 3.19. There is no big difference between the cases with the width of 400 cm and 300 cm. In the case of the 200 cm width, the efficiency decreases by about 10 % around 40 degrees. The width of the downstream MRD

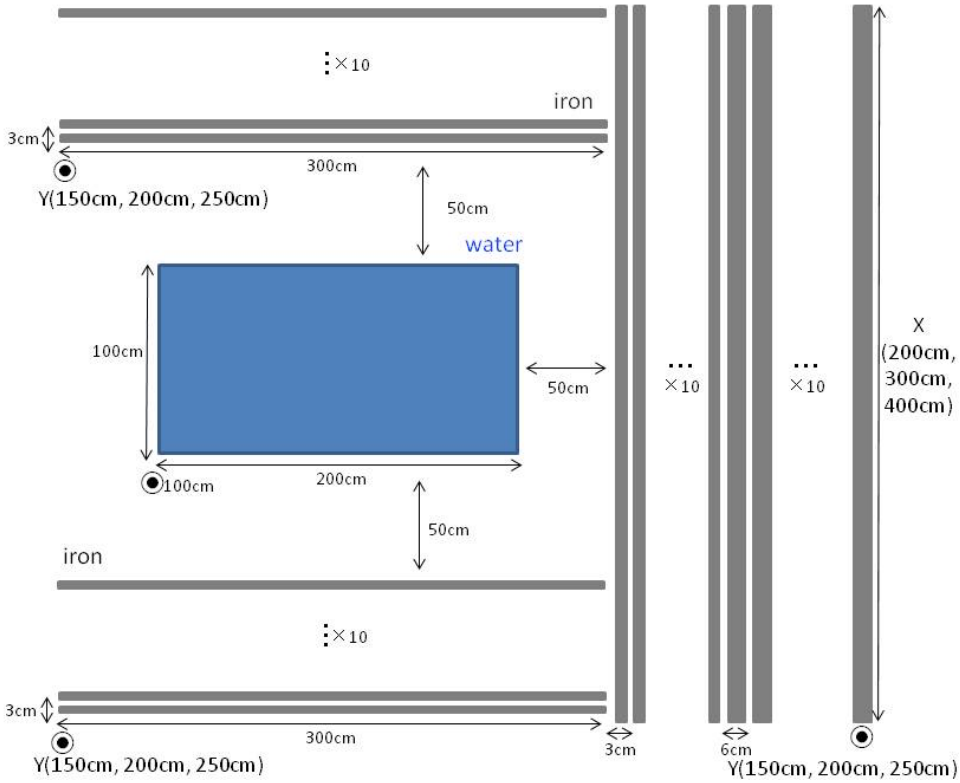

Figure 3.17: Set up of Monte Carlo simulation to optimize the width and height of the MRDs.

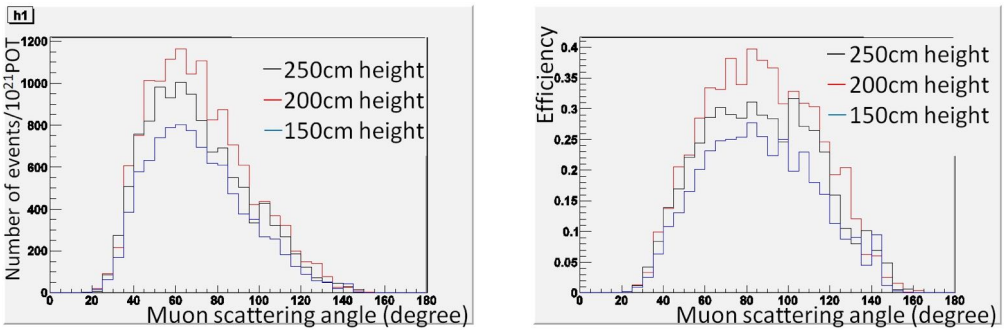

Figure 3.18: Muons stop in the side MRDs, produced on fiducial volume of the H_2O target (left) and their efficiency (right)

should be around 300 cm. Finally, the width of the downstream MRD and side MRD is determined to be 320 cm to simplify the design and due to the limit of the weight of the MRD. Figure 3.20 shows the optimized target and MRDs.

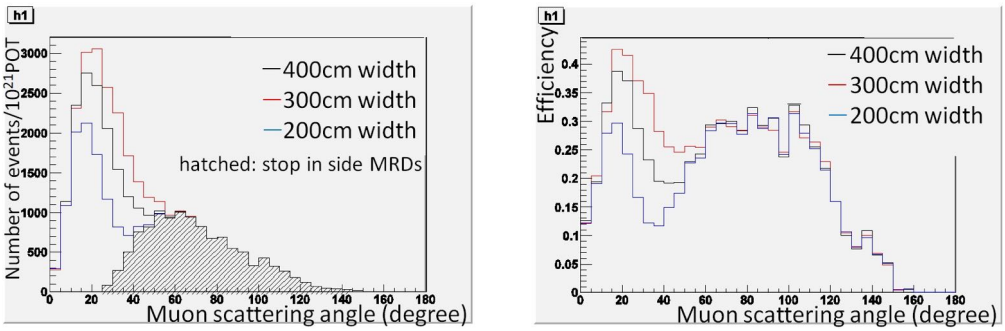

Figure 3.19: Muons stop in the downstream MRD and the side MRDs (hatched), produced on H_2O target (left) and their efficiency (right).

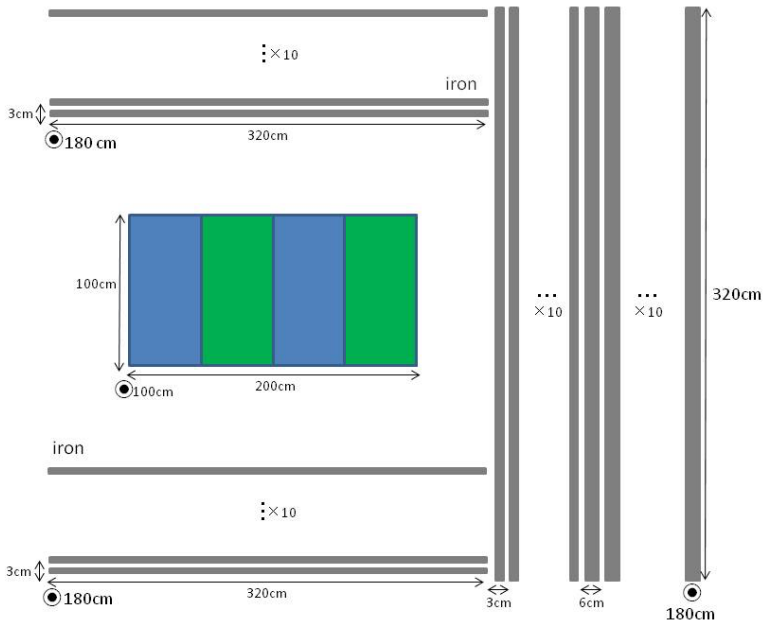

Figure 3.20: The final arrangement of the MRDs.

3.6 Optimization of scintillators

3.6.1 Scintillators inside the central detector

Inside the central detector, plastic scintillator bars are aligned in a 3D grid like structure as shown in Fig. 3.2. Spaces between scintillators are filled with the neutrino target materials, water or hydrocarbon cubes. This structure enables us to reconstruct high angle track and obtain large acceptance. The size of the scintillator is $100 \times 2.5 \times 0.3 \times cm^3$. The thickness is determined to be as thin as possible while keeping the light yield. The length of the scintillator is 100 cm, same as the width of the targets. The scintillators are arranged as shown in Fig. 3.21 to satisfy the requirement of the number of the channels. A MPPC is connected to only one side of the scintillators and the number of channels is 6400. The fraction of water mass is 79% for this configuration.

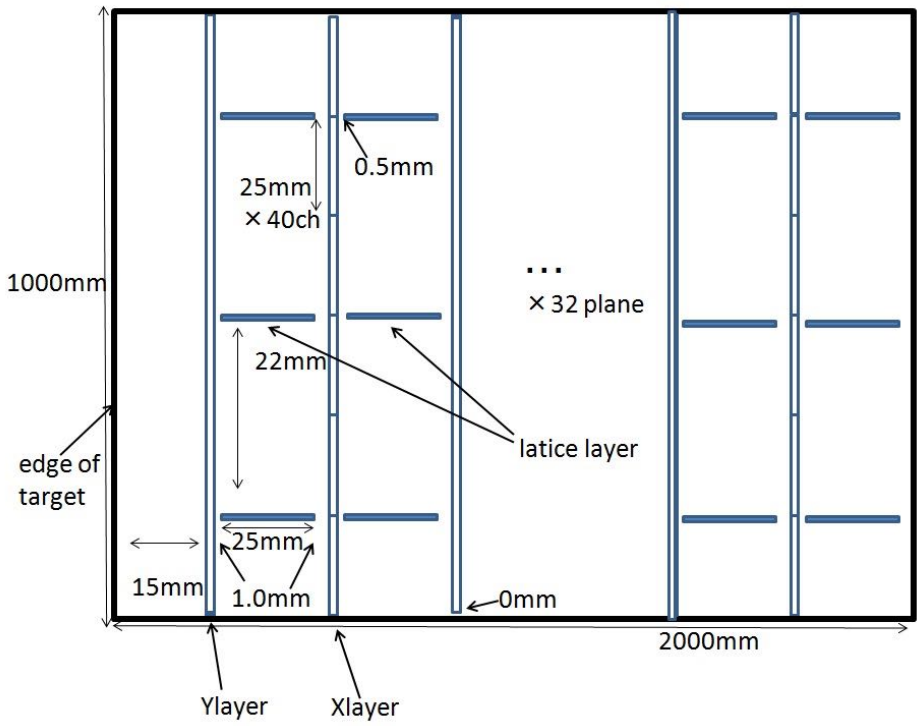

Figure 3.21: Side view of the arranged scintillators inside the central detector.

3.6.2 Scintillators in the MRDs

The size of the scintillators used in the MRDs is 180×20×0.7 cm^3. Almost same dimension scintillators are used for MRD in T2K experiment. They are arranged between iron plates parallel to the y-axis. Two MPPCs are connected to both edge of a scintillator and the number of channels is 1280. The hit position along with y axis is measured by timing difference between two MPPCs. Its accuracy is 10 cm and this is better than that measured by light yield difference between two MPPCs.

3.6.3 Scintillators around the target

The main background is considered to be particles generated in neutrino interactions with MRDs and the wall of the detector hall. In order to reject such background coming from outside the central detector, we use the time of flight information. To measure the timing, 180×50×1 cm^3 scintillators are used because it has relatively good time resolution, 1 ns. Same type of the scintillators is also used in T2K. They are arranged around the target and in front of the MRDs as shown in Fig. 3.22. The hit timing is measured by inner TOF scintillators and outer TOF scintillators separately. Their difference is used for rejection of incoming particles. The number of planes of the scintillator is determined by required timing resolution in order to measure the direction of travel of particles with the accuracy of 2 σ. The distance between the MRD and the target is determined to be as near as possible while keeping the number of readout channel. Table 3.4 shows the relation between the number of plane and the distance between the MRD and the target and the distance is determined to be 50 cm. A MPPC is connected to only one side of the scintillators and the number of channels is 1264.

Table 3.4: The relation between the number of scintillator planes and distance between the targets and the MRDs.

distance	number of planes	number of events
30 cm	8	20% higher than 50 cm
50 cm	3	
70 cm	2	10% lower than 50 cm

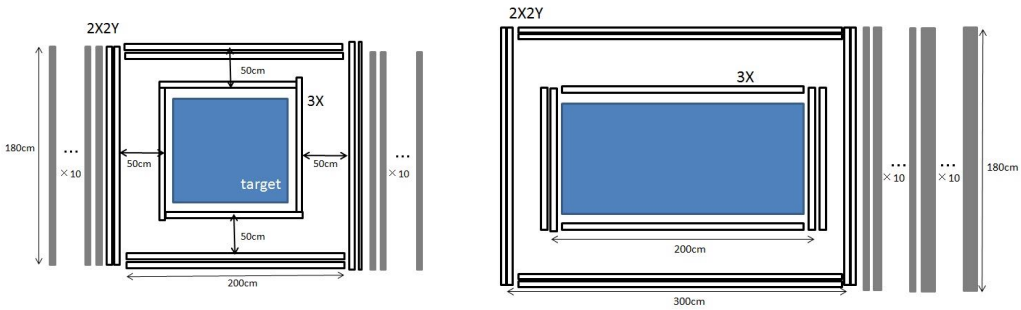

Figure 3.22: The front (left) view and side (right) view of the TOF planes (white square).

3.6.4 Summary of the design of the detector

Table 3.5 shows the summary of the design of the detector and Fig. 3.23 shows the final design of the new detector.

Table 3.5: Summary of the detector parameters

Central detector		Size	100×100×200 cm^3
		Size of the each target part	100×100×50 cm^3
		Target masses (H_2O, CH)	1 ton each
		Size of scintillators in the target region	100×2.5×0.3 cm^3
		Size of scintillators for TOF	120(180)×5×1 cm^3
		Number of channels	6400(target)+1264(TOF)
MRD	Side	Size	50×180×320 cm^3
		Thickness of iron plates	3 cm (10 planes)
	Downstream	Size	320×180×150 cm^3
		Thickness of iron plates	3 cm (10 planes) 6 cm (10 planes)
	Total	Size of scintillators	180×20×0.7 cm^3
		Number of channels	1280

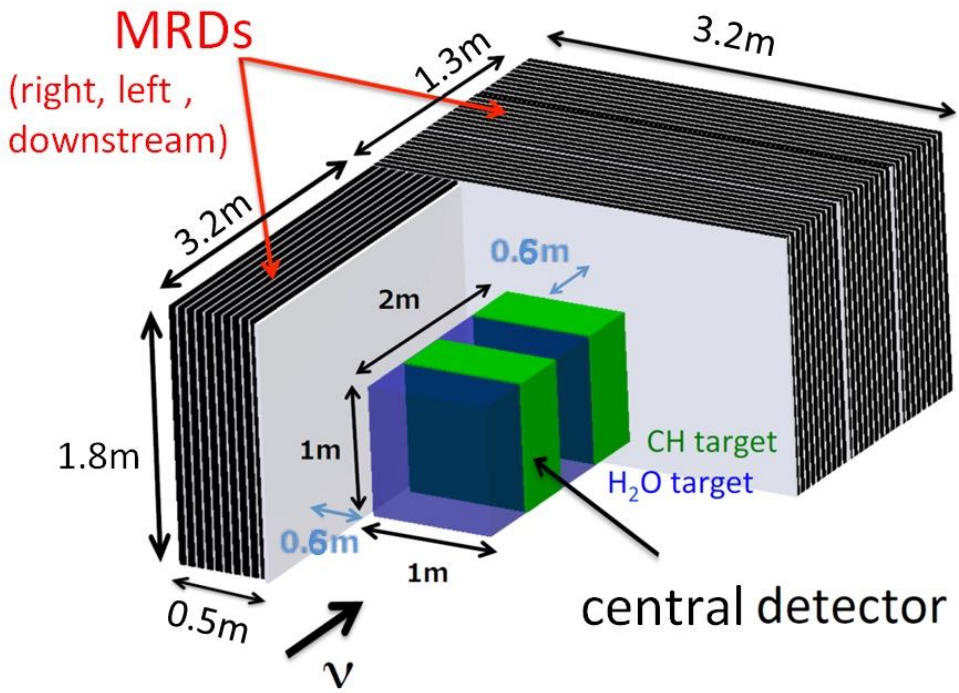

Figure 3.23: Schematic view of the detector after the optimization. Scintillators and the right side MRD are not drawn.

Chapter 4

Performance test of the detector components

4.1 Detector components of the WAGASCI

In the target region, thin, 3 mm thickness scintillators are used to reduce the fraction of non-water material. It is produced in Fermilab. Figure 4.1 shows the picture of the scintillator. There is a straight groove to put the wavelength shifting fiber. Reflector, TiO_2, is co-extruded to increase the light yield and separate the scintillators optically. The scintillators are aligned in a 3D grid like structure as shown in Fig. 3.2. To make this structure, some machining are applied.

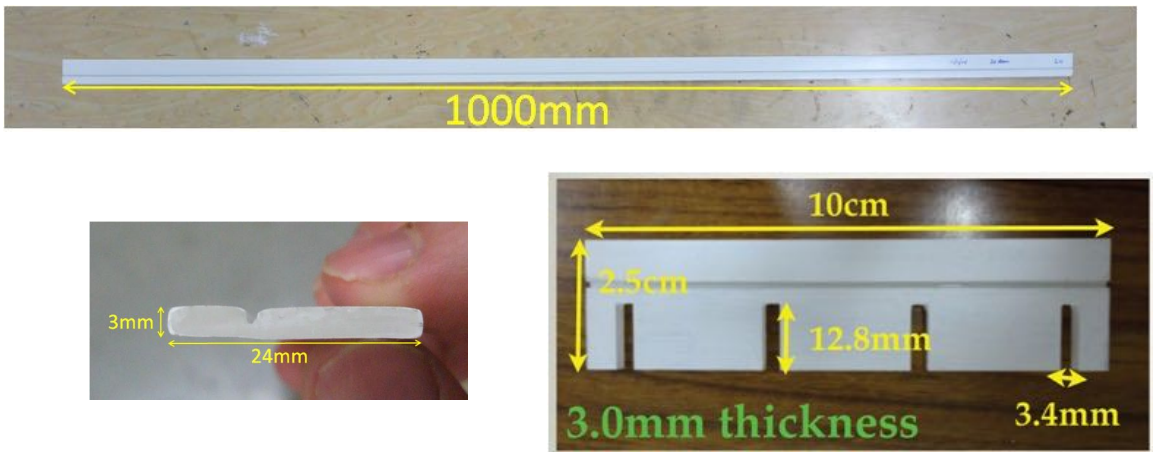

Figure 4.1: Schematic view of the 3 mm thickness scintillator. The size is $100 \times 2.5 \times 0.3\ cm^3$. The sample used in the beam test is machined (lower right).

The scintillation light from the scintillators is collected by a wavelength shifting fiber and read by a semiconductor photo detector, Multi-pixel Photon Counter (MPPC) [27]. The wavelength shifting fiber, Y-11(200) [28], is produced by Kuraray company. The scintillation blue light is absorbed and green light is emitted, as shown in Fig. 4.2. It makes the attenuation length longer. The scintillator, fiber and MPPC are connected as follows:

1. The fiber is put on the straight groove of the scintillator and it is glued by optical cement[1]. Before put the fiber, air bubbles in the cement are excluded by hand. It is set one day for drying.

2. Additional reflector[2] is painted on the fiber. It is painted divided two times and set one day for drying.

3. The fiber is connected to MPPC by a fiber bundle. It is also glued by the optical cement. A edge of the fiber is polished by fiber polisher.

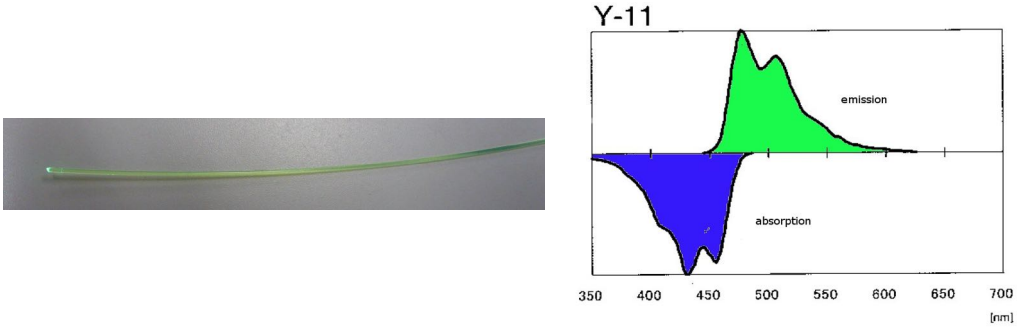

Figure 4.2: Wave length shifting fiber (left). Absorption and emission wavelength of the fiber (right). [28]

The MPPC is a new type of photon-counting device made up of multiple APD pixels operated in the Geiger mode, as shown in Fig. 4.3. When a photon hits an APD pixel, it creates an electron-hole pair and causes avalanche multiplication. In the Geiger mode, the electric field in the APD is strong, therefore the avalanche multiplication can not stop by itself. MPPC controls this multiplication by using quenching register and keeping the output charge from a pixel constant. The total output charge of MPPC is proportional to the number of pixels which photons hit.

WAGASCI experiment requires a new photo device which have high photo detection efficiency and low noise because of the low light yield of the thin

[1]ELJEN TECHNOLOGY,EJ-500
[2]ELJEN TECHNOLOGY,EJ-510

plastic scintillators used in the central detector. It also should be compact and cheap because of the large number of the readout channels, around 10000. Good time resolution, better than ns, is also required for TOF. To satisfy these requirement, we plan to use a new low noise MPPC developed by Hamamatsu photonics.

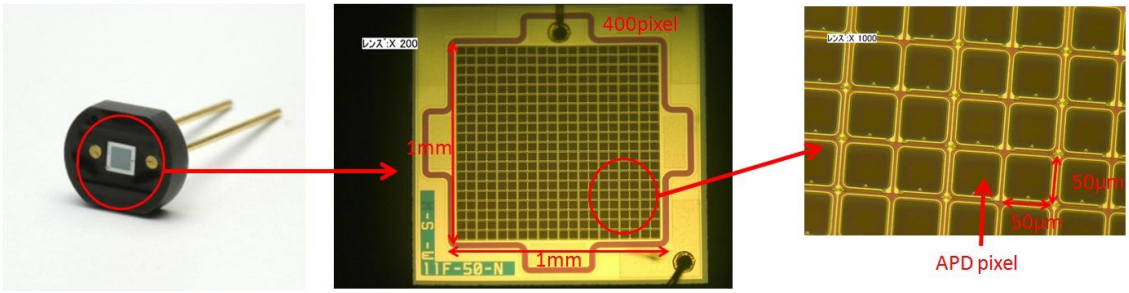

Figure 4.3: Pictures of the MPPC.

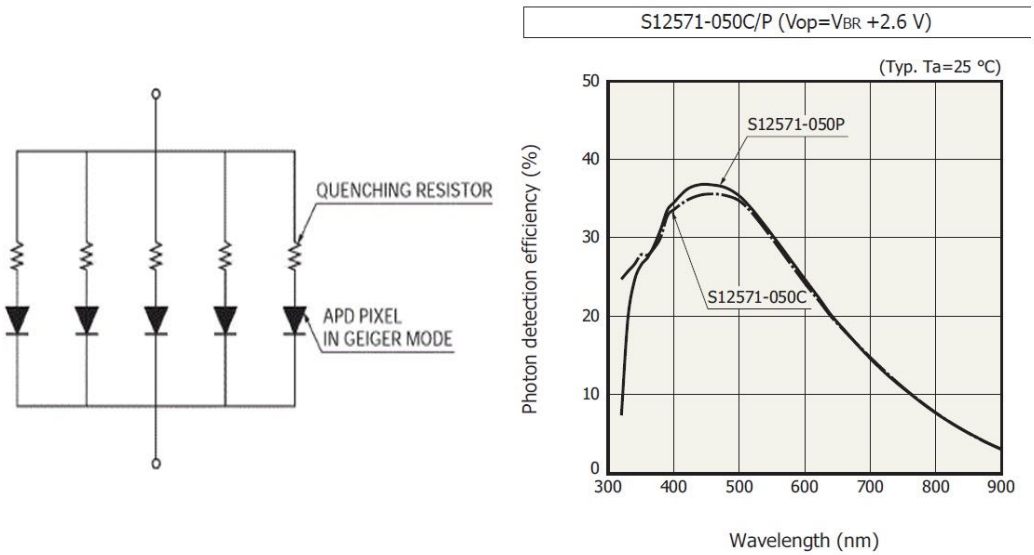

Figure 4.4: Equivalent circuit of the MPPC (left) and photo detection efficiency of MPPC [27].

In this chapter, some performance tests of the MPPC and scintillator are explained.

4.2 Performance test of MPPC

Older MPPC has some limitation, high dark noise rate and false pulses, crosstalk and after pulse. The crosstalk occurs when photons, produced by avalanche multiplication, hit other pixels. The afterpulse is a spurious pulse following the true signal. Both crosstalk and afterpulse make the output signal higher than the true value.

To improve this weak point, a new low noise MPPC is developed. It has low dark noise rate, crosstalk and afterpulse rate due to the improvement of a wafer. Figure 4.5 shows the waveform of the new and old MPPC. Where ΔV is defined as bias voltage minus break down voltage. Clear reduction of afterpulse and crosstalk is found for the new MPPC.

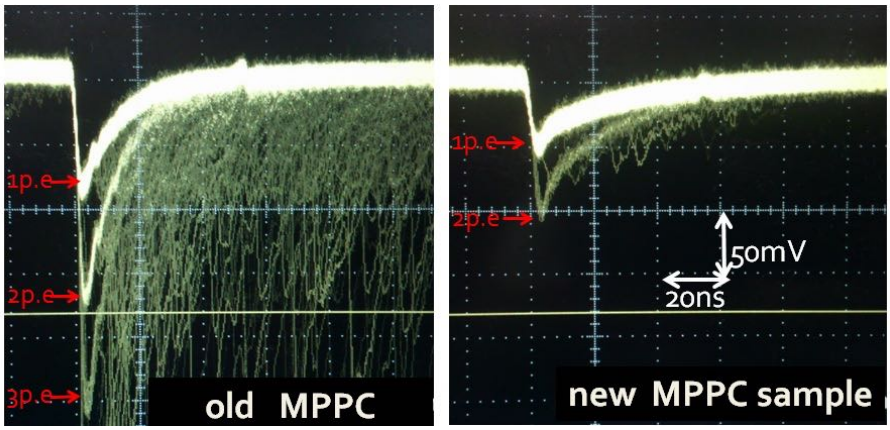

Figure 4.5: Waveform of each MPPC by oscilloscope. The signal is amplified by a factor of a hundred. ΔV=3.0V. Time constant of new MPPC is longer than that of old MPPC and the difference of operated gain of these two MPPCs is less than 10 %.

We test the performance of the sample of the new MPPC, produced in December 2014. Table 4.1 shows the list of the tested MPPC. Table 4.2 shows a summary of the measured parameters. Here ΔV of the old MPPC is set same as that of INGRID and ΔV of the new MPPC is set as high as possible to increase photo detection efficiency. The photo detection efficiency of the new MPPC is 1.78 times better than that of old MPPC while keeping the dark noise rate of new MPPC ten times lower than that of old MPPC. These performance is suitable for WAGASCI. Appendix B shows the measurement of the new MPPC samples produced in summer 2013.

We also plan to use 32 ch array type MPPC for the central detector and it is under development. Its performance is expected to be same as the tested

Table 4.1: List of tested samples

Kind of MPPC	Model number	Size of one pixel	Size of device
New MPPC	S13081-050CX	$50 \times 50 \mu m^2$	$1.3 \times 1.3\ mm^2$
Old MPPC	S10362-13-050C	$50 \times 50 \mu m^2$	$1.3 \times 1.3\ mm^2$

Table 4.2: Measured parameters for the new MPPC

Parameters	New MPPC (ΔV=4.0V)	Old MPPC (ΔV=1.1V)
Gain	2.6×10^6	7.0×10^5
Dark noise rate (Hz)	36k	520k
Crosstalk and afterpulse rate	0.052	0.11
Relative photo detection efficiency	1.78	1.0

sample in this measurement.

4.3 Performance test of the scintillator

The light yield of the 3 mm thickness scintillator is expected to be low because it is thin and some machining are applied. We test the light yield of the sample of the 3 mm thickness scintillator twice by using positron beam. The beam test is done in May 2014 and December 2014 at Tohoku University. In this section, the result of the second beam test is mainly described.

4.3.1 Setup

Figure 4.6 shows the beamline of the Tohoku University [29]. An electron is accelerated in LINAC and STB ring and emits synchrotron light. The light injects to an Au target and positrons and electrons are produced. The positron is focused by a magnetic field and their energy and width can be selected by changing the strength of the magnetic field. The beam parameters are set as shown in Table 4.3.

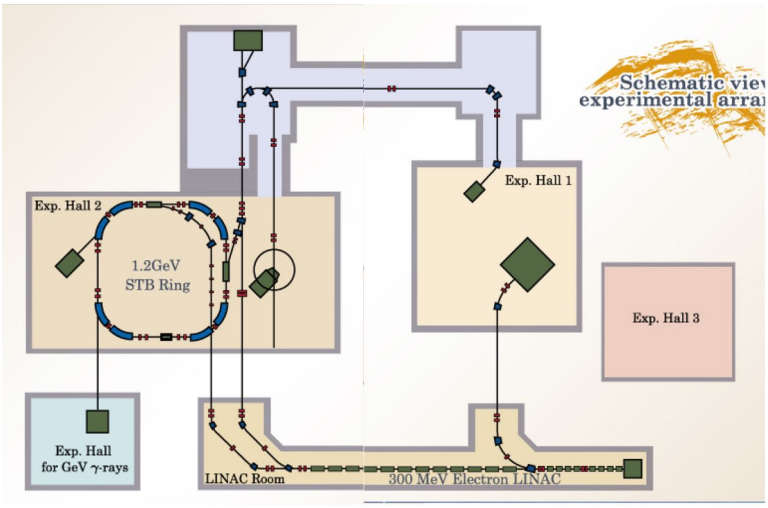

Figure 4.6: Schematic view of the positron beamline. The measurement is done in Exp.Hall for GeV γ-rays. [29]

Figure 4.7 shows the setup of the measurement. The positron beam is injected to the tested scintillator straightly. The scintillator is put between a hodoscope and a trigger scintillator for tagging the positron. The hodoscope consists of two scintillation fiber layers and each layer is composed of sixteen 1.5 mm width scintillation fiber. It measures the position of the injected positron. Figure 4.8 shows the positron beam profile measured with the hodoscope. Figure 4.9 shows the readout circuit of the measurement. The

Table 4.3: The parameters for the positron beam.

energy	589MeV
rate	2 kHz
σ_X	~1.5 cm
σ_Y	~1.0 cm

ADC and TDC value of the tested scintillator are recorded when the signals of the trigger scintillator and both horizontal and vertical layer of the hodoscope exceed the threshold level. The new MPPC with $\Delta V = 4.0V$ is used in this measurement.

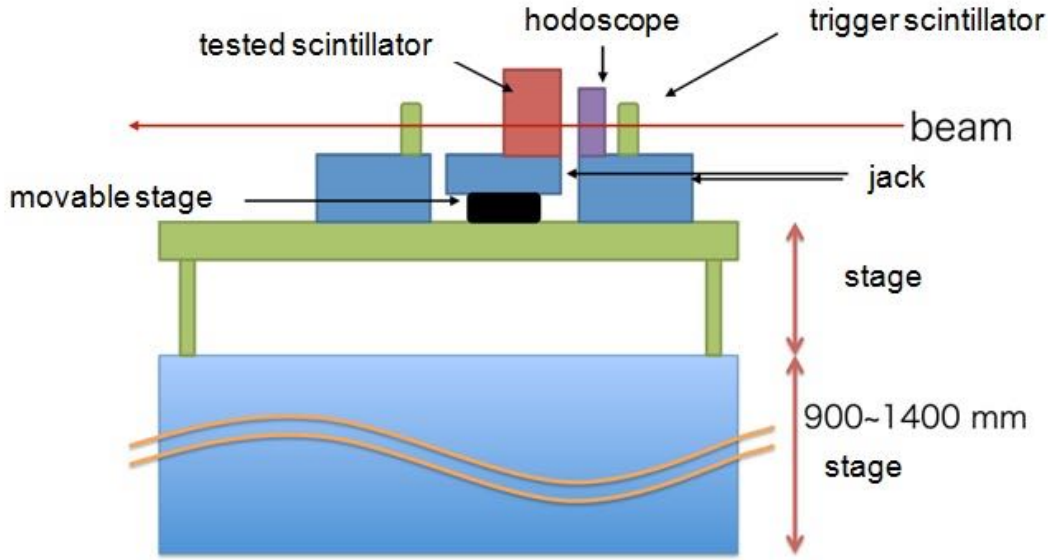

Figure 4.7: Schematic view of the setup

4.3.2 Result of measurements of the 3.0 mm thickness scintillator

Two types of 3.0 mm thickness scintillators, without machining and with machining to construct the 3D grid, are tested. The beam is injected to the scintillator without machining as shown in Fig. 4.10. The length of the fiber is 60 cm. The number of events is about one thousand in each 1.5×1.5 mm^2

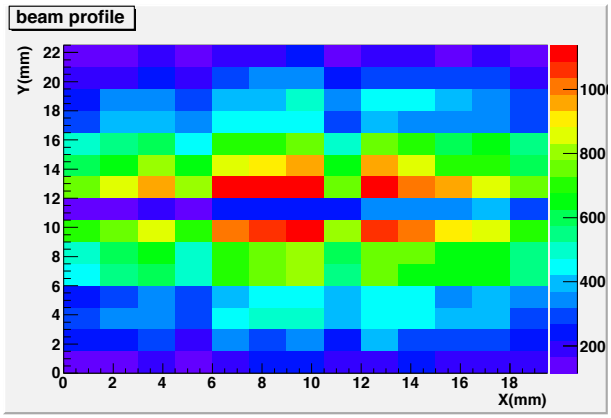

Figure 4.8: Beam profile by the hodoscope

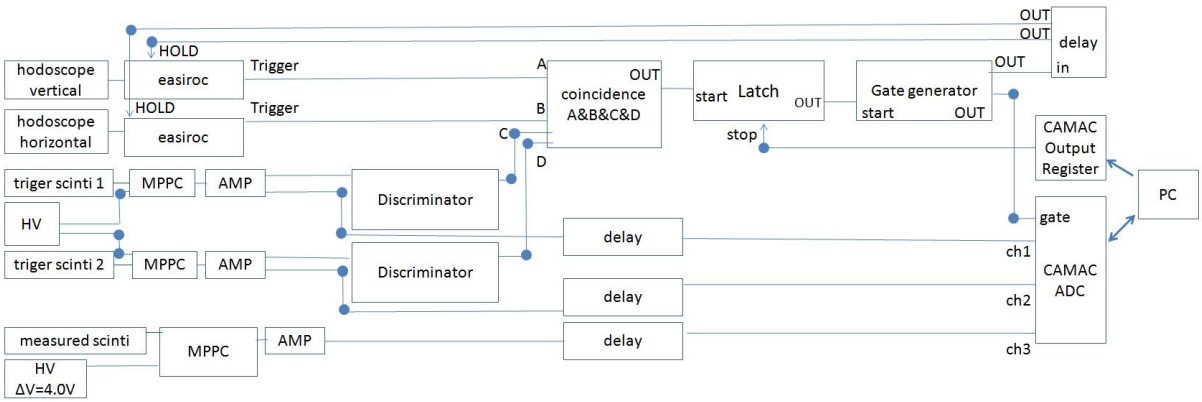

Figure 4.9: Schematic view of the circuit

bin and the statistical error is lower than 1 % in each 1.5 mm bin along with Y axis. Figure 4.11 shows typical ADC distribution. Figure 4.12 shows the mean light yield in each position. The effect of the crosstalk and after pulse is subtracted by dividing the mean light yield by 1 plus crosstalk and afterpulse rate, 1.052. In the left plot of Fig. 4.12, the position of the fiber is at Y=10 mm. Near the fiber, the mean light yield is more than 20 p.e. On the fiber, it is relatively low due to the groove. The light yield seems not to depend on the beam position along with X axis. Fig. 4.13 shows the mean light yield along with Y axis. The light yield is decreasing going away from the fiber. It is fitted by an exponential function as a distance from the fiber and the attenuation length is 30 mm.

Figure 4.14 shows the detection efficiency in each position. The threshold

is set to 1.5 p.e. The efficiency is more than 99 % in any position. The region within 1.5 mm from the edge of the scintillator can not be evaluated because of the resolution of the hodoscope.

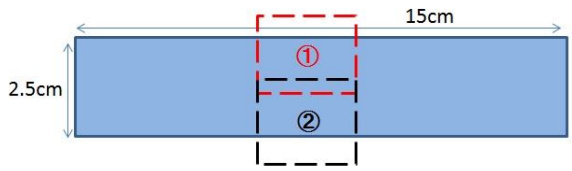

Figure 4.10: Position of the beam injected to the scintillator

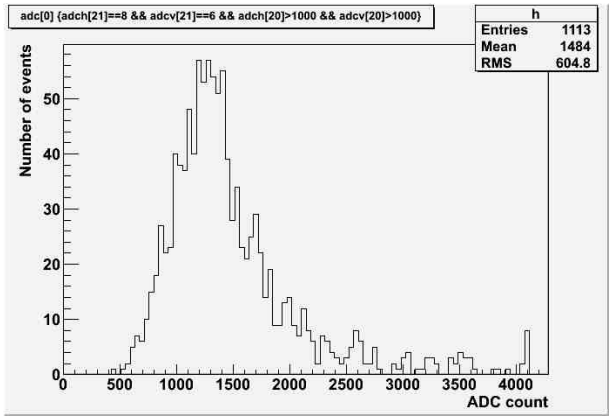

Figure 4.11: ADC distribution at X=10 mm, Y=6 mm in Fig. 4.12 left plot. Pedestal (1p.e.) coresponds to 102.9 (171.6) adc counts.

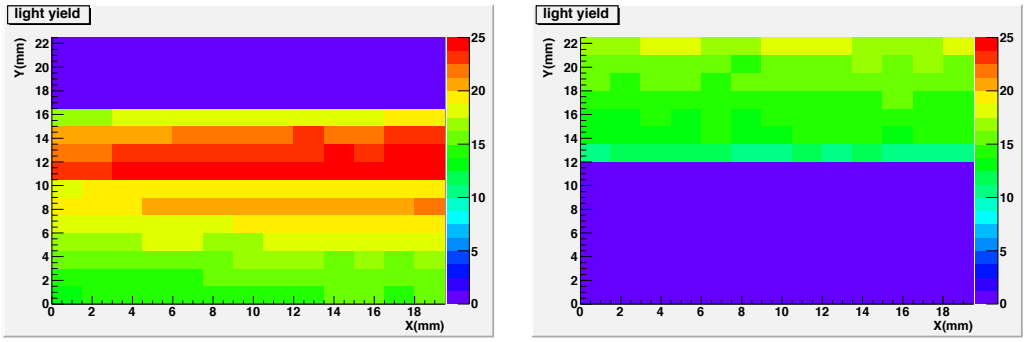

Figure 4.12: Mean light yield in each position. Left (right) plot corresponds to ① (②) in Fig. 4.10.

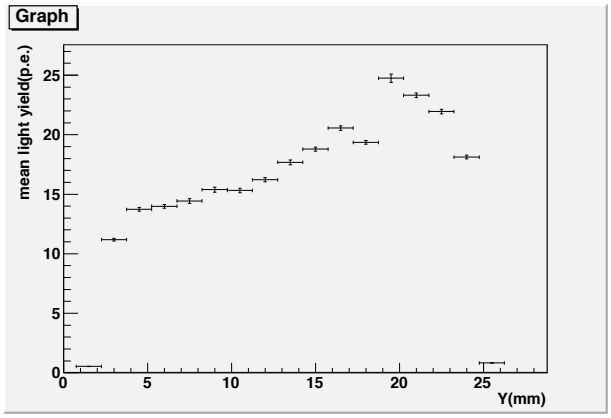

Figure 4.13: Mean light yield along with Y axis. The fiber is in Y=18 mm. The error bars are only statistical error.

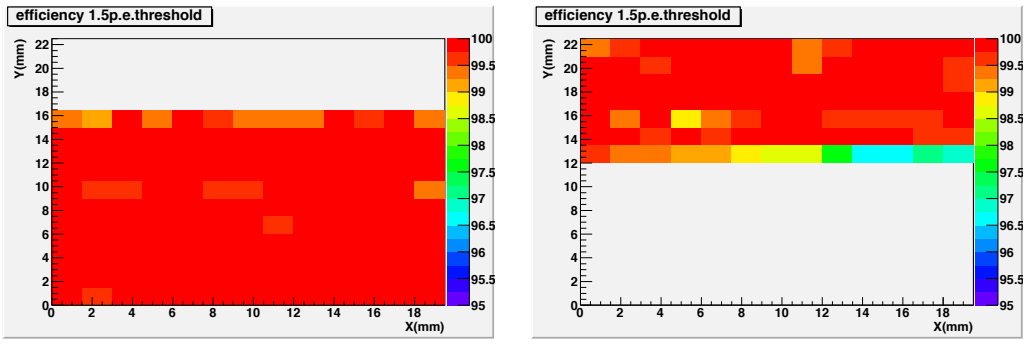

Figure 4.14: Detection efficiency in each position. Threshold is 1.5 p.e. Left (right) plot corresponds to ① (②) in Fig. 4.10.

The beam is injected to the scintillator with machining as shown in Fig. 4.15. The length of the fiber is 60 cm. For the data taking, the number of events at the edge of the scintillator, X=6 mm in Fig. 4.16, is required to be more than ten thousand to measure the efficiency with the 1 % statistical accuracy. Figure 4.16 shows the mean light yield in each position. The position of the fiber is at 8 mm(left plot) and 20 mm(right plot). The tendency of the light yield is same as that of the scintillator without machining, however, the light yield is a little low overall. The reason of it is under investigation and maybe due to the effect of the machining or individual difference of the scintillator. Figure 4.17 shows the mean light yield along with Y axis. The attenuation length is 25 mm.

Figure 4.18 shows the detection efficiency in each position. The efficiency is more than 99 % even at the edge. The right side edge of the scintillator is also tested and there is no difference compared with the central part, as shown in Fig. 4.19.

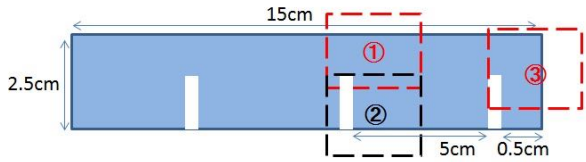

Figure 4.15: Position of the beam injected to the scintillator with machining

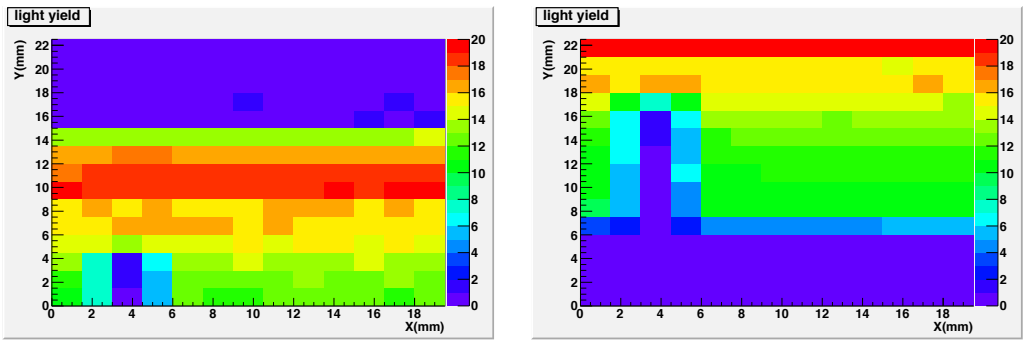

Figure 4.16: Mean light yield of the scintillator with machining in each position. Left (right) plot corresponds to ① (②) in Fig. 4.15.

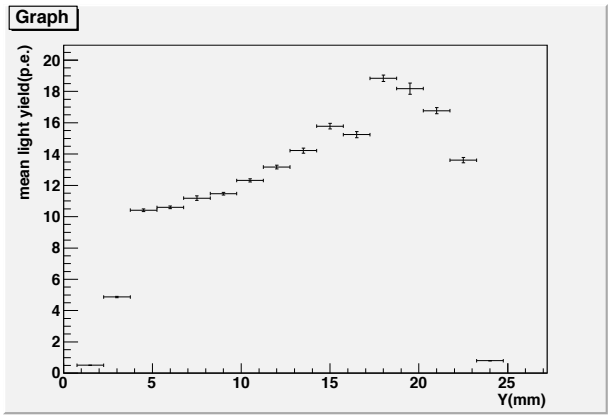

Figure 4.17: Mean light yield of the scintillator with machining along with Y axis. The fiber is in Y=16 mm. The error bars are only statistical error.

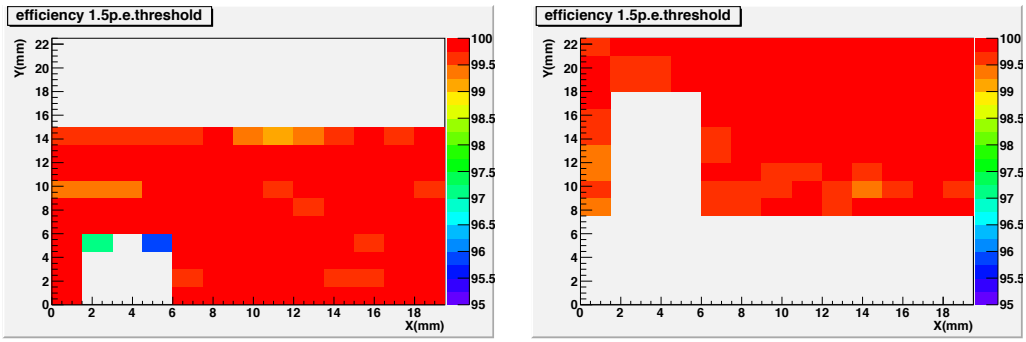

Figure 4.18: Detection efficiency of the scintillator with machining in each position. Threshold is 1.5 p.e. Left (right) plot corresponds to ① (②) in Fig. 4.15.

4.3.3 Summary

Table 4.4 shows the summary of the measured parameters for the 3 mm thickness scintillator. A light yield in the table is defined as the mean light yield at the position which maximizes the light yield. We also confirm the efficiency of the 3 mm thickness scintillator is above 99 % at any position for straightly injected minimum ionization particle and this is enough to be used in the central detector.

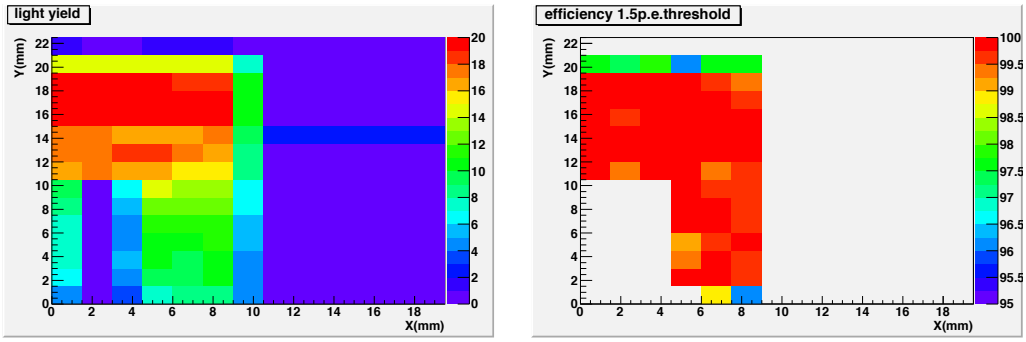

Figure 4.19: Mean light yield (left) and their efficiency (right) at the edge of the scintillator with cut. They correspond to ③ in Fig. 4.15.

Table 4.4: Measured parameters for the 3 mm thickness scintillator

Parameters	without machining	with machining
Light yield per MIP	24 p.e.	18 p.e.
Attenuation length along with Y-axis	30 mm	25 mm

Chapter 5

Expected performance of the detector

5.1 Detector simulation

The performance of the detector is evaluated by using Monte Carlo simulation. The neutrino beam line and neutrino interaction are simulated by JNUBEAM and NEUT, in the same way as Chapter 3. The simulation of the behavior of the secondary particles in the detector is simulated by using Geant4. The simulation is based on the code originally developed for the INGRID.

5.1.1 The central detector

Each target is simulated as a $100\times100\times50$ cm^3 rectangular solid.

The scintillators inside the target are arranged as shown in Fig. 3.21. Each scintillator is simulated as a 1000 mm$\times$24 mm$\times$3 mm rectangular solid. The width is 24 mm, not 25 mm, assuming the width of the reflector. The groove and cut of the scintillator is implemented.

The scintillators around the target are placed 10 cm from the edge of the target. Each TOF scintillator is simulated as an octant based on the simulation in INGRID. The hole of the TOF scintillator to put a fiber is simulated.

The support structure is not simulated.

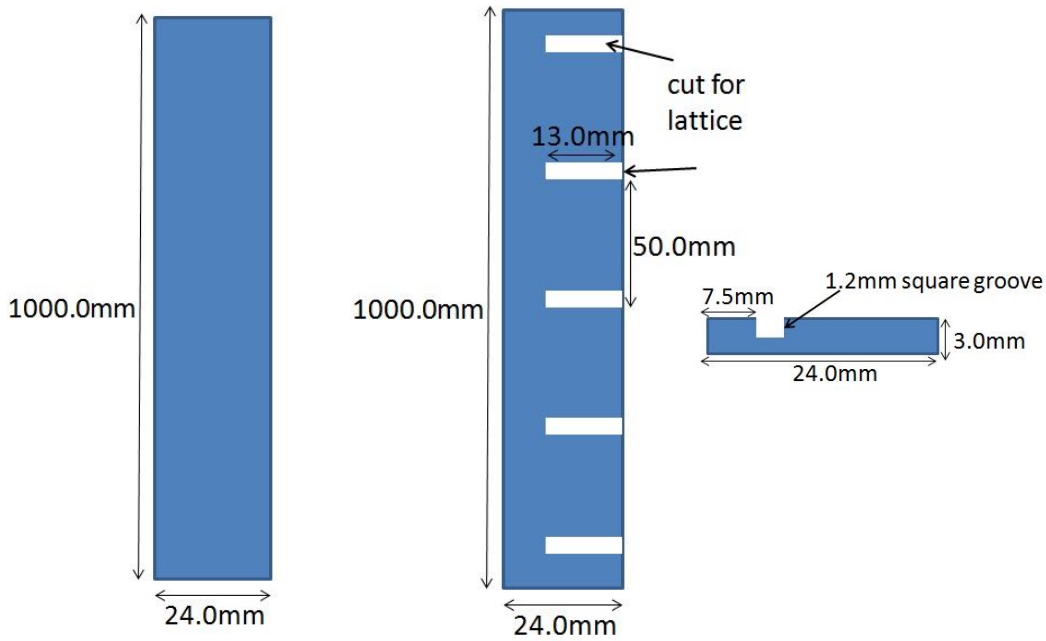

Figure 5.1: Each scintillator of X and Y layer (left) and lattice layer (middle). Their groove is simulated (right).

5.1.2 MRDs

The iron plate in the side MRDs is simulated as a 3×180×320 cm^3 rectangular solid. Ten iron plates are arranged at an interval of 2 cm. The distance between the first iron plate and the target is 60 cm.

The iron plate in the downstream MRD is simulated as a 3×180×320 cm^3 and 6×180×320 cm^3 rectangular solid. Ten 3 cm iron plates and ten 6 cm iron plates are arranged at an interval of 2 cm. The distance between the first iron plate and the target is 60 cm.

The scintillators are set between the iron plates. They are simulated as a 0.7×180×20 cm^3 rectangular solid. They are arranged between iron plates parallel to the y-axis. The hit position along with y-axis is measured by using timing information, however, it is not implemented yet.

The support structure is not simulated.

5.1.3 Scintillator, wavelength shifting fiber and MPPC

If secondary particles lose their energy in the scintillators, the emission of the scintillation light, absorption into wavelength shifting fibers, propagation in wave length shifting fiber and detection by MPPCs are simulated. A crosstalk and afterpulse of MPPC are also simulated. These tuning are based on the measurement, described in Chapter 4. A dark noise of the MPPC is not implemented.

5.1.4 Experimental hall

For background study, wall and floor of the experimental hall are simulated as shown in Fig. 5.2. Engineering drawing of the hall is used as a reference. Neutrino interaction point is simulated inside $5 \times 10 \times 5$ m^3 volume in the wall and $10 \times 4 \times 10.5$ m^3 volume in the floor. We measure the background events from hall at the candidate site of the WAGASCI by using one of the INGRID module. Based on the measurement, the total number of such background events is tuned.

5.1.5 Summary of parameters in the simulation

Table 5.1 shows the summary of the parameters used for this simulation.

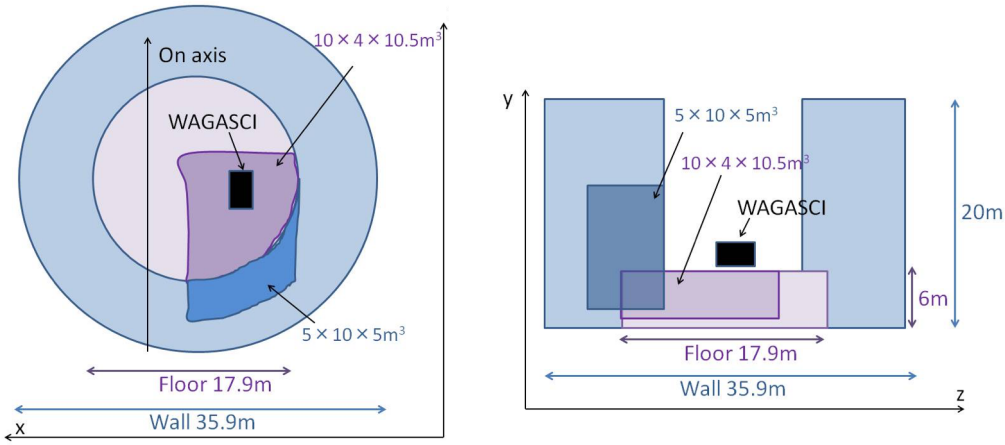

Figure 5.2: Top view (left) and side view (right) of the wall and floor simulated in MC

Table 5.1: Parameters for simulation

Water target	material	H_2O
	density	$1.00g/cm^3$
Hydrocarbon target	material	C_9H_{10}
	density	$1.03g/cm^3$
Iron	material	Fe
	density	$7.87g/cm^3$
Wall and floor	material	$O(53\%), Si(34\%), metals(13\%)$
	density	$2.2g/cm^3$
Scintillator	material	C_9H_{10}
	density	$1.03g/cm^3$
	light yield	41.3 p.e./MeV (central)
		22.6 p.e./MeV (TOF)
		22.6 p.e./MeV (MRD)
	attenuation length	25.0 mm (central)
	due to the distance	10.4 mm (TOF)
	from the fiber	not implemented (MRD)
	timing resolution	2.0 ns (central)
		1.0 ns (TOF)
		1.7 ns (MRD)
Fiber	attenuation length	241 cm
	velocity of the light	28.0 cm/ns
MPPC	crosstalk and afterpulse rate	0.05

5.2 Track reconstruction

Figure 5.3 shows an event display of the CCQE interaction on the central detector. What we can get is only the information of hits of the scintillators. To select neutrino interaction from the hit information, track reconstruction algorithm is developed. The reconstruction methods is based on that of INGRID and Proton Module [16]. Especially, in the central detector, scintillator is arranged like 3D-grid. For this new structure, reconstruction method is improved. The flow of the track reconstruction is as follows:

1. Two-dimensional track reconstruction
2. Track matching with MRD
3. Three-dimensional track reconstruction

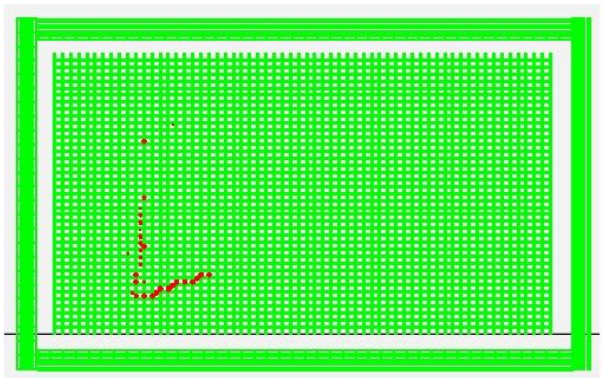

Figure 5.3: An event display of CCQE interaction. Green lines are scintillators and red circle is the light yield in each channel.

5.2.1 Two dimensional track reconstruction

The tracks in x-z and y-z view are reconstructed independently. Track reconstruction algorithm is based on Cellar automaton, which has been used in K2K and T2K. It is a discrete calculation model composed of many cell. In the central detector, the algorithm is used along with z and x (y) axis to reconstruct high angle track. Figure 5.4 shows an example of the reconstructed track. Channels having ADC signal more than 1.5 p.e. are defined as hits and the tracks having more than 2 hits are reconstructed. Each reconstructed track is fitted by a linear function. In the MRDs, the algorithm is used along with z axis.

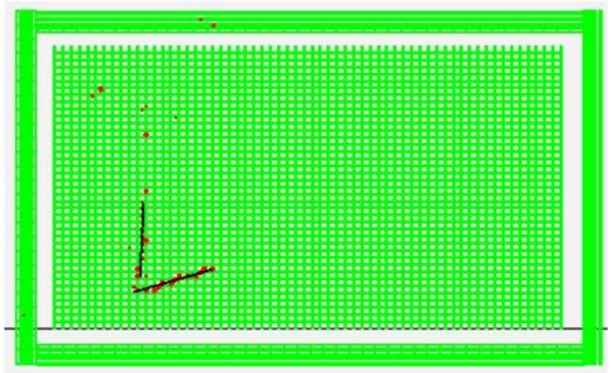

Figure 5.4: An event display of CCQE interaction. Black lines are reconstructed tracks. Green lines are scintillators and red circle is the light yield in each channel.

5.2.2 Track matching with MRD and TOF plane

When two-dimensional tracks are reconstructed both in the central detector and MRD, the matching between the central detector and MRD tracks is checked. Hits in TOF planes matched with the track in the central detector is also checked. The x-y view track in the side MRDs and WAGASCI y-z view track are jointed after three dimensional track reconstruction because side MRDs do not have y-z view.

5.2.3 Three-dimensional track matching

The three-dimensional tracks are searched among the pairs of two-dimensional tracks. If difference of the upstream Z position of a X track and a Y track is smaller than three layers, they are combined into a three-dimensional track. This three-dimensional track matching is examined separately among MRD-matched tracks and MRD-non-matched tracks. Starting point z of the MRD-matched track is determined by the position of the most upstream (downstream) hit scintillator for forward scattering (backward scattering) track. Starting point of x and y is calcurated by the result of the z position and result of the linear fitting at each view.

5.3 Signal and background

A signal is defined as CC interaction with H_2O or CH target. The dominant background source is muons produced by neutrino interaction on the MRDs

and experimental hall. They are rejected by TOF and fiducial volume cut. In addition, NC interaction on the targets and interaction of neutral particles, such as neutron and gamma, are background sources which can not be rejected by such cuts because neutral particles are not observed by scintillators in WAGASCI. These backgrounds are separated from signals of muons by using the MRDs.

5.4 Event selection

The flow of the event selection is as follows:

1. Vertexing
2. Short track search
3. Track direction cut
4. Fiducial volume cut
5. Iron plate cut

5.4.1 Vertexing

After the reconstruction of three-dimensional tracks, the vertexes of tracks are searched. If a pair of the starting points of three-dimensional MRD-matched track are within 10 cm along with x,y and z axis, they are identified as the tracks from a common vertex. The starting point of the MRD-matched track penetrating the largest number of iron plates from the common vertex is identified as the reconstructed vertex. If there is no three-dimensional MRD-matched track, the event is rejected.

5.4.2 Short track search

Short tracks from the reconstructed vertexes are searched to reconstruct secondary particles, like protons and pions. If a reconstructed vertex and starting point of a three-dimensional MRD-non-matched track are within 10 cm along with X,Y and Z axis, this track is associated with the reconstructed vertex. Two dimensional track from the reconstructed vertex is also searched with the same rule.

5.4.3 Track direction cut

The direction of the reconstructed track is determined by the timing information of the TOF scintillators. The tracks going out from the target are selected. Figure 5.5 shows the time difference between the central detector and the left side MRD. The direction of travel of the reconstructed particle is correctly identified with the accuracy of 96.0%.

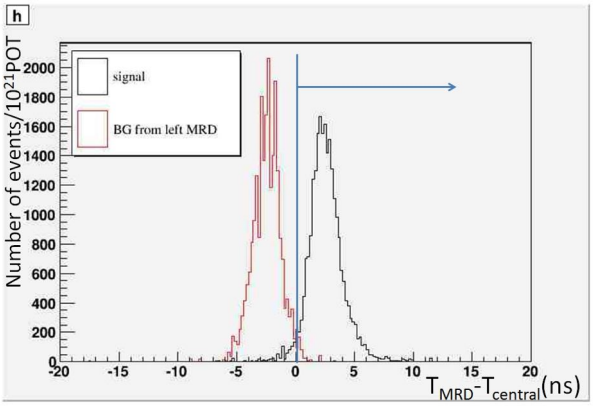

Figure 5.5: Time measured by TOF scintillators in front of the left side MRD minus Time measured by TOF scintillators just around the central detector after 3dimensional track reconstruction. Black (Red) line is the neutrino interaction on the target (left side MRD). The difference > 0 is required.

5.4.4 Fiducial volume cut

If the vertex of the track is in 5 cm from edge of target, the track is excluded to reject the background from outside as shown in Fig. 5.6. The fiducial mass is 0.65 ton.

5.4.5 Iron plates cut

To reject the background from NC and neutral particles, the tracks are required to penetrate more than four iron plates in the downstream MRD and more than one iron plates in the side MRDs, as shown in Fig. 5.7. To measure the momentum of the muon, the track is required to stop in the MRDs or penetrate all iron plates.

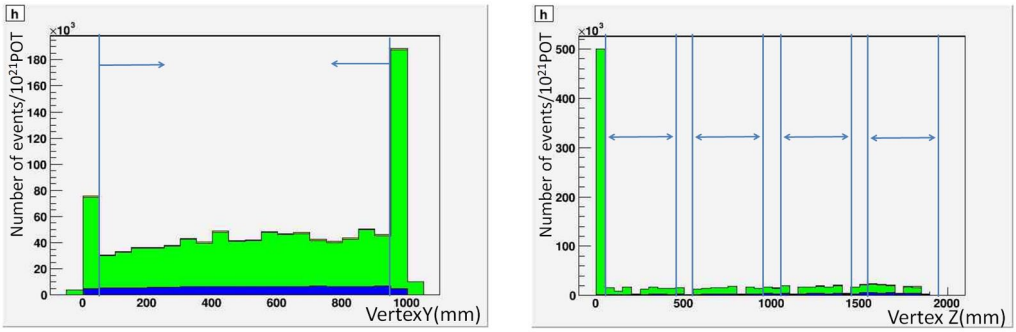

Figure 5.6: Starting point y (left) and z (right) of the reconstructed track after 3dimensional track reconstruction jointed the downstream MRD. Blue is events from the target, green is events from hall, and yellow is events from the MRDs. 5 cm from the edge of the target is rejected.

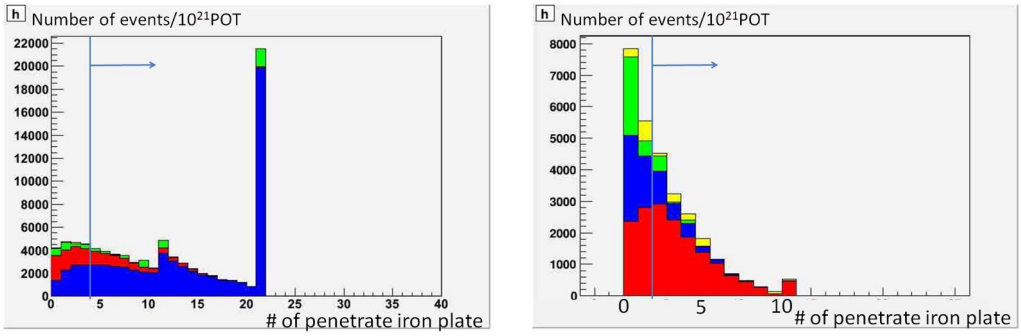

Figure 5.7: The number of the penetrate iron plates of the track in the downstream MRD (left) and side MRDs (right) after fiducial cut. Blue is muons produced inside the target, red is the particle except for muons produce inside the target, green is events from wall, and yellow is events from the MRDs.

5.5 Summary of the event selection

Table 5.2 and 5.3 show the summary of the event selection on each target. In the case of the hydrocarbon target, 2.92×10^3 CC events per 1×10^{21} POT are expected. The purity of charged current interaction is 91.0%. In the case of the water target, 2.41×10^3 CC events per 1×10^{21} POT are expected. The purity is 75.5%. The main background is neutrino interaction on the scintillators inside the water target and the fraction of CC interaction is more than 95%.

Table 5.2: Summary of the event selection on hydrocarbon target per 1×10^{21} POT

Cut	CC	NC	BG from outside	All
Track reconstruction	7.43×10^4	4.81×10^3	1.04×10^6	1.11×10^6
TOF	7.07×10^4	4.42×10^3	9.14×10^5	9.88×10^5
Fiducial	4.98×10^4	3.10×10^3	4.41×10^3	5.65×10^4
Penetrate 5 irons	3.79×10^4	1.28×10^3	1.62×10^3	4.06×10^4
Stop in MRD	3.00×10^4	1.16×10^3	1.58×10^3	3.27×10^4
Fraction after all cut	91.7%	3.5%	4.83%	100%

Table 5.3: Summary of the event selection on water target per 1×10^{21} POT

Cut	CC	NC	BG from scintillator	BG from outside	All
Track reconstruction	6.27×10^4	3.61×10^3	1.62×10^4	1.04×10^6	1.12×10^6
TOF	5.84×10^4	3.17×10^3	1.50×10^4	9.14×10^5	9.88×10^5
Fiducial	3.95×10^4	1.75×10^3	9.71×10^3	7.32×10^3	5.55×10^4
Penetrate 5 irons	3.02×10^4	9.12×10^2	7.67×10^3	2.04×10^3	4.00×10^4
Stop in MRD	2.41×10^4	8.65×10^2	6.19×10^3	1.64×10^3	3.19×10^4
Fraction after all cut	75.5%	2.71%	19.4%	5.14%	100%

5.5.1 Vertex

Figure 5.8 shows the vertex of the reconstructed track after event selection. Figure 5.9 shows the difference between reconstructed vertex and true neutrino interaction vertex. The vertex is mainly reconstructed within $\pm$ 5 cm.

5.5.2 Reconstructed angle

Figure 5.10 shows the scattering angle of the reconstructed track on the hydrocarbon and water target after the event selection. The large scattering angle events are observed. The angle resolution is around 3 degrees, as shown in Figure 5.11.

5.5.3 Number of penetrating iron plates

Figure 5.12 (5.13) shows the number of the penetrating iron plates of the longest MRD-matched track in the downstream MRD and side MRDs on hydrocarbon (water) target after the event selection.

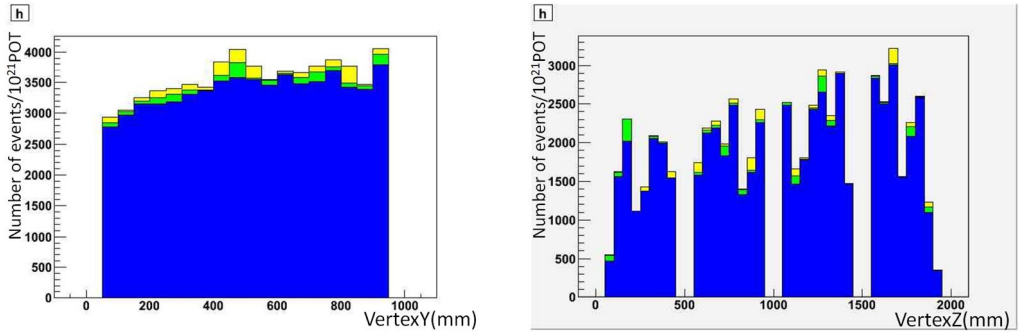

Figure 5.8: Reconstructed vertex y (left) and z (right) after the event selection. Blue is events from the target, green is events from hall, and yellow is events from the MRDs.

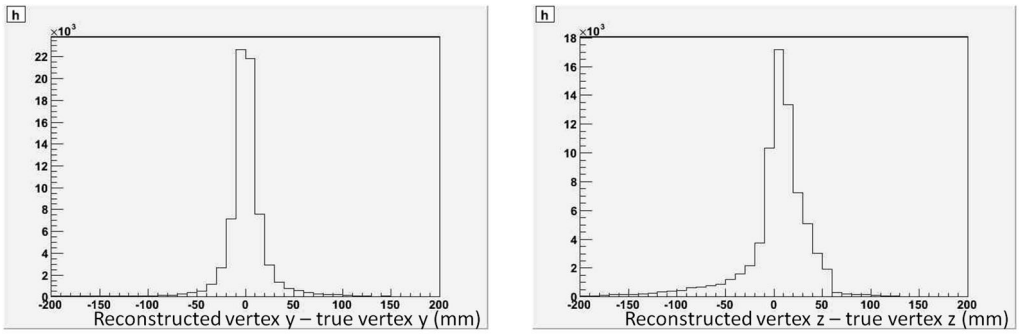

Figure 5.9: Reconstructed vertex - true vertex y (left) and z (right) after fiducial cut.

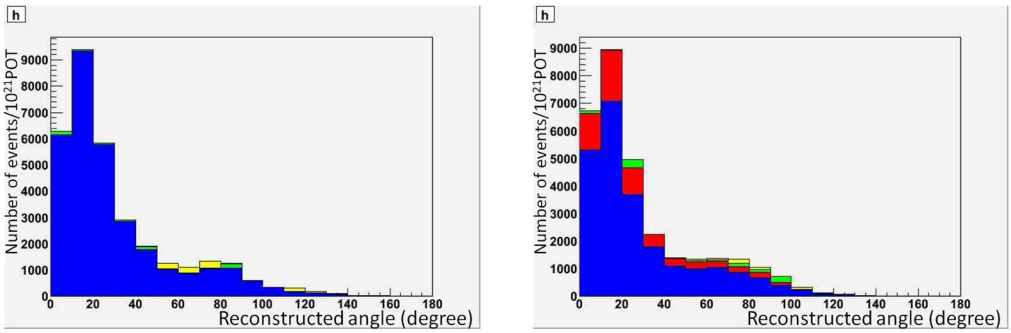

Figure 5.10: Reconstructed angle on hydrocarbon (left) and water (right) target after the event selection. Blue is events from the target, green is events from hall, yellow is events from the MRDs, and red is events from the scintillators inside the water target.

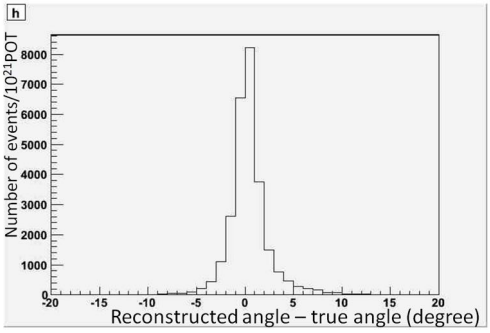

Figure 5.11: Difference between reconstructed angle and true angle on water target after the event selection.

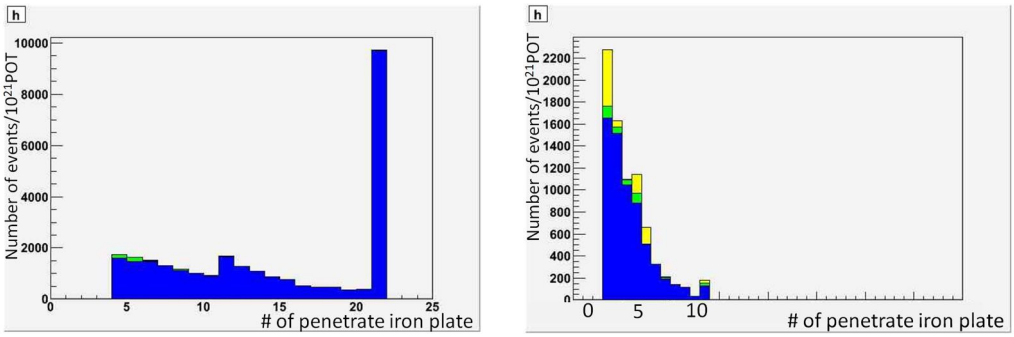

Figure 5.12: End plane of the track in the downstream MRD (left) and side MRDs (right) after iron cut on hydrocarbon target. Blue is events from the target, green is events from hall, and yellow is events from the MRDs.

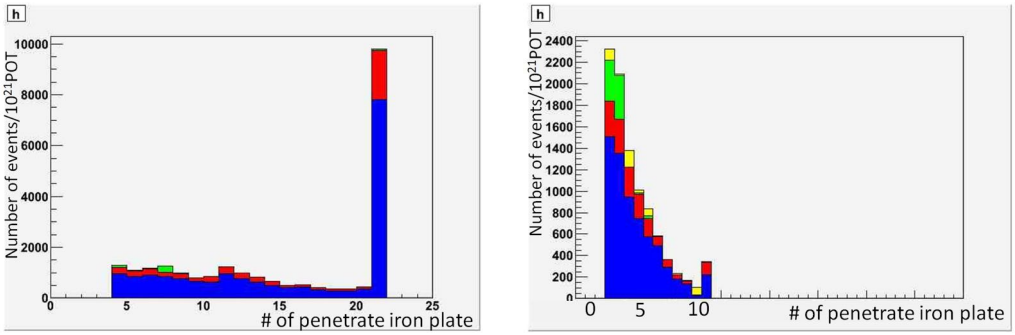

Figure 5.13: End plane of the track in the downstream MRD (left) and side MRDs (right) after iron cut on water target. Blue is events from water, red is events from scintillators, green is events from hall, and yellow is events from the MRDs.

5.5.4 Muon identification

Table 5.4 shows the kind of particles which produce the longest track from each vertex after the event selection. The fraction of muon is 85.6%. In near future, this is expected to be improved by usind dE/dX information or changing the number of the penetrated iron plates.

Table 5.4: The kind of particles which make the longest track

kind of particles	fraction
μ	85.6%
π^+, π^-	4.8%
p	4.3%
e^+, e^-	4.5%

5.5.5 Muon tagging efficiency

Figure 5.14 and 5.15 shows efficiency of muon after the event selection. The efficiency of the large scattering angle muons is lower due to the acceptance of the MRDs. In addition, it is relatively smaller than that described in Chapter 3 because three hits are required to reconstruct the track in the central detector. The efficiencies are different between hydrocarbon target and water target due to the acceptance of the MRD.

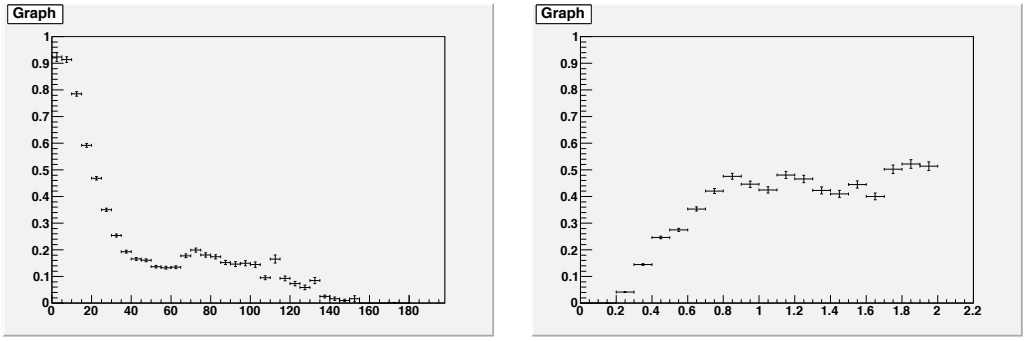

Figure 5.14: Efficiency of the muons as a function of their true angle (left) and momentum (right) on hydrocarbon target after the event selection

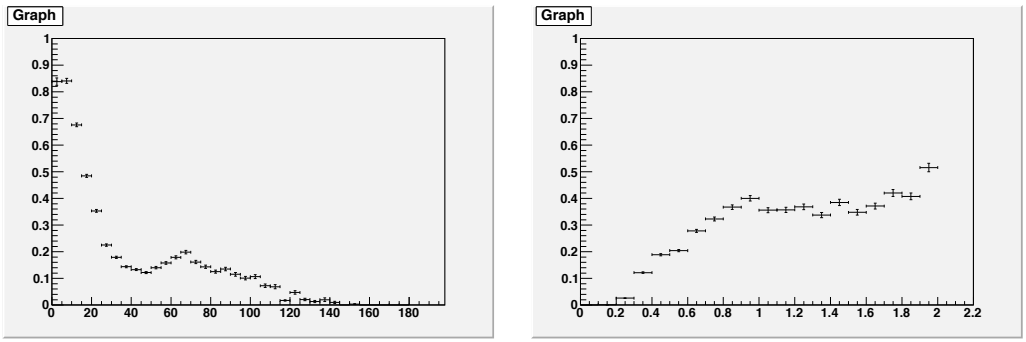

Figure 5.15: Efficiency of the muons as a function of their true angle (left) and momentum (right) on water target after the event selection

Chapter 6

Cross section measurement and sensitivity to neutrino interaction model

The primary motivation of the WAGASCI experiment is to measure charged current cross section on H_2O, CH and their ratio. In this chapter, the performance of WAGASCI on cross section measurement is estimate. The event selection method is described in Chapter 5.

6.1 Charged current cross section measurement

6.1.1 Charged current cross section on hydrocarbon

The cross section on hydrocarbon is calculated by Eq. 6.1.

$$X_{CH} = \frac{N_{CH} - N_{OutBGCH}}{\Phi_{CH} T_{CH} \varepsilon_{CH}} \tag{6.1}$$

where N_{CH} is the number of selected events in data, $N_{OutBGCH}$ is the number of the background events expected by MC simulation, Φ_{CH} is the muon neutrino flux at the hydrocarbon target, T_{CH} is the number of target nucleons and ε_{CH} is the detection efficiency for charged current interaction on hydrocarbon target.

Table 6.1 shows the neutrino interaction mode after the event selection. Figure 6.1 shows detection efficiency of neutrino. Figure 6.2 shows the momentum and scattering angle of the muons after the event selection.

Table 6.1: Fraction of the neutrino interaction mode for hydrocarbon target events after the event selection

Interaction mode	events/1×10^{21}POT	fraction
CCQE	1.35×10^4	41.2%
CC1π	8.49×10^3	25.9%
CCDIS,multiπ	7.45×10^3	22.7%
CCcoh	6.90×10^2	2.1%
NC	1.16×10^3	3.5%
BG from outside	1.58×10^3	4.8%

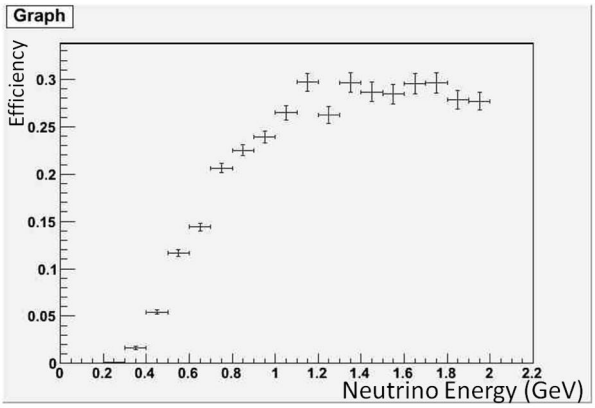

Figure 6.1: Selection efficiency as a function of the energy of the neutrino from hydrocarbon target after the event selection

6.1.2 Charged current cross section on water

For the water target events, the background from interaction with scintillators has to be subtracted by using the measurement of the hydrocarbon target. However, the efficiency on water target and hydrocarbon target is different due to the acceptance of the MRDs and it gives an additional systematics error. To reduce this difference, additional cut is applied to the events on the hydrocarbon target. As shown in Fig. 6.4, an imaginary MRD is defined 50 cm behind the downstream MRD. The reconstructed tracks from hydrocarbon target are extended to the downstream and are required to reach the imaginary MRD. Figure 6.5 shows the detection efficiency after the imaginary cut and their ratio.The difference is less than 5% in the main energy region. The cross section is calculated by Eq. 6.2.

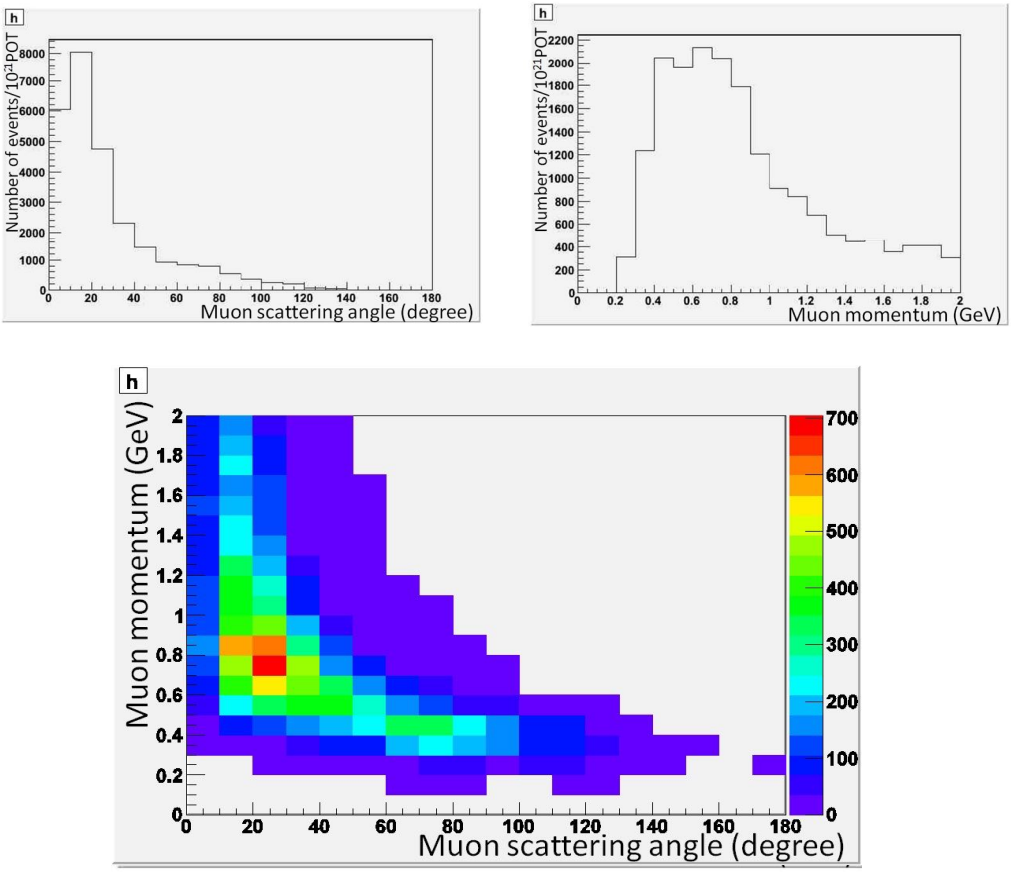

Figure 6.2: True angle (upper left), momentum (upper right) and angle vs momentum (lower middle) of the muons from hydrocarbon target after the event selection.

$$X_{H_2O} = \frac{N_{H_2O} - N_{OutBGH_2O} - N_{BGscinti}}{\Phi_{H_2O} T_{H_2O} \varepsilon_{H_2O}} \tag{6.2}$$

where $N_{BGscinti}$ is the number of the background events on the scintillator given as follows.

$$N_{BGscinti} = \Phi_{scinti} T_{scinti} \varepsilon_{scinti} X_{CH} \tag{6.3}$$

$$= \frac{\Phi_{scinti} T_{scinti} \varepsilon_{scinti}}{\Phi_{CH} T_{CH} \varepsilon_{CH}} (N_{CH} - N_{OutBGCH}) \tag{6.4}$$

Table 6.2 shows the neutrino interaction mode after the event selection. Figure 6.3 shows the neutrino selection efficiency after the event selection.

Figure 6.6 shows the momentum and scattering angle of the muons after the event selection.

Table 6.2: Fraction of the neutrino interaction mode for hydrocarbon target events after the event selection

Interaction mode	events/1×10^{21}POT	fraction
CCQE	1.08×10^4	33.8%
CC1π	6.83×10^3	21.4%
CCDIS,multiπ	5.70×10^3	17.8%
CCcoh	5.60×10^2	1.7%
NC	8.65×10^2	2.7%
BG from scintillator	6.19×10^3	19.4%
BG from outside	1.64×10^3	5.1%

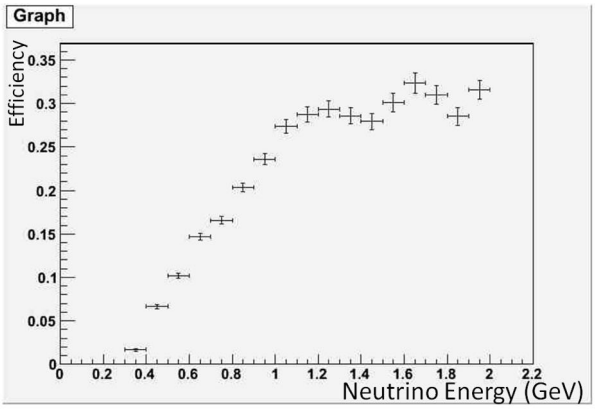

Figure 6.3: Selection efficiency as a function of the energy of the neutrino from water target after the event selection

6.1.3 Sensitivity to neutrino interaction model

In WAGASCI, more than 7.0×10^3 CC events are expected per one year and the statistical error is 2% and differential cross section can be measured statistically. The expected systematic error is around ten percents mainly due to the uncertainty of the neutrino flux.

Fig. 6.7 and 6.8 show the muon scattering angle and momentum on H_2O target with RFG and SF. In the angular distribution and momentum distribution around 200 MeV, there is a large difference more than a few percent

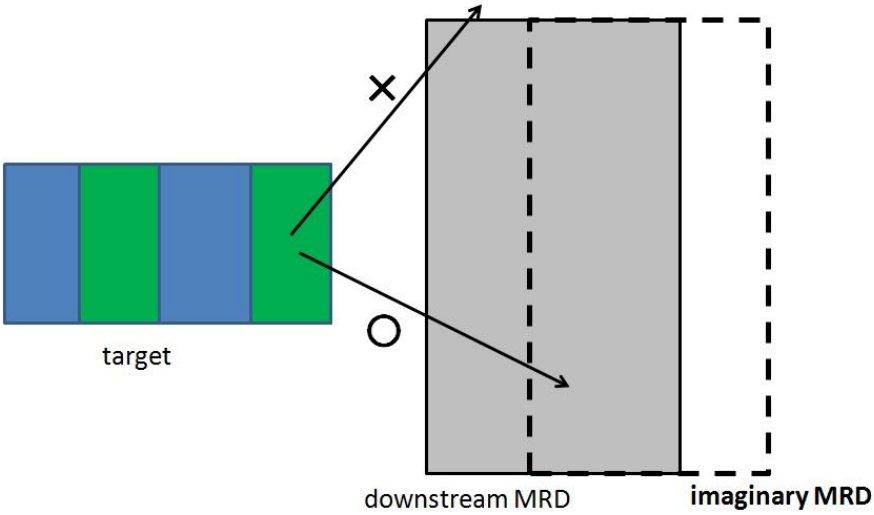

Figure 6.4: Top view of the imaginary MRD

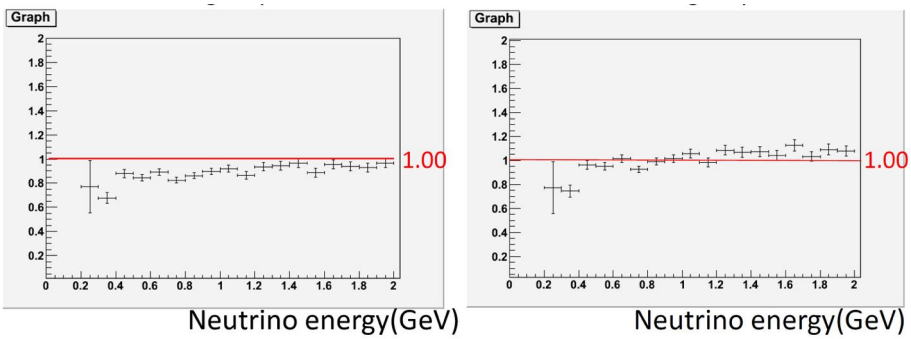

Figure 6.5: Neutrino detection efficiencies ratio between H_2O and CH target, before additional cut (left) and after additional cut (right)

between the models. If the discrepancy between model and nature exist, WAGASCI may measure it and limit the model.

In addition, as described in Chapter 2, it is important to check the correctness of the model of CCQE. This measurement can validate it by measuring large scattering angle muons on hydrocarbon and water target. In present analysis, external experimental data is used for fitting the parameters of CCQE interaction. Instead of the external data, we can use the result of WAGASCI. Better comparison between data and model is expected because used neutrino flux is almost same as that in T2K and type of the detector is

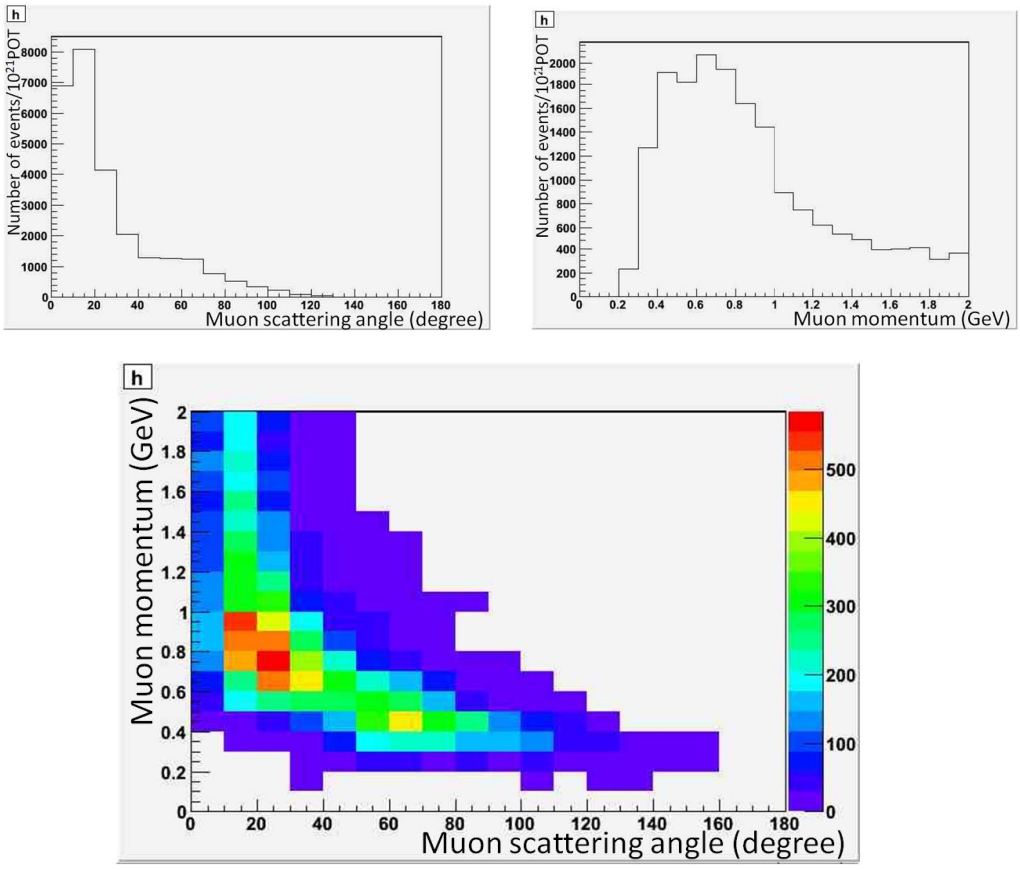

Figure 6.6: True angle (upper left), momentum (upper right) and angle vs momentum (lower middle) of the muons from water target after the event selection

similar to T2K near detector.

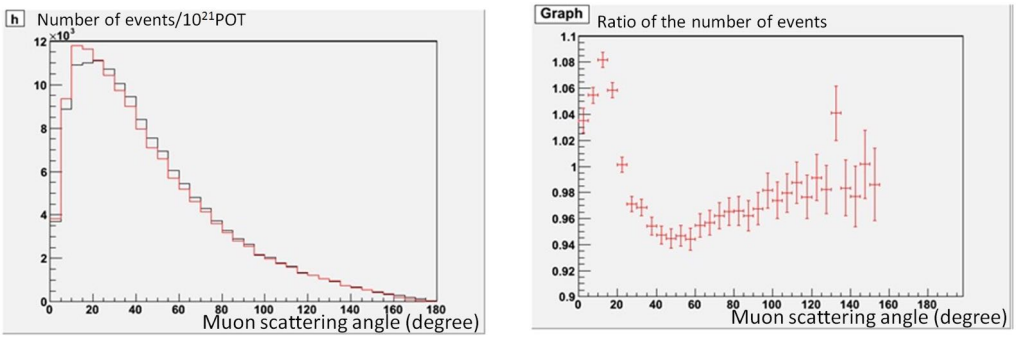

Figure 6.7: Scattering angle of muons on H_2O target (left) in the case of RFG (black) and SF (red) and their ratio (right). Error bar is the statistic of MC.

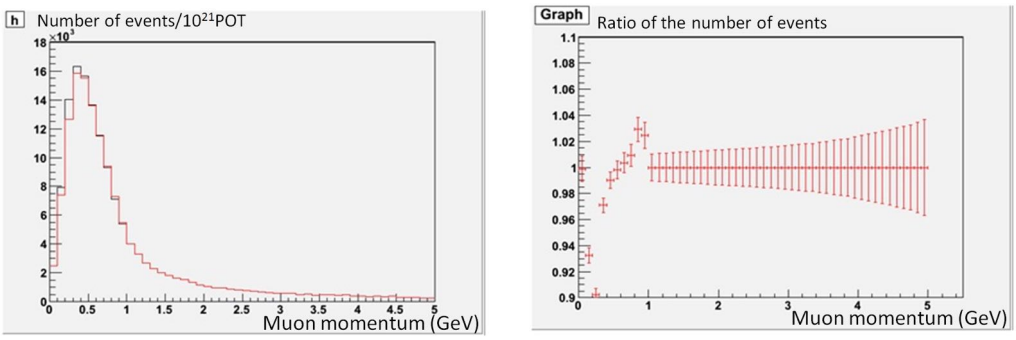

Figure 6.8: Momentum of muons on H_2O target (left) in the case of RFG (black) and SF (red) and their ratio (right). Error bar is the statistic of MC.

6.2 Charged current cross section ratio measurement

For the cross section ratio measurement, event selection is the same as that of the measurement of the cross section on water. Then, the neutrino interaction mode and muon momentum and scattering angle after the event selection is same as Table 6.2 and Fig. 6.6. Imaginary cut is applied to the events on the hydrocarbon target. The cross section ratio is calculated as follows:

$$\begin{aligned} X_{H_2O}/X_{CH} &= \frac{\Phi_{CH}T_{CH}\varepsilon_{CH}}{\Phi_{H_2O}T_{H_2O}\varepsilon_{H_2O}}\frac{N_{H_2O}-N_{OutBGH_2O}-N_{BGscinti}}{N_{CH}-N_{OutBGCH}} \\ &= \frac{\Phi_{CH}T_{CH}\varepsilon_{CH}}{\Phi_{H_2O}T_{H_2O}\varepsilon_{H_2O}}\frac{N_{H_2O}-N_{OutBGH_2O}-\frac{\Phi_{scinti}T_{scinti}\varepsilon_{scinti}}{\Phi_{CH}T_{CH}\varepsilon_{CH}}(N_{CH}-N_{OutBGCH})}{N_{CH}-N_{OutBGCH}} \end{aligned} \tag{6.5}$$

6.2.1 Estimation of error

We roughly estimate the statistical and the systematics error below.

Statistical error

For simplify, $N_{OutBGCH} = N_{OutBGH_2O} = 0$ is assumed. The statistical error is given as follows:

$$\frac{\sigma^{stat}_{X_{H_2O}/X_{CH}}}{X_{H_2O}/X_{CH}} = \frac{\sqrt{\frac{1}{N_{CH}^2}\sigma^2_{N_{H_2O}} + \frac{(N_{H_2O}-\beta N_{CH})^2}{N_{CH}^4}\sigma^2_{N_{CH}} + \beta^2\frac{1}{N_{CH^2}}\sigma^2_{N_{CH}} + \sigma^2_{N_{BGscinti}}}}{N_{H_2O}-\beta N_{CH}} \tag{6.6}$$

where

$$\beta = \frac{\Phi_{scinti}T_{scinti}\varepsilon_{scinti}}{\Phi_{CH}T_{CH}\varepsilon_{CH}} \tag{6.7}$$

As shown in Fig. 3.13 and 6.5, $\frac{\Phi_{scinti}\varepsilon_{scinti}}{\Phi_{CH}\varepsilon_{CH}} \sim 1$ can be assumed. $\frac{T_{scinti}}{T_{CH}} = 0.21$ then $\beta \cong 0.21$. By the assumption of $N_{H_2O} = N_{CH}$ and $\sigma_N = \sqrt{N}$,

$$\frac{\sigma^{stat}_{X_{H_2O}/X_{CH}}}{X_{H_2O}/X_{CH}} = \frac{1.7}{\sqrt{N_{H_2O}}} \tag{6.8}$$

The N_{H_2O} is expected to be more than 7.0×10^3 per one year and the statistical error is 2 %. The N_{H_2O} is expected to be 2.4×10^4 per 1×10^{21} POT. In that case, the differential cross section ratio is measured and 3000 CC events, corresponding to 3.1 % statistical error, are required in each bin. The binning of the differential cross section ratio as a function of the scattering angle of muon is 0–10, 10–20, 20–30, 30–50, 50–60, 60–80 and 80–140 degrees. The binning of the differential cross section ratio as a function of the momentum of muon is 0–0.5, 0.5–0.7, 0.7–0.9, 0.9–1.1 and above 1.1 GeV.

Systematic error

The sources of the systematic error are mainly composed of four components.

1. Neutrino flux
2. Neutrino interaction model
3. Background
4. Detector response

When the neutrino flux or neutrino interaction model is changed, Φ and ε are changed and cross section is also changed. As shown in 6.5, the related term in the cross section ratio measurement is $\frac{\Phi_{CH}\varepsilon_{CH}}{\Phi_{H_2O}\varepsilon_{H_2O}}$ and $\frac{\Phi_{scinti}\varepsilon_{scinti}}{\Phi_{CH}\varepsilon_{CH}}$. For the result of the Proton Module and INGRID [16], the uncertainty produced by these term is less than 3% because the uncertainties of the denominator and the numerator cancel. In our case, the difference of the flux and detection efficiency between water and hydrocarbon target is small at the same level, so the associated uncertainty is also expected to be less than 3%.

As shown in Table 5.2 and 5.3, the background from outside is expected to be around 5%. Even if we have 10% uncertainty of the background estimation, the resulting uncertainty on the 0.5%. The background from scintillator inside the water results in the systematic uncertainty. In Eq. 6.5, the term of the background from scintillator depends on the ratio $\frac{\Phi_{scinti}\varepsilon_{scinti}}{\Phi_{CH}\varepsilon_{CH}}$ which is expected to have small uncertainty described above.

The error of detector response is still to be estimated, but it is expected to be small because the detector is almost identical for hydrocarbon and water target.

Finally, the error is expected to be around 3%.

6.2.2 Sensitivity to neutrino interaction model

Uncertainty of nucleons momentum distribution in nucleus

In the T2K oscillation analysis, the uncertainty of the momentum distribution of nucleons in nucleus is one of the source of the dominant systematic error. In the present analysis, the error is assigned from the difference between two models, RFG and SF. It is difficult to evaluate the uncertainty correctly because no experiment has measured the neutrino cross section on CH and H_2O with the accuracy of lower than ten percent in the T2K neutrino energy region. Then, conservative error is assigned.

WAGASCI will provide the first experimental data to validate the difference between H_2O and CH. We can evaluate that uncertainty based on the cross section ratio measurement of WAGASCI, not relying on a model. The momentum and scattering angle distributions of muons at the far detector will be predicted by using the measurement of the WAGASCI and the near detector. The uncertainty of the result of WAGASCI or the difference between the model and result of WAGASCI can be used to estimate the uncertainty. It will reduce the error which is estimated conservatively at present. Figure 6.9 and 6.10 show the muon scattering angle and momentum ratio on H_2O and CH with each model. If different models are used between H_2O and CH, the ratio changes about ten percent from the case that same model is used between H_2O and CH. WAGASCI measures the cross section ratio with a 3% accuracy which is better than this uncertainty.

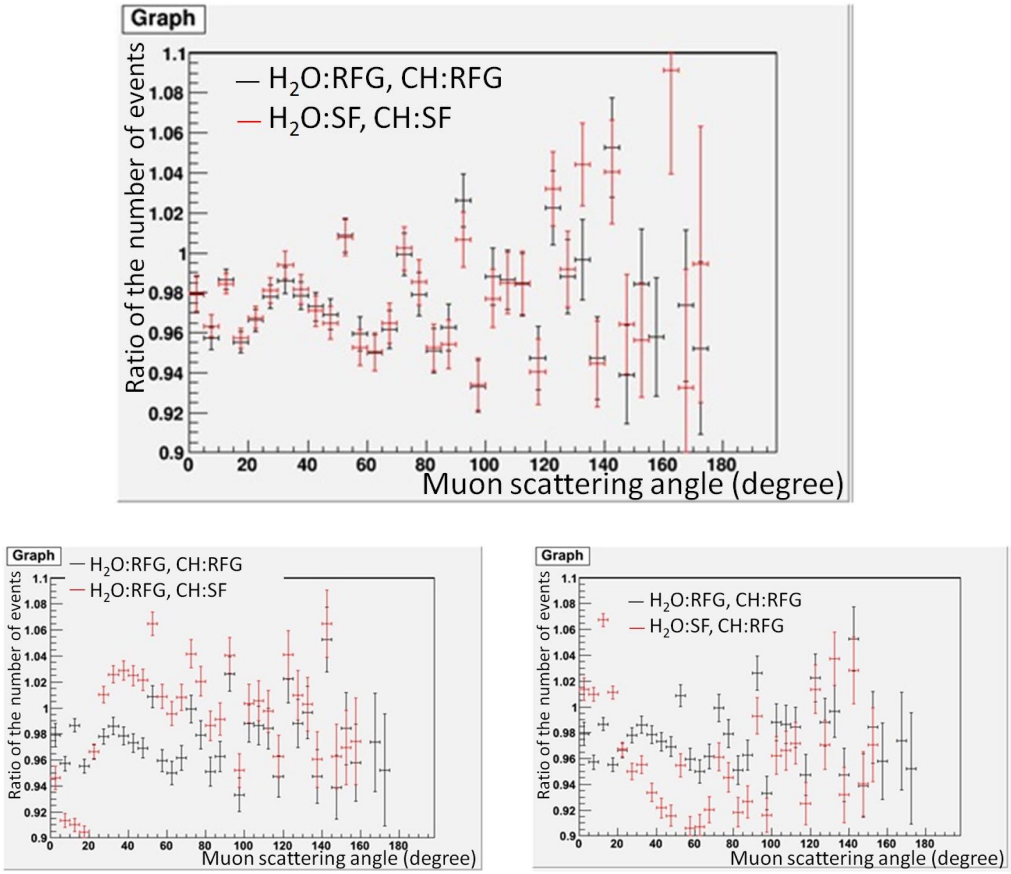

Figure 6.9: Muon scattering angle ratio on H_2O and CH with each model. The used model is H_2O:RFG CH:RFG (black), H_2O:SF CH:SF (red in upper), H_2O:RFG CH:SF (red in lower left) and H_2O:SF CH:RFG (red in lower right).

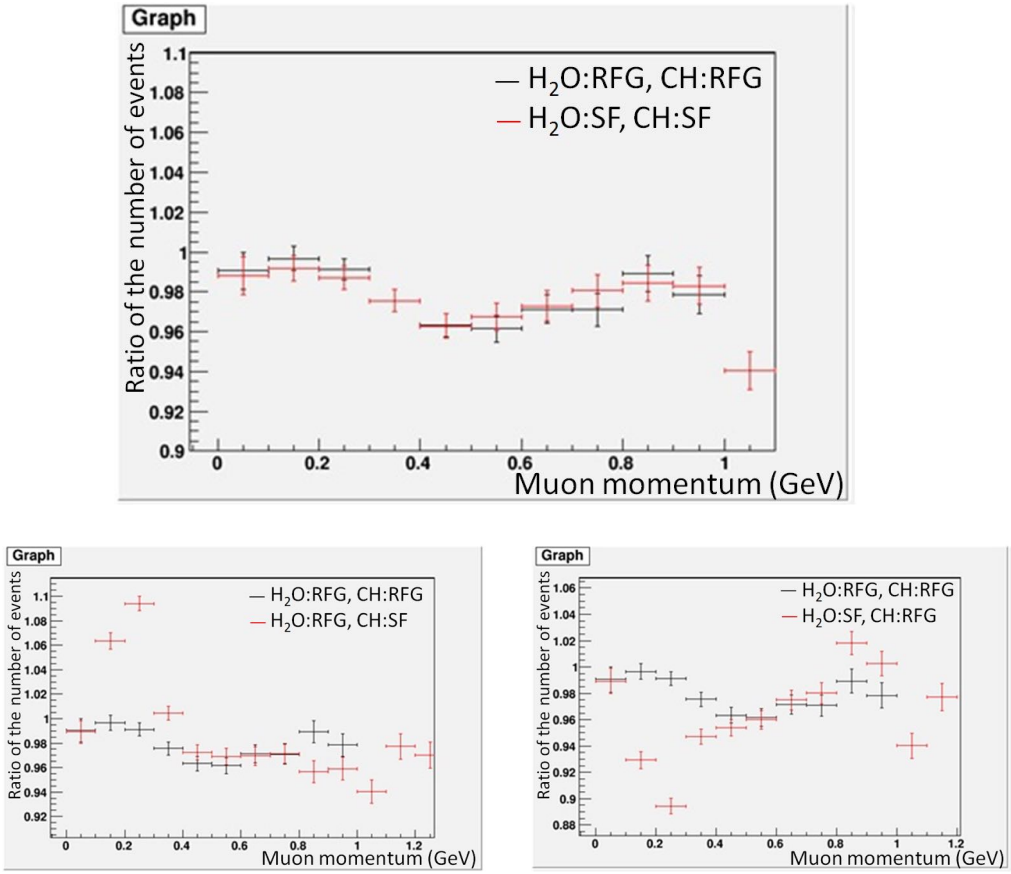

Figure 6.10: Muon momentum ratio on H_2O and CH with each model. The used model is H_2O:RFG CH:RFG (black), H_2O:SF CH:SF (red in upper), H_2O:RFG CH:SF (red in lower left) and H_2O:SF CH:RFG (red in lower right).

Fermi momentum

In T2K experiment, the uncertainty of Fermi surface momentum of the relativistic Fermi gas model is assumed to be ±30MeV, determined from electron scattering data [30]. Their nominal value is 217 MeV (carbon) and 225 MeV (oxygen). The error of the Fermi momentum is not dominant error, however, it is important to check the correctness of the model.

Figure 6.11 shows the scattering angle distribution on H_2O in each Fermi momentum. The number of forward scattering muons varies by about 2%. Figure 6.12 shows the muon scattering angle ratio on H_2O and CH with each parameters. In the small scattering angle, there is about 4% difference between the nominal case and a case that Fermi momentum of either targets is nominal +30 MeV and that of another target is nominal -30 MeV. WAGASCI can measure the cross section ratio with the accuracy of 3%, which is better than expected uncertainty, and check the correctness of the model.

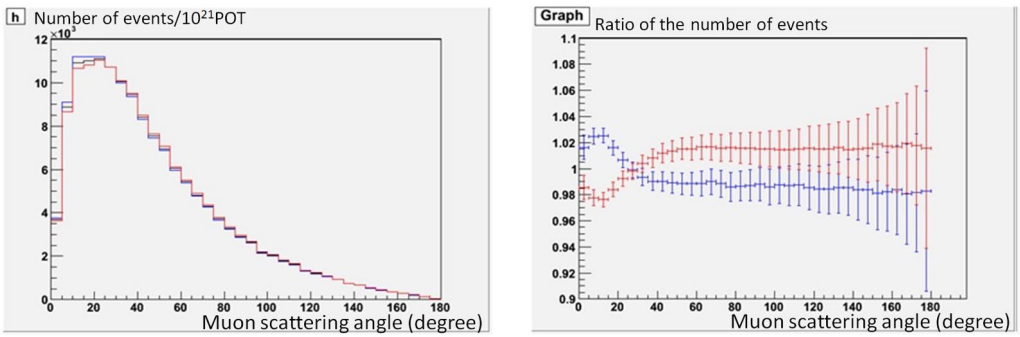

Figure 6.11: Scattering angle of muons on H_2O target (left). Black line is in case of the nominal value. Red(Blue) line is in case of the$+1\sigma(-1\sigma)$ from the nominal value. Their ratio (right)

CC coherent pion production

The cross section of CC coherent pion production (CCcoh) is small and not measured well. In T2K experiment, the uncertainty of the normalization of the CC coherent interaction is 100% [30]. The error of the CCcoh is also not dominant error, however, it is important to check the correctness of the model.

Figure 6.13 shows the theta distribution on H_2O target in each CCcoh normalization. The number of forward scattering muons is different about 6% in each case. Figure 6.14 shows the muon scattering angle ratio on H_2O and CH in each CCcoh normalization. The forward scattering muons

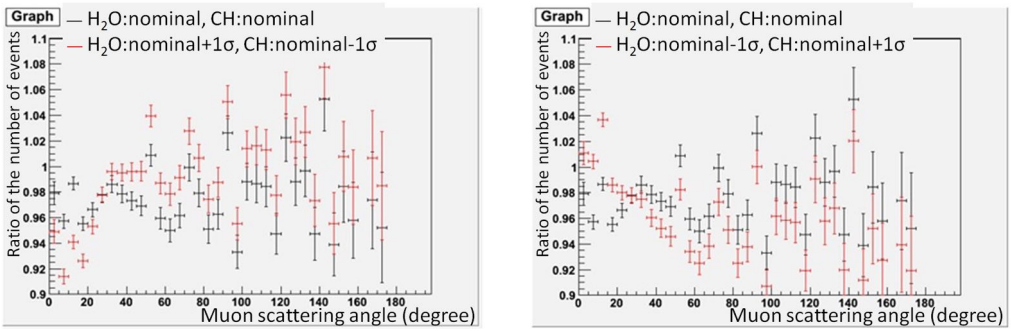

Figure 6.12: Muon scattering angle ratio H_2O and CH. The used Fermi momentum value is H_2O:nominal CH:nominal (black), H_2O:nominal+30 MeV CH:nominal-30MeV (red in left) and H_2O:nominal-30MeV CH:nominal+30MeV (red in right).

have about±10%uncertainty. In the small scattering angle, there is about 10% difference between the nominal case and a case that normalize factor of either targets is twice and that of another target is zero.

If WAGASCI measure the cross section ratio with the accuracy of 3%, we can partly correlate the normalization factor between targets and reduce the uncertainty. This is a good check of the reliability of the model. If CC coherent interaction can be selected by some additional cut, we can check the model much more.

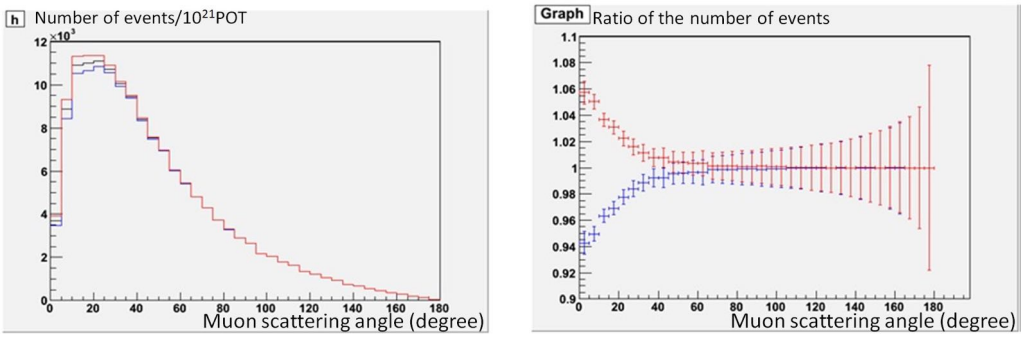

Figure 6.13: Scattering angle of muons on H_2O target (left). Black line is in case of the nominal normalization. Red(Blue) line is in case of the+100%(−100%) from the nominal normalization. Error bar of their ratio is the statistic of MC (right).

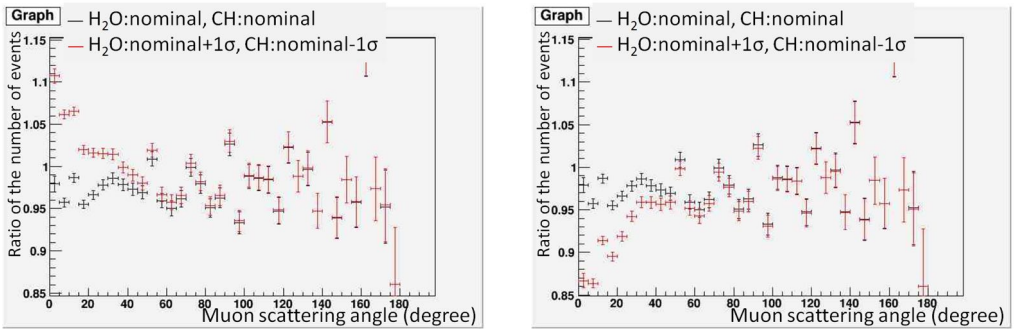

Figure 6.14: Muon scattering angle ratio H_2O and CH. The used normalization factor is H_2O:nominal CH:nominal (black), H_2O:2×nominal CH:0 (red in left) and H_2O:0 CH:2×nominal (red in right).

6.3 Exclusive-channel measurement

6.3.1 Charged current quasi-elastic interaction measurement

CCQE is the signal of the T2K experiment and it is important to measure its cross section with a large angular acceptance. In CCQE, two charged particles, a muon and a proton, are expected in the final state. Some protons are not reconstructed, only events which have one or two reconstructed tracks are selected. In this study, background from outside and on scintillator is not implemented.

one track selection

In addition to the event selection described in Chapter 5, it is required that the reconstructed vertex have only one track. Table 6.3 shows the summary of the one track event selection. 8696 CCQE events are expected and purity of CCQE is 74.7%. As shown in Fig. 6.15, low scattering angle muons can be selected by this selection. The selected track is composed of 99% muon.

Table 6.3: Summary of the event selection for charged current interaction on H_2O target

One track selection	CCQE	CC1π	CCDIS	CCcoh	NC	All
Events/10^{21}POT	8696	2026	476	162	254	11295
Fraction	74.7%	17.4%	4.0%	1.3%	2.1%	100%

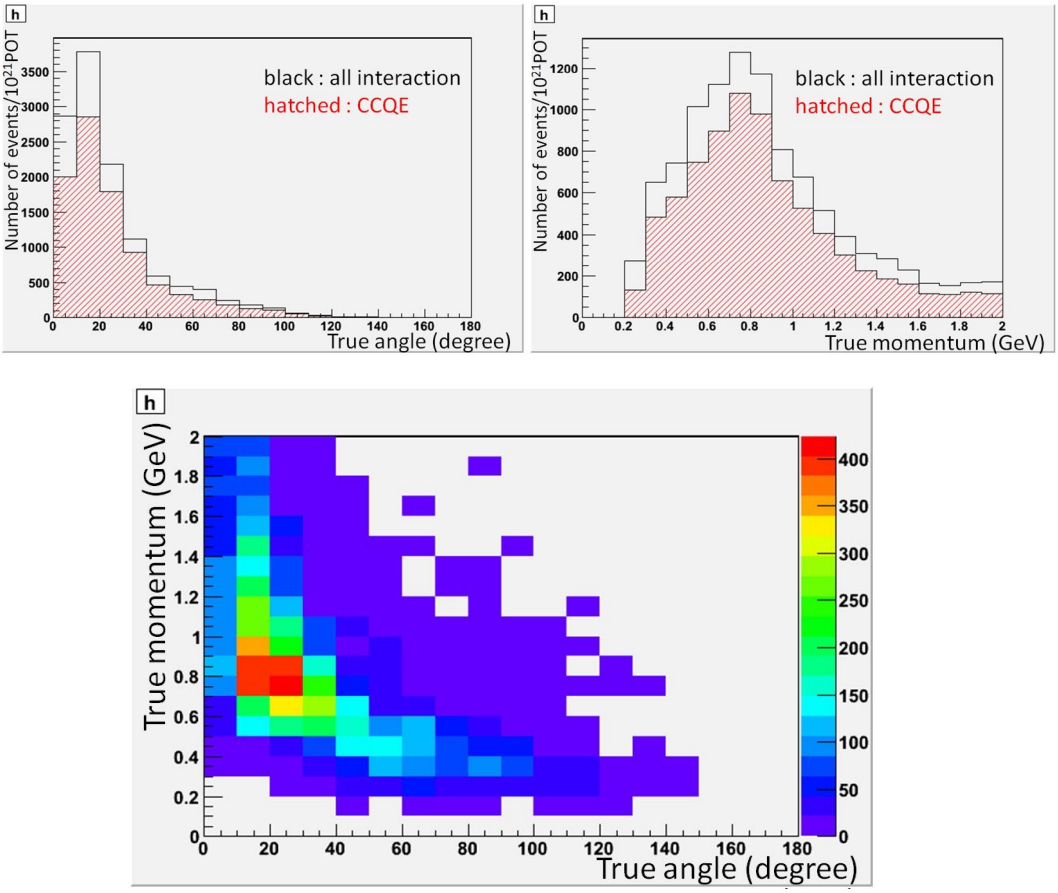

Figure 6.15: True angle (upper left), momentum (upper right) and momentum vs angle (lower middle) of track

two tracks selection

The vertex is required to have two tracks. One track is required to penetrate the iron plates more than four (one) in the downstream (side) MRD. In addition, kinematic cut is applied to enhance CCQE events. For this cut, two angles called opening angle and coplanarity angle are defined as shown in Fig. 6.16. The opening angle is required to be more than 60 degrees because in the center of mass system of CCQE, a muon and a proton are emitted back to back and small opening angle is suppressed. The coplanarity angle should be more than 150 degrees because it should be 180 degrees in CCQE if primary neutron is stopped. Table 6.4 shows the summary of the one track event selection. 2284 CCQE events are expected per 1×10^{21} POT and the purity of CCQE is 71.3%. As shown in Fig. 6.18, relatively high scattering

angle events can be selected by this selection.

In water target case, the background of scintillators should be subtracted. However, it is more difficult than the case of the inclusive charged current interaction measurement because the same detection efficiency is required between water and hydrocarbon target, not only about muon but also othe secondary particles, proton and pion. The method is to be studied in future.

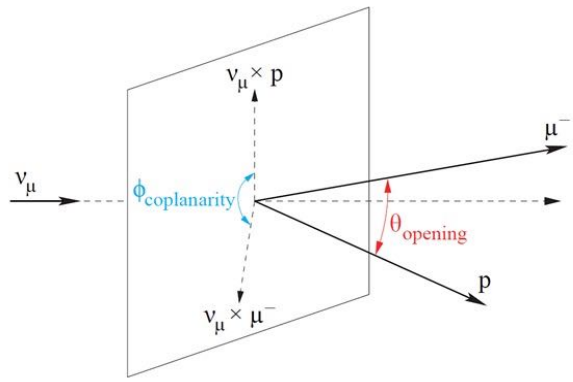

Figure 4.9: Definition of the opening angle and the coplanarity angle.

Figure 6.16: Definition of opening angle and coplanarity angle [16]

Table 6.4: Summary of the event selection for charged current interaction on H_2O

Cut	Events/10^{21}POT	CCQE	CC1π	CCDIS	CCcoh	NC
Two track selection	8246	41.9%	39.1%	11.6%	4.2%	2.7%
Opening angle cut	4107	61.3%	27.8%	7.8%	1.4%	1.4%
Coplanarity angle cut	2284	71.3%	20.5%	5.8%	1.1%	1.0%

6.3.2 future prospects

We plan to establish CC1π cross section on H_2O and CH and their ratio in order to reduce the systematic error of π less Δ decay. It is a phenomenon that Δ is produced in neutrino interaction with a nucleon and interacts nucleons in nucleus before it decays. In that case, a pion is not produced. In T2K experiment, the uncertainty of the normalization of the CC coherent

Table 6.5: The kind of particles which make the longest track

kind of particles	fraction
μ	91.0%
π^+, π^-	2.1%
p	4.0%
e^+, e^-	2.4%

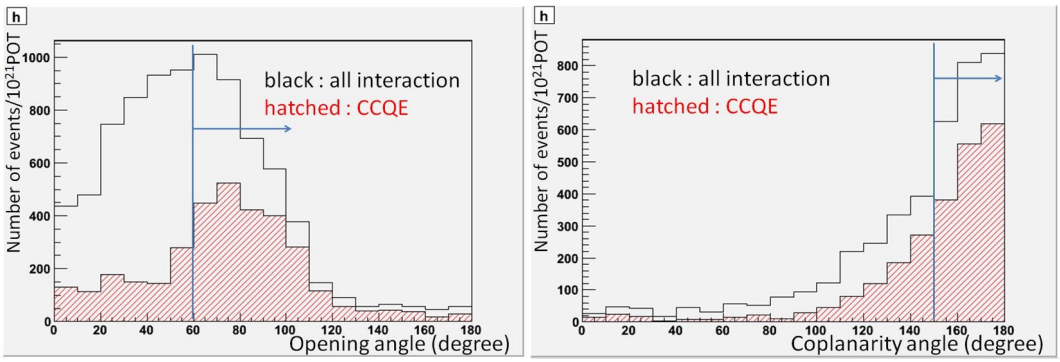

Figure 6.17: Reconstructed opening angle (left) and coplanarity angle (right).

interaction is assumed to be 100% and no correlation is assumed between near and far detector and thus no cancellation is assumed. It is one of the dominant error sources. If WAGASCI can measure the cross section with a few percent accuracy, the uncertainty is validated and the error can be reduced.

The number of emitted pions is effected by secondary interactions with nucleons in nucleus and it is difficult to select CC1π interaction. In addition, part of pions have low momentum and can not be detected. The background of scintillators should be subtracted same as the CCQE measurement. The method is to be studied in future.

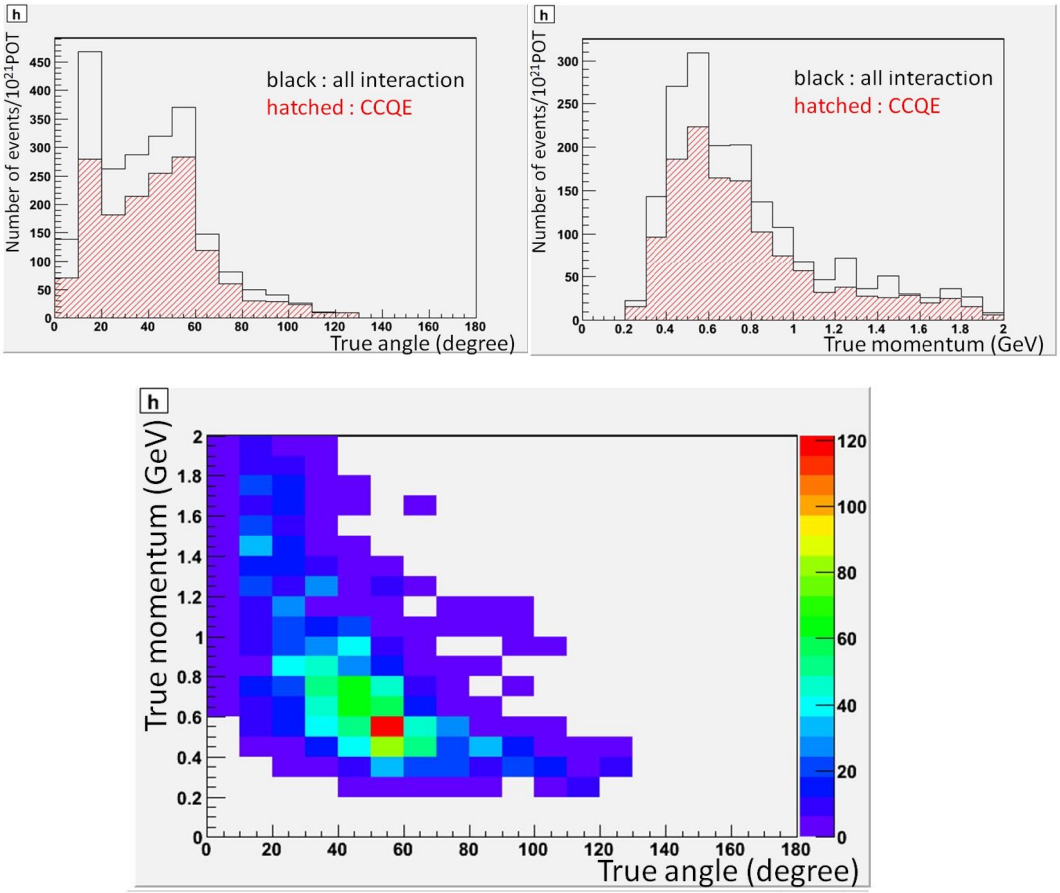

Figure 6.18: True angle (upper left), momentum (upper left) and momentum vs angle (lower middle) of track

Chapter 7

Summary and future prospects

7.1 Summary

In order to reduce the systematic errors of T2K experiment, we propose a new experiment named WAGASCI at the J-PARC neutrino beamline to measure the ratio of the charged current cross sections between water and plastic (CH) targets with a large angular acceptance. We optimize the design of the new detector by using Monte Carlo simulation. The performance of detector components, thin plastic scintillators and new low noise MPPCs, are tested and confirmed to be suitable for the new detector. The performance of the new detector is evaluated by Monte Carlo simulation based on the R&D of the detector components. The event selection criteria are developed to measure the cross sections. The expected number of charged current interaction is 7.23×10^3 per year and the cross section ratio will be measured with a total uncertainty of 3 %. Sensitivity to the neutrino interaction model is checked. WAGASCI has a possibility to reduce the error due to the uncertainty of momentum distribution of nucleons in nucleus and check the model of CCQE by detecting large scattering angle muons.

7.2 Future prospects

WAGASCI is approved by J-PARC PAC as J-PARC T59. Based on the R&D described in this thesis, several works are ongoing.

The mechanical design of the WAGASCI has been developed by LLR Ecole polytechnique group. Figure 7.1 (7.2) shows the schematic view of the mechanical structure of the central detector (MRD). The fiber bundle and connector for the wave length shifting fiber and MPPC is also designed.

A prototype of the grid layer is produced to check the mechanical sta-

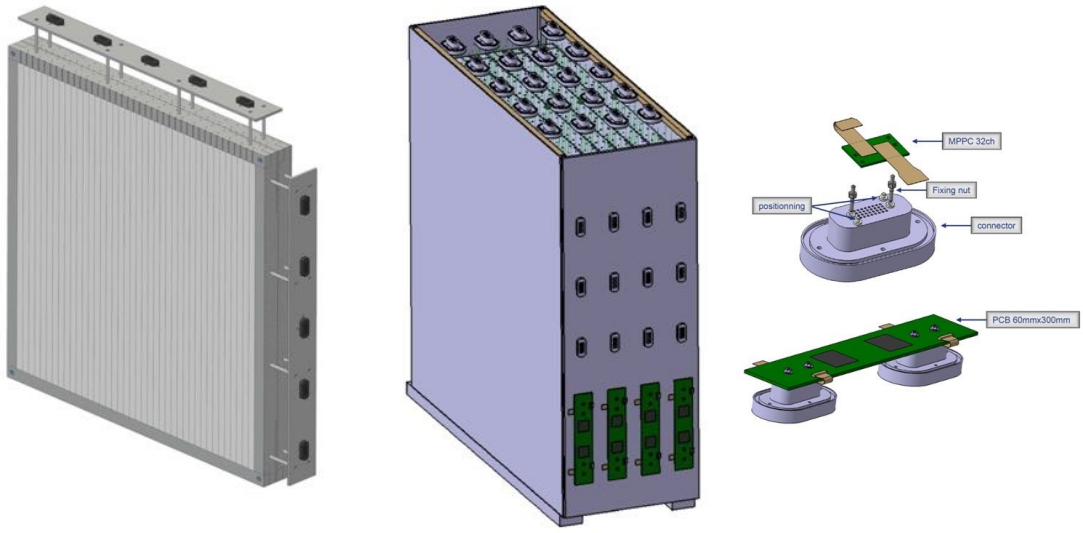

Figure 7.1: View of the central detector. Scintillators are fixed by aluminum flame (left) and compose a module (middle). The central detector is composed of two H_2O and CH modules. Right picture is a connector of the wave length shifting fiber and MPPC.

bility, as shown in Fig 7.3. Mass production of 3 mm thickness scintillators and TOF scintillators will be done in 2015. Performance test and mass production of the MRD scintillators already started by INR Moscow group (Fig. 7.4).The MPPCs used for the MRD are being produced. Towards the detector construction, we plan to work on mass evaluation of the detector component and establish an assembly procedure.

The electronics test and design of them is also ongoing by LLR group. The front-end board and DAQ have been developed based on SPIROC2 chip, which is an auto-triggered, bi-gain, 36-channel ASIC and measure the charge and time on each channel [31]. It was developed by OMEGA team for an ILC prototype hadron calorimeter.

Monte Carlo study for anti neutrino beam is also ongoing and we have an option to place a magnet at the downstream of the central detector to identify μ^+ and μ^-, as shown in Fig. 7.5. Their planning and optimization of the design is ongoing.

We plan to start the installation of the MRD in May 2016 and finish the installation of all detector August 2016. We plan to start data taking from Fall 2016.

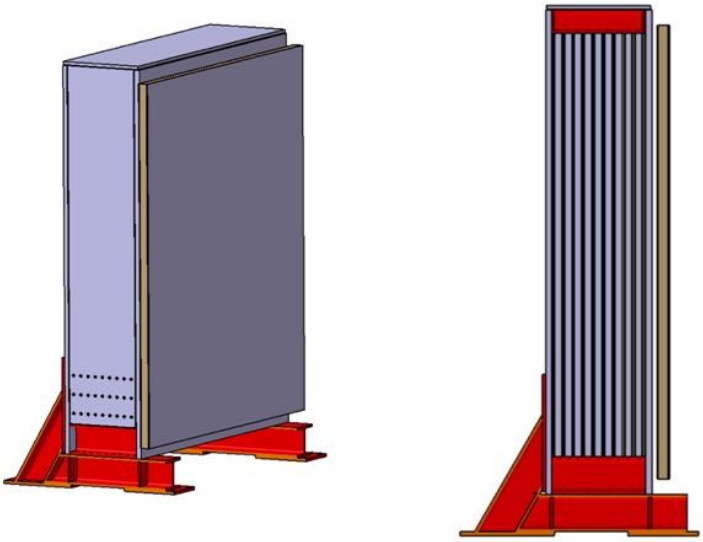

Figure 7.2: View of a mechanical design of the side MRD

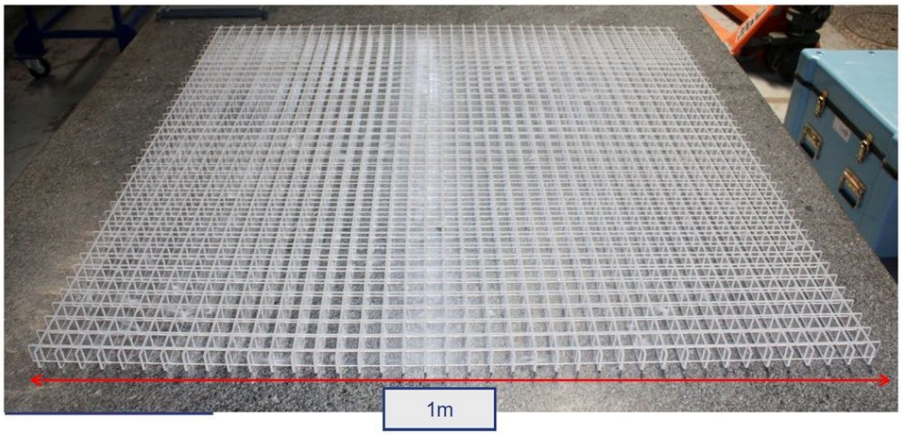

Figure 7.3: Picture of the prototype grid layer made of plastic

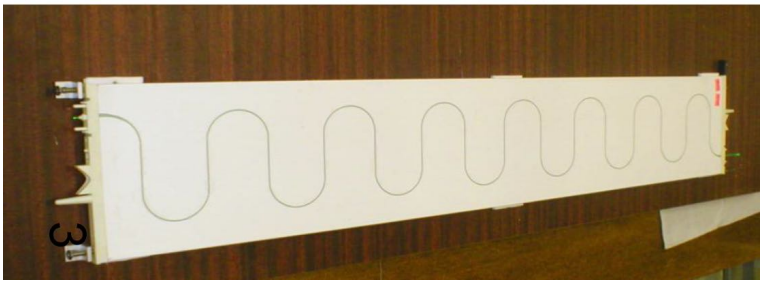

Figure 7.4: Picture of the MRD scintillator

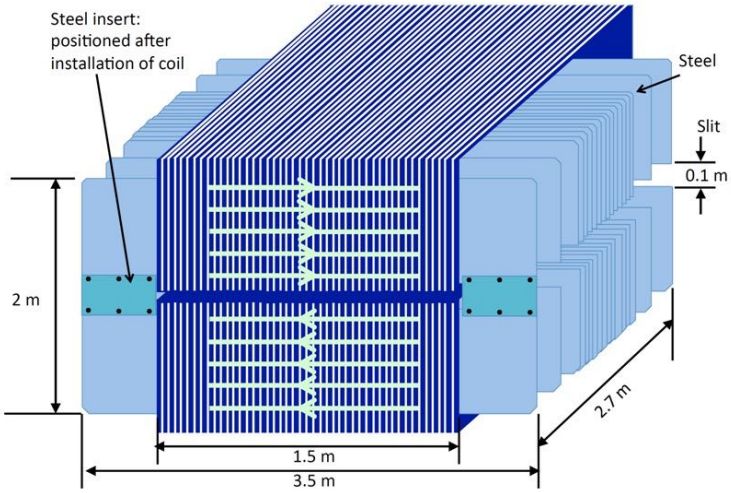

Figure 7.5: Schematic view of the magnet

Appendix A

Flux and background measurement at the candidate site

In WAGASCI experiment, the main background is considered to be particles generated in neutrino interactions with the wall of the detector hall. However, it is difficult to simulate precisely because the structure and composition of the wall, floor and other materials outside of the detector are much complicated. For a precise understanding of them, we measure the muons produced by the hall at the candidate site of WAGASCI by using INGRID [16]. The Monte Carlo simulation of the WAGASCI is based on that of the INGRID and the neutrino events on INGRID are also compared with the expectation of the MC simulation to check the reliability of the simulation.

A.1 INGRID

INGRID is composed of 16 modules [16]. One module is composed of a sandwich structure of 9 iron plates and 11 plastic scintillator trackers, as shown in Fig. 1.4. The scintillator tracker consist of two scintillator layers and each layer has 24 INGRID-type scintillator bars. Neutrino interaction on iron and wall is distinguished by using the most upstream scintillator tracker and side veto trackers around irons. We moved one of them to the candidate site of WAGASCI, as shown in Fig. A.1.

In the Monte Carlo simulation, irons, scintillators and hall are simulated in the same way as WAGASCI. The only difference is the parameters of the MPPC because the new low-noise MPPCs are used in the WAGASCI and old type MPPCs are used in INGRID. Neutrino interaction points are assumed

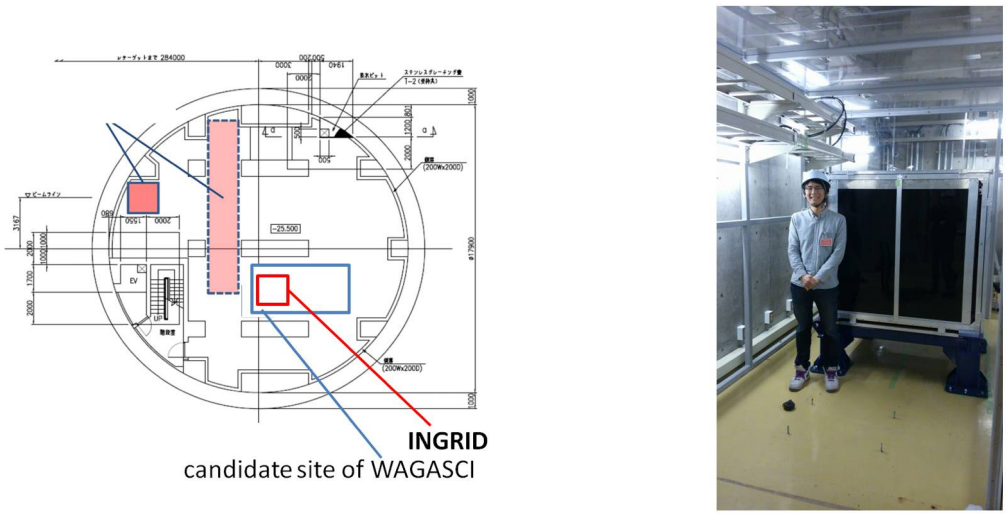

Figure A.1: The place INGRID is moved to (left) and a picture of the moved module (right).

on the iron, scintillator trackers in INGRID, wall, floor and pillar of the hall same as the case of WAGASCI.

The analysis method of INGRID is similar to that of the WAGASCI. The flow of the event selection is as follows:

1. Time clustering
2. Number of active planes selection
3. Two-dimensional track reconstruction
4. Three-dimensional track reconstruction
5. Vertexing
6. Beam timing cut
7. Veto cut
8. Fiducial volume cut

A.2 Data taking

Table A.1 shows the summary of the data set.

Table A.1: Summary of the data set

Period	2014/5/21∼6/3
Number of delivered spills	248875
Number of accumulated POT	2.01×10^{19}
Horn current	250kW

A.3 Comparison between data and simulation

Table A.2 shows the summary of the event selection with each cut and the expectation by the simulation. The number of events after the fiducial cut is consistent with the prediction of the simulation within 5 %. However, the number of events which hit front veto is 1.52 times bigger than the prediction of the simulation. This is because of the incomplete simulation of the hall. To reduce this difference, the total number of events on pillar,wall and floor is tuned by factor 1.52. Table A.3 shows the summary of the event selection after the normalization. The number of events which hit side veto planes is also consistent with the simulation by this tuning.

Table A.2: Summary of the event selection

Selection	data	MC(irons and scintillators)	MC(wall,floor,pillar)	MC(all)
Beam timing	32473	11069.1	pillar 75.5 wall 11133.1 floor 2438.7	24389.9
Veto cut	12977	10250.7	pillar 13.5 wall 1175.8 floor 243.7	11683.8
Fiducial cut	8095	7748.2	pillar 4.4 wall 99.5 floor 10.9	7863.1
Front veto	16988	650.5	pillar 11.6 wall 9027.3 floor 1445.2	11136.8
Side veto	2508	167.8	pillar 50.4 wall 930.0 floor 421.0	1569.3

Table A.3: Summary of the event selection after normalization of BG

Selection	data	MC(irons and scintillators)	MC(wall,floor,pillar)	MC(all)
Beam timing	32473	11069.1	pillar 117.6 wall 17345.2 floor 3799.7	31822.7
Veto cut	12977	10250.7	pillar 21.0 wall 1831.8 floor 379.6	12483.4
Fiducial cut	8095	7748.2	pillar 6.8 wall 155.0 floor 16.9	7927.2
Front veto	16988	650.5	pillar 18.0 wall 14064.3 floor 2254.7	16988.0
Side veto	2508	167.8	pillar 78.5 wall 1448.9 floor 655.9	2351.3

The vertex and angular distributions from the data are also compared with the simulation with each cut after the normalization of the BG. Figure A.2 and A.3 show the vertex distribution after beam timing cut, veto cut and fiducial cut. These vertex distribution is almost consistent with the simulation within the statistical error[1]. Figure A.3 also shows the angular distribution after the fiducial cut. It is consistent with the simulation. The neutrino interaction on irons and scintillators are simulated well at the candidate site.

Figure A.4 (A.5) shows the vertex and angular distribution of events which hit the front (side) veto plane(s). In both cases, high angle events are more than the prediction of the simulation.

Figure A.6 (A.7) is the neutrino interaction points on the wall (floor) of the events which hit the veto planes of INGRID. To reduce the discrepancy, more precise setting of the hall and other materials outside of the detector are needed. There should be also uncertainty of neutrino flux and interaction cross section, not only modeling of hall.

[1]There is a discrepancy in plane 8 of the Vertex z after fiducial cut. This is also observed other INGRID modules. The reason is under investigation.

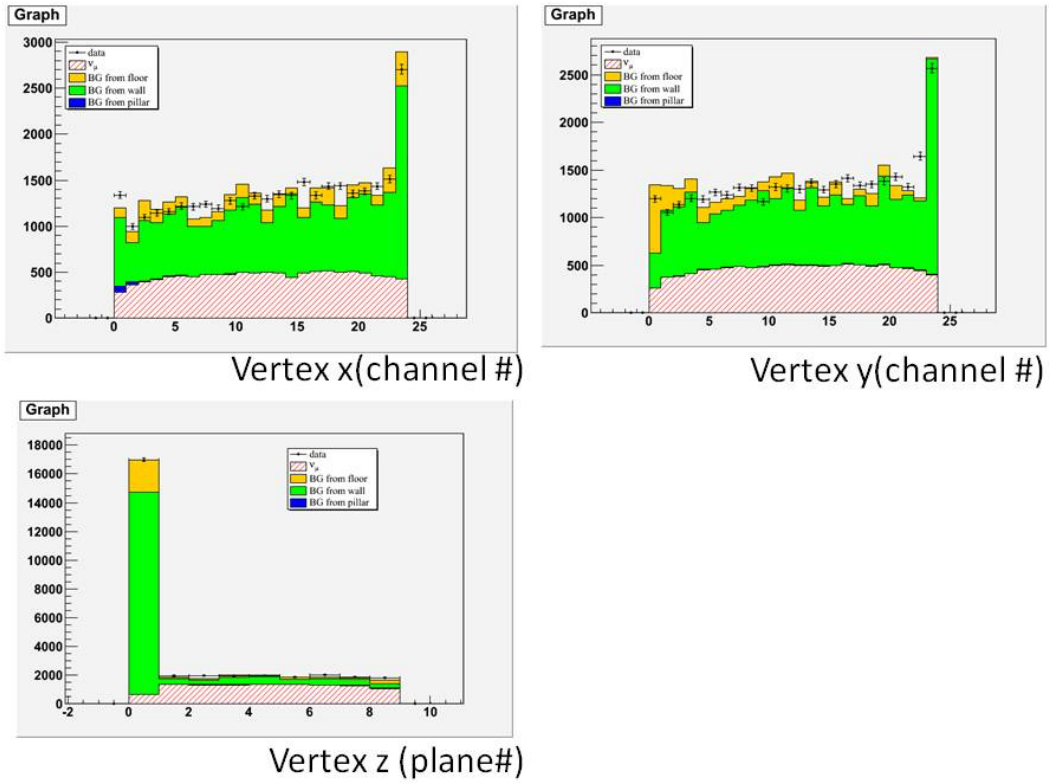

Figure A.2: Vertex x (upper left), y (upper right) and z (lower left) after beam timing cut

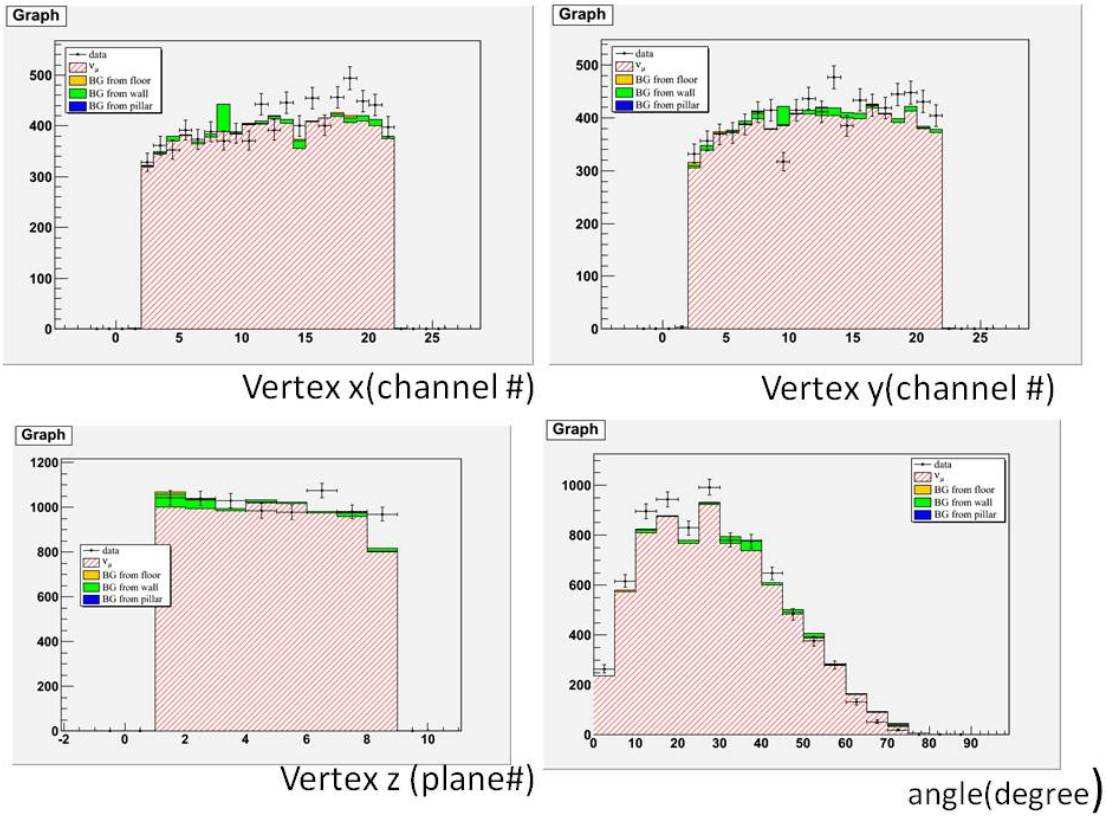

Figure A.3: Vertex x (upper left), y (upper right), z (lower left) and angle (lower right) after fiducial cut

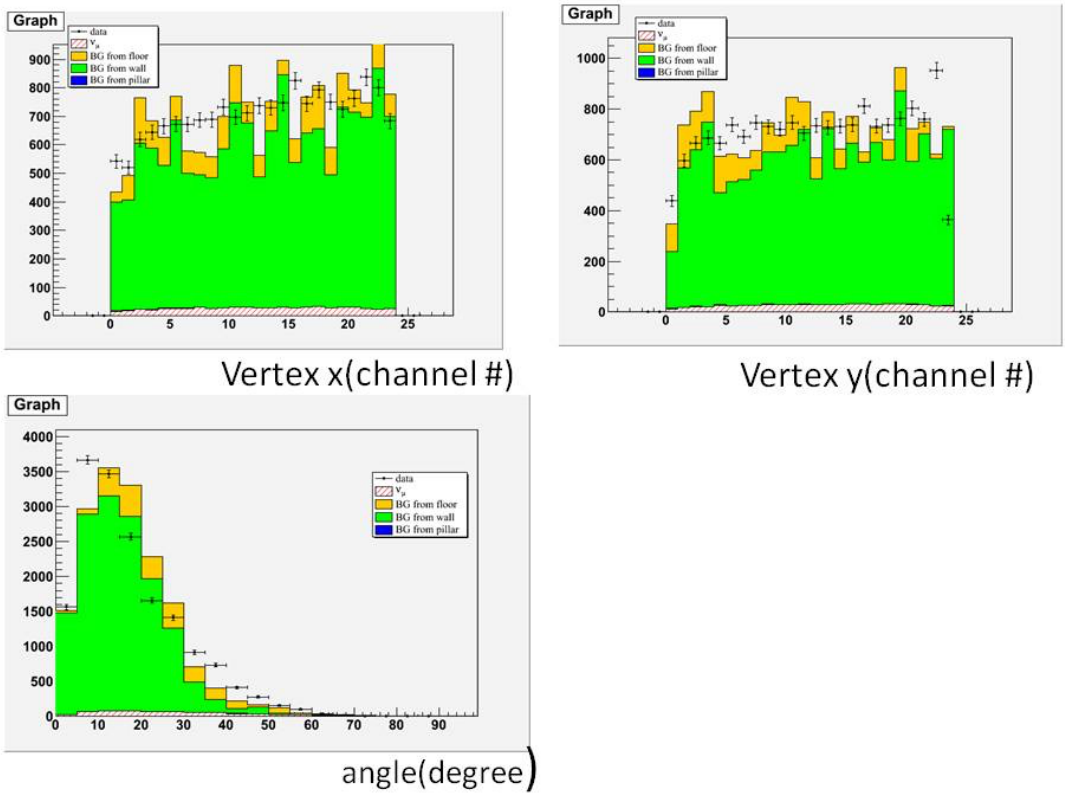

Figure A.4: Vertex x (upper left), y (upper right) and angle (lower left) of the events hitting the front veto plane

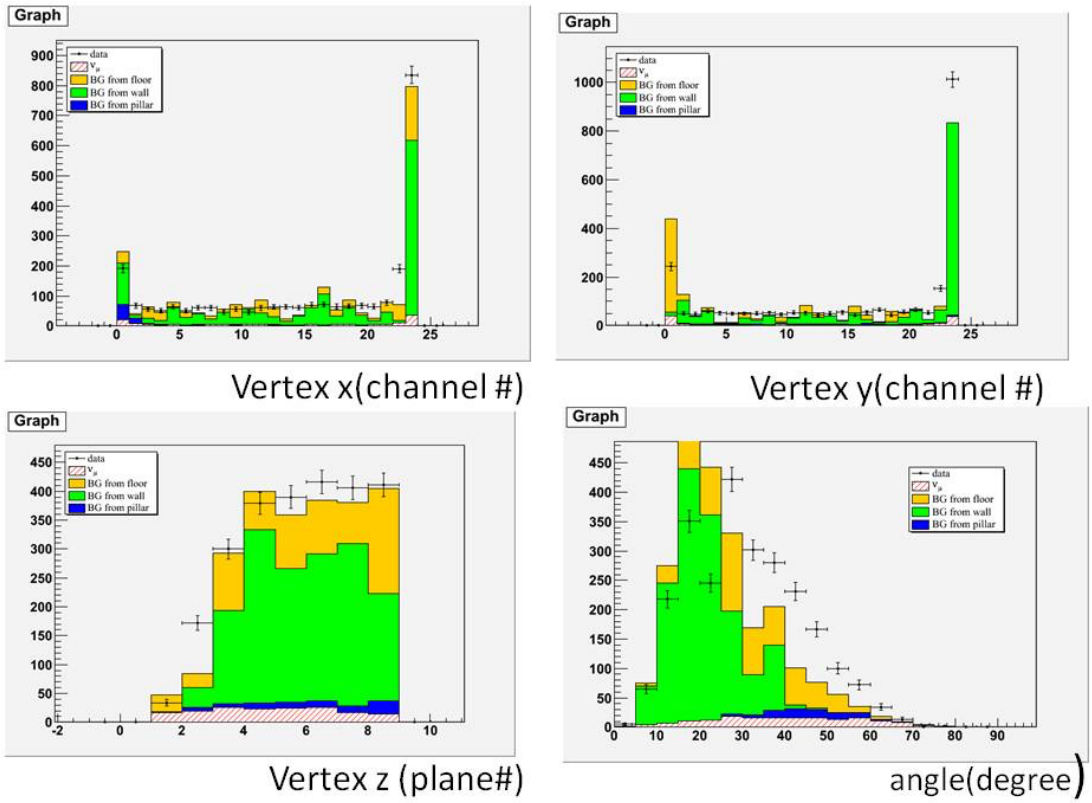

Figure A.5: Vertex x (upper left), y (upper right), z (lower left) and angle (lower right) of the events hitting the side veto planes

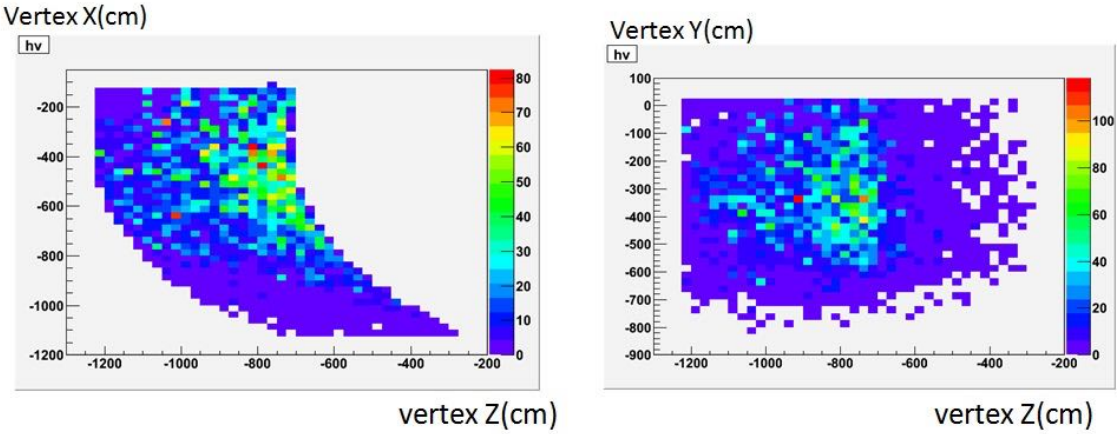

Figure A.6: True vertex x-z (left) and y-z (right) of the events which are produced inside the wall and hit the veto plane of the INGRID.

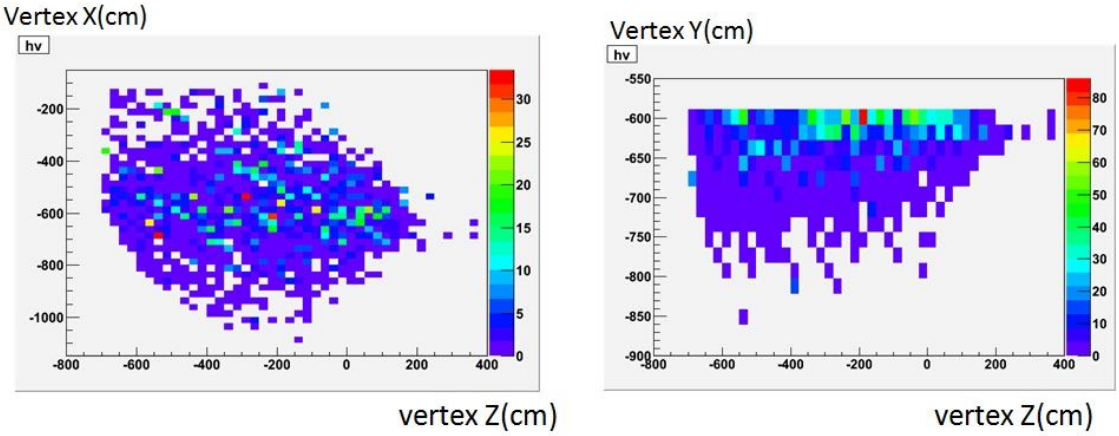

Figure A.7: True vertex x-z (left) and y-z (right) of the events which are produced inside the floor and hit the veto plane of the INGRID.

Appendix B

Performance test of the sample of the new MPPCs

We test and compare the older MPPC and two type of the new MPPC samples, produced in 2013 April, quantitatively. One is a normal, low noise and low afterpulse type and another is a crosstalk suppression type. The former has low dark noise rate and low afterpulse rate due to the improvement of the wafer. In addition, the crosstalk suppressed MPPC has lower crosstalk rate due to trench between the pixels, as shown in Fig. B.1. Table B.1 shows the list of the tested samples. Measurement item is as follows.

1. Gain
2. Dark noise rate
3. Crosstalk rate
4. Afterpulse rate
5. Crosstalk and afterpulse rate
6. Relative photo detection efficiency

Each measurements is done at 15°C, 20°C and 25°C to measure temperature dependency.

B.1 Gain

The gain of the MPPC is proportional to the bias voltage. The output charge of a pixel is given in the following equation.

Table B.1: List of tested samples

Kind of MPPC	Model unmber	Size of one pixel	Size of device
New MPPC (no crosstalk suppression)	S12571-050C	$50 \times 50 \mu m^2$	$1.0 \times 1.0\ mm^2$
New MPPC (with crosstalk suppression)	1X1MN50UMLCT-A	$50 \times 50 \mu m^2$	$1.0 \times 1.0\ mm^2$
Older MPPC	S10362-10-050C	$50 \times 50 \mu m^2$	$1.0 \times 1.0\ mm^2$

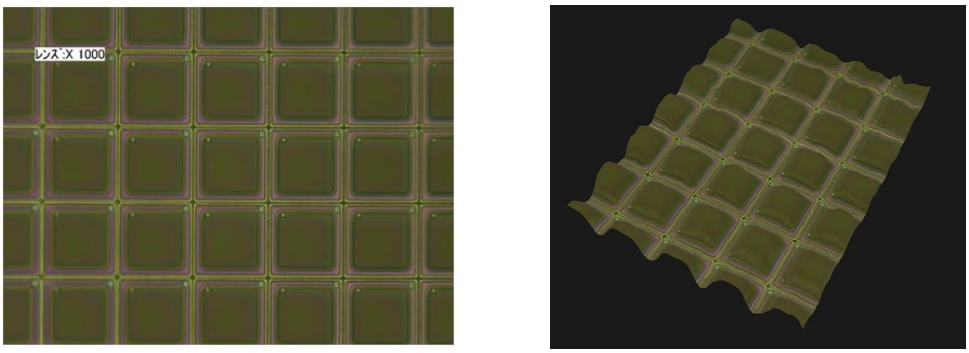

Figure B.1: View of the crosstalk suppression MPPC. There are trenches between the pixels to reduce crosstalk.

$$Q_{1p.e.} = C(V_{bias} - V_{bd}) \equiv C\Delta V \tag{B.1}$$

Here, C is a capacitance of a MPPC, V_{bias} is a bias voltage, V_{bd} is a break down voltage of a MPPC. We calculate the gain by measuring $Q_{1\ p.e.}$, which is calculated by the distance between pedestal peak and 1 p.e. peak as shown in Fig. B.2. ADC distribution is fitted by double Gaussian to measure the ADC value of the peaks. Figure B.3 shows the circuit for the measurement of gain and photo detection efficiency. We also measure the break down voltage and capacitance of the MPPCs by fitting the gain with a linear function of the bias voltage.

The result at 20°C is shown in Fig. B.4. The gain of new MPPCs is a little lower than that of the older MPPC with the same ΔV. New MPPCs have much wider operation voltage while keeping the linearity to ΔV. This is due to the reduction of the noise. Figure B.5 shows the measured gain at each temperature. Only breakdown voltage depends on temperature and there is no temperature dependency of gain as a function of ΔV. Table B.2 shows the summary of the capacitance and breakdown voltage measurement. New MPPCs have lower breakdown voltage. Temperature dependency is almost

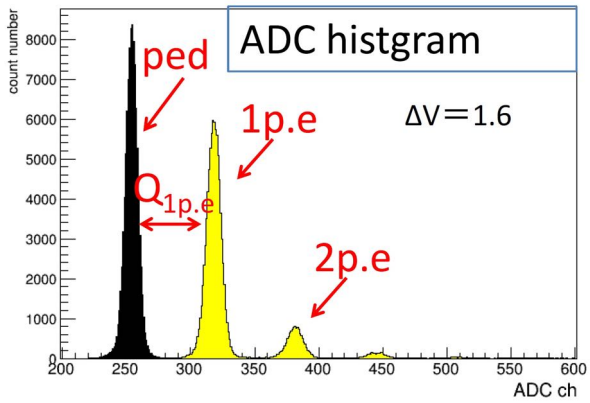

Figure B.2: A sample of the ADC histgram.

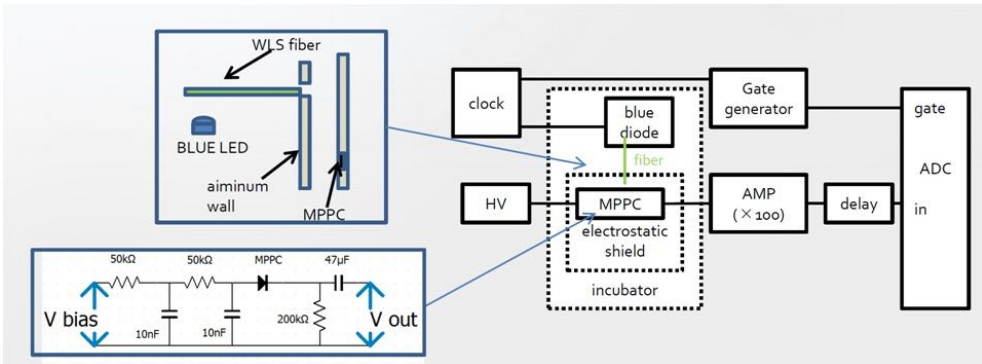

Figure B.3: A circuit for the measurement of gain and relative photo detection efficiency

the same between the old and new MPPCs.

B.2 Dark noise rate

The main source of the dark noise is thermal electrons and holes which makes avalanche multiplication. We measure dark noise rate by counting the number of pulses over 0.5 p.e. Used circuit for dark noise, afterpulse and crosstalk measurement is shown in Fig. B.6. To reduce the effect of the afterpulse, the counting is vetoed for $1\mu s$ just after counting a pulse.

Figure B.7 shows the measured dark noise rate in 20°C.[1] New MPPCs

[1]Noise rate seems to be linear function of ΔV. It is known to the possibility of the

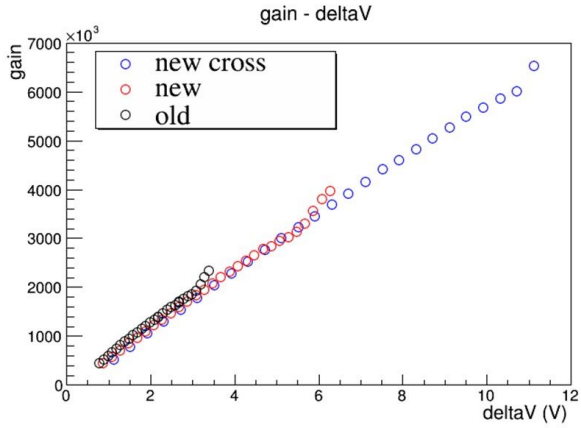

Figure B.4: Measured gain with each MPPC at 20°C.

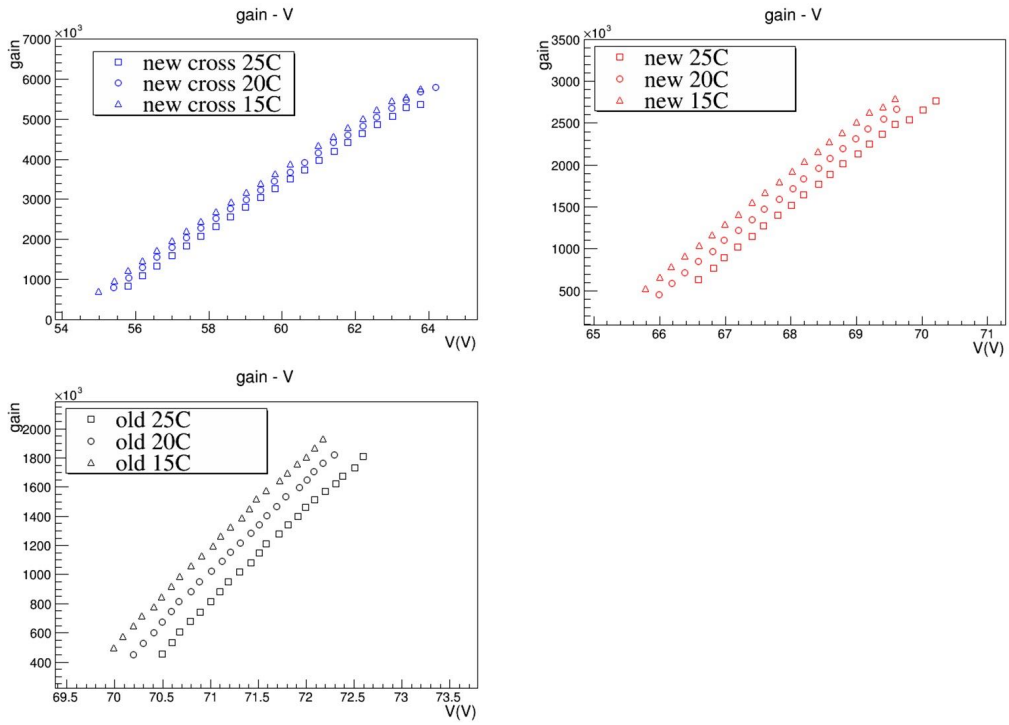

Figure B.5: Measured gain of the new MPPC with crosstalk suppression (left), with no crosstalk suppression (middle) and older MPPC (right) at each temperature. V is a bias voltage.

avalanche multiplication of a hole is also linear function of ΔV. On the other hand, that of an electron is not linear. Holes seem to be the reason of the dark noise.

Table B.2: Summary of the measured breakdown voltage and capacitance

Kind of MPPC	Temperature	Breakdown voltage(V)	$dV_{bd}/dT(V/°C)$	Capacitance(pF)
New MPPC (crosstalk suppression)	15°C	53.62 ± 0.04	0.065	93.32 ± 0.54
	20°C	53.89 ± 0.05		92.47 ± 0.70
	25°C	53.62 ± 0.03		93.64 ± 0.59
New MPPC (no crosstalk suppression)	15°C	64.76 ± 0.04	0.066	92.73 ± 1.13
	20°C	65.13 ± 0.03		94.47 ± 0.89
	25°C	65.42 ± 0.04		93.09 ± 1.15
Older MPPC	15°C	69.18 ± 0.02	0.054	104.1 ± 0.7
	20°C	69.42 ± 0.02		102.4 ± 0.9
	25°C	69.72 ± 0.02		102.0 ± 1.1

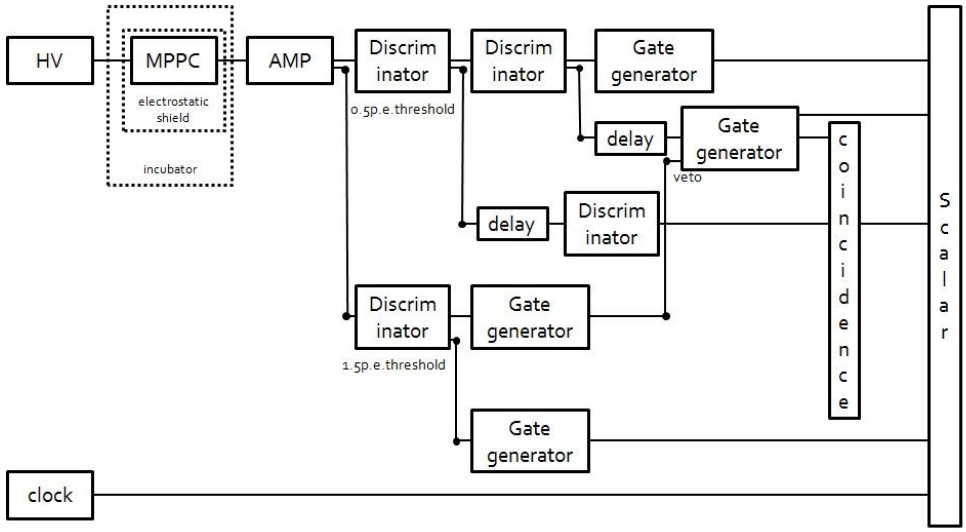

Figure B.6: A circuit for the measurement of dark noise rate, crosstalk rate and afterpulse rate

has about ten times lower dark noise rate compared with the old MPPC[2]. Figure B.8 shows the measured dark noise rate at each temperature. If the temperature increase, the dark noise rate increases compared with the same ΔV. This is because the number of the emitted thermal electrons increases due to the increase of temperature.

[2]We confirm that commercial version have more lower dark noise rate, as described in Chapter 4.

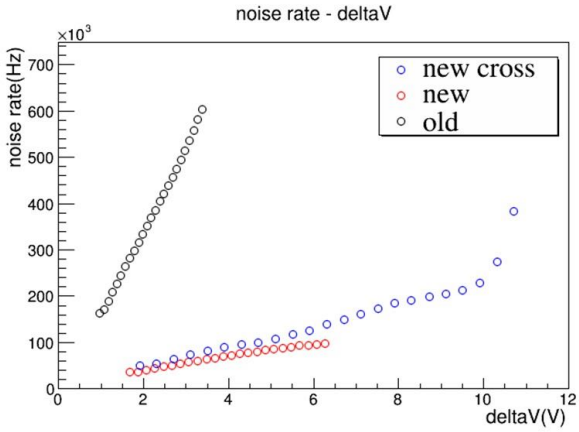

Figure B.7: Measured dark noise rate at 20°C with the new MPPC with crosstalk suppression (blue), with no crosstalk suppression (red) and older MPPC (black).

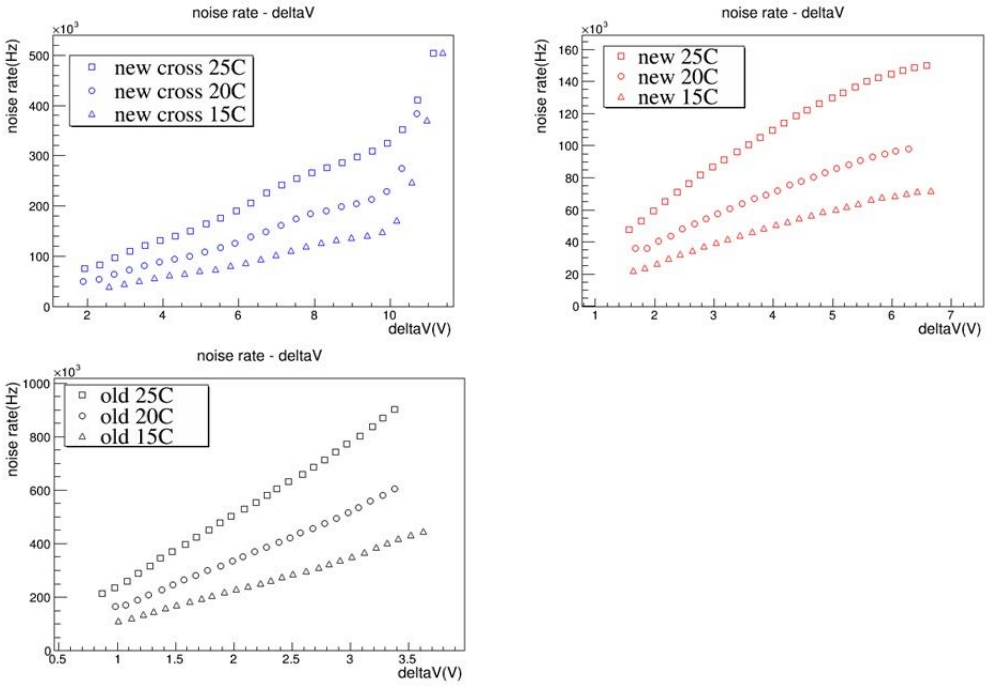

Figure B.8: Measured dark noise rate of the new MPPC with crosstalk suppression (left), with no crosstalk suppression (middle) and older MPPC (right) at each temperature.

B.3 Crosstalk rate

In an avalanche multiplication process, photons might be generated which are different from photons initially incident on an APD pixel. If those generated photons are detected by other pixels, then the MPPC output shows a value higher than the true value. We define crosstalk rate as following equation and measure it.

$$Crosstalk \equiv Darknoiserate_{1.5p.e.threshold}/Darknoiserate_{0.5p.e.threshold} \quad \text{(B.2)}$$

Figure B.9 shows the measured crosstalk rate at 20°C. The crosstalk rate of the crosstalk suppression version is much lower than that of no crosstalk suppression version. Figure B.10 shows the measured crosstalk rate at each temperature. There is no temperature dependency.

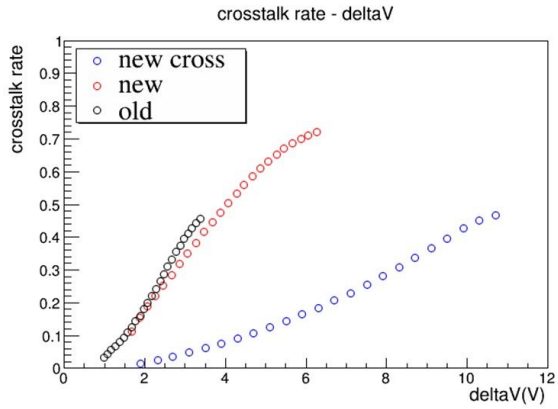

Figure B.9: Measured crosstalk rate in 20°C with the new MPPC with crosstalk suppression (blue), with no crosstalk suppression (red) and older MPPC (black).

B.4 Afterpulse rate

Afterpulses are spurious pulses following the true signal, which occur when the generated carriers are trapped by crystal or wafer and then released at a certain time delay. As shown in Figure B.11, we count the number of pulses inside 200ns gate after a 0.5p.e.–1.5p.e. pulse and define it as an afterpulse rate. Because the width of the discriminator is 20 ns, the afterpulses appear just after within 30ns from the originated pulse can not be measured in this

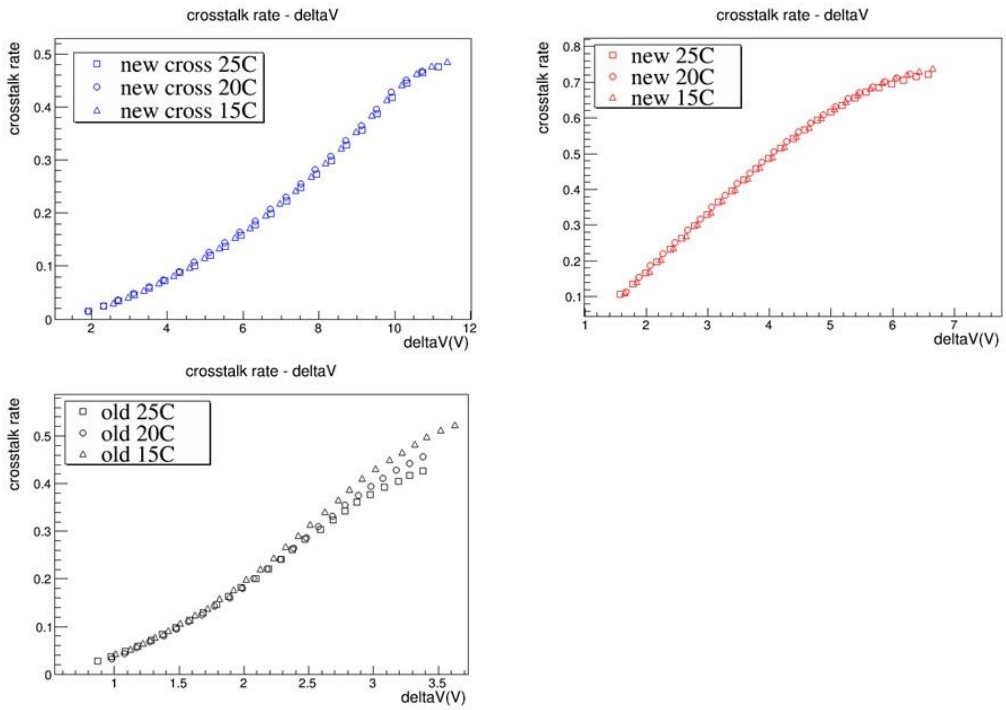

Figure B.10: Measured crosstalk rate of the new MPPC with crosstalk suppression (left), with no crosstalk suppression (middle) and older MPPC (right) at each temperature.

measurement. The effect of the dark noise is subtracted by the assumption of the Poisson distribution and the result of the dark noise rate measurement.

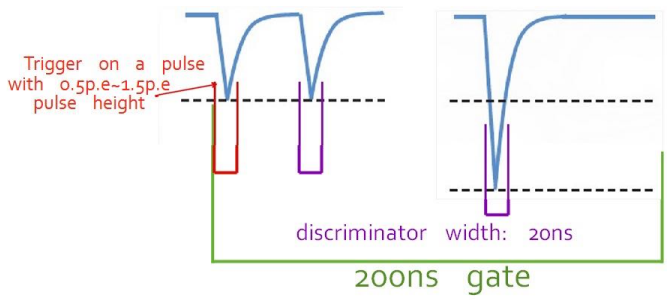

Figure B.11: Afterpulse measurement

Figure B.12 shows the measured afterpulse rate at 20°C.[3] The afterpulse

[3]That of old MPPC and crosstalk suppression MPPC seems to be the function of ΔV^2. This is because a probability of the avalanche multiplication is proportional to ΔV and

rate of the new MPPCs is much lower than that of old MPPC. That of new MPPC with no crosstalk suppression is very low and can not be measured correctly by this measurement. Figure B.13 shows the measured afterpulse rate at each temperature. There is a slight dependency of the temperature.

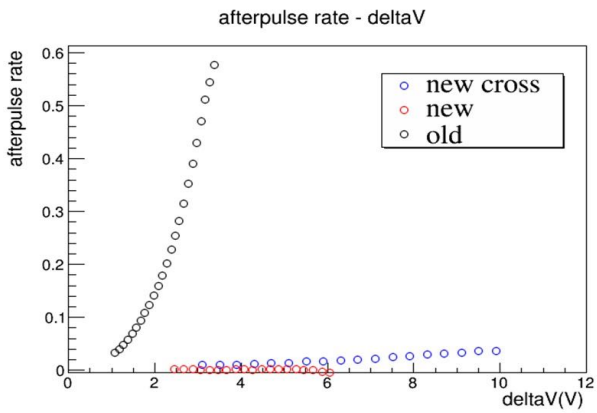

Figure B.12: Measured afterpulse rate at 20°C with the new MPPC with crosstalk suppression (blue), with no crosstalk suppression (red) and older MPPC (black).

B.5 Photo detection efficiency

We measure light yield from a wavelength shifting fiber to measure relative photo detection efficiency. To get uniform light, we use an aluminum wall which works as a defuser. The mean light yield is calculated by the assumption of the Poisson distribution as follows.

$$Crosstalk \equiv Darknoiserate_{1.5p.e.threshold}/Darknoiserate_{0.5p.e.threshold} \quad \text{(B.3)}$$

This is to reduce the effect of the crosstalk and afterpulses. The effect of the dark noise is also subtracted. We define the unit of relative photo detection efficiency as that of older MPPC with ΔV=1V.

Figure B.14 shows the measured relative photo detection efficiency at 20°C. New MPPC with no crosstalk suppression seems to have lower photo detection efficiency compared with old MPPC with the same ΔV. This is because the difference of the gain with the same ΔV. With the same gain,

the number of produced carriers also proportional to ΔV.

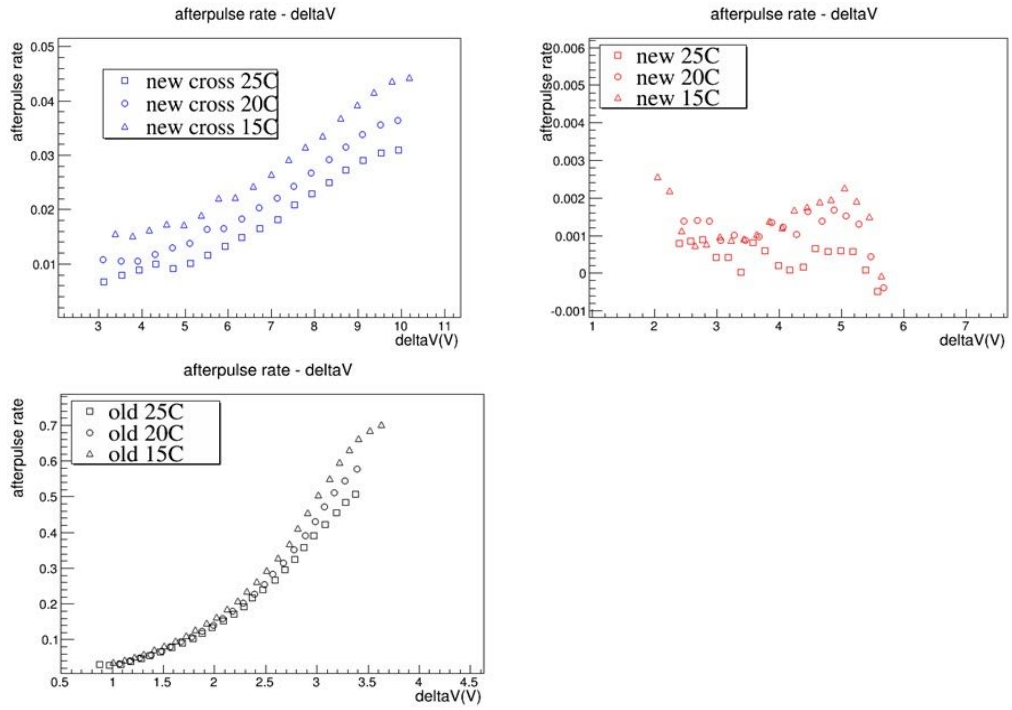

Figure B.13: Measured afterpulse rate of the new MPPC with crosstalk suppression (left), with no crosstalk suppression (middle) and older MPPC (right) at each temperature.

the new MPPC have the photo detection efficiency same as the old MPPC, as shown in Fig. B.14. That of the crosstalk suppression MPPC is about 15 % lower than that of other MPPCs with the same ΔV due to the trench which reduces the effective area.[4] Figure B.15 shows the measured afterpulse rate at each temperature. There is no temperature dependency.

B.6 Comparison of performance

Table B.3 shows the summary of the comparison of the performance in each MPPCs with appropriate bias voltages. We compare the cross suppression MPPC with the older MPPC and confirm that the noise rate of the former is 3 times lower, crosstalk rate of the former is same, afterpulse rate of the former is 4 times lower and photo detection efficiency of the former is twice. The crosstalk suppression MPPC satisfy the requirements of WAGASCI and

[4]We confirm that commercial version have no effect of the trench for photo detection efficiency.

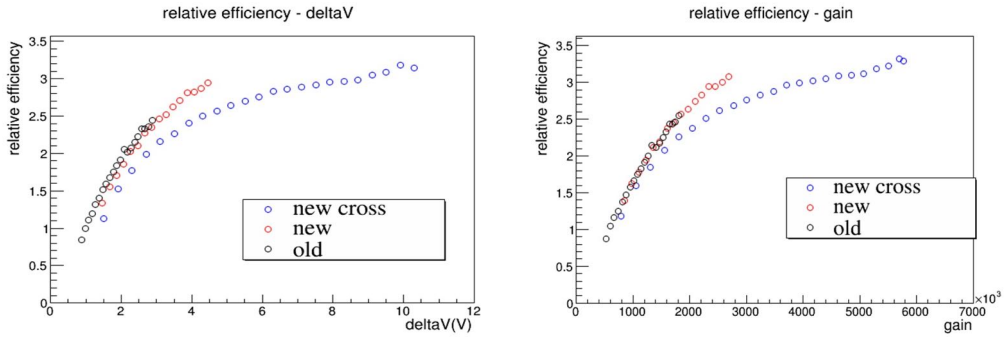

Figure B.14: Measured relative photo detection efficiency as a function of ΔV (left) and gain (right) at 20°C with the new MPPC with crosstalk suppression (blue), with no crosstalk suppression (red) and older MPPC (black).

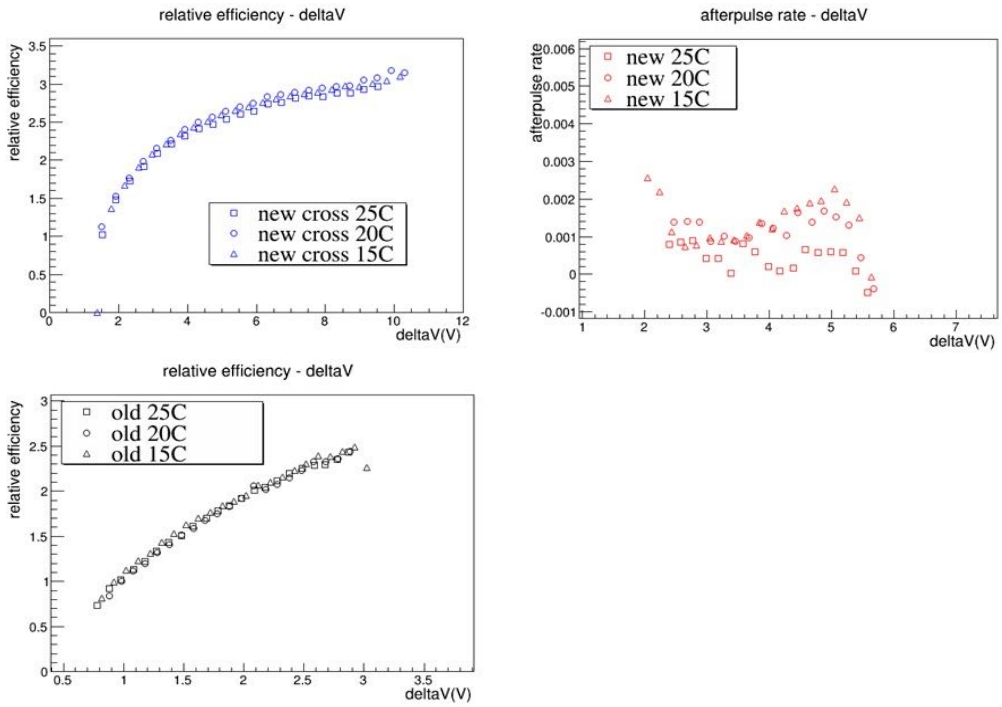

Figure B.15: Measured photo detection efficiency of the new MPPC with crosstalk suppression (left), with no crosstalk suppression (middle) and older MPPC (right) at each temperature.

we decide to use it. For the commercial version improved in December 2014, we confirm especially crosstalk rate is much more improved.

Table B.3: Summary of the comparison of the performance at 20°C.

Kind of MPPCs	New MPPC (crosstalk suppression) ΔV=3.0V	New MPPC (no crosstalk suppression) ΔV=3.0V	Older MPPC ΔV=1.2V
Gain	1.7×10^5	1.8×10^6	6.0×10^5
Dark noise rate (Hz)	7.0×10^4	5.7×10^4	1.9×10^5
Crosstalk rate	0.045	0.34	0.055
Afterpulse rate	0.010	<0.005	0.040
Relative photo detection efficiency	2.1	2.4	1.2

Bibliography

[1] Y. Fukuda *et al.* [Super-Kamiokande Collaboration], Phys. Rev. Lett. **81**, 1562 (1998) [hep-ex/9807003].

[2] Z. Maki, M. Nakagawa and S. Sakata, Prog. Theor. Phys. **28**, 870 (1962).

[3] K. A. Olive *et al.* (Particle Data Group), Chin. Phys. C, 38, 090001 (2014).

[4] A. Gando *et al.* [KamLAND Collaboration], Phys. Rev. D **88**, no. 3, 033001 (2013) [arXiv:1303.4667 [hep-ex]].

[5] K. Abe *et al.* [Super-Kamiokande Collaboration], Phys. Rev. Lett. **97**, 171801 (2006) [hep-ex/0607059].

[6] P. Adamson *et al.* [MINOS Collaboration], Phys. Rev. Lett. **112**, 191801 (2014) [arXiv:1403.0867 [hep-ex]].

[7] K. Abe *et al.* [T2K Collaboration], Phys. Rev. Lett. **112**, no. 18, 181801 (2014) [arXiv:1403.1532 [hep-ex]].

[8] F. P. An *et al.* [Daya Bay Collaboration], Phys. Rev. Lett. **112**, 061801 (2014) [arXiv:1310.6732 [hep-ex]].

[9] Y. Abe *et al.* [Double Chooz Collaboration], JHEP **1410**, 86 (2014) [arXiv:1406.7763 [hep-ex]].

[10] J. K. Ahn *et al.* [RENO Collaboration], Phys. Rev. Lett. **108**, 191802 (2012) [arXiv:1204.0626 [hep-ex]].

[11] K. Abe *et al.* [T2K Collaboration], Phys. Rev. Lett. **112**, 061802 (2014) [arXiv:1311.4750 [hep-ex]].

[12] K. Abe *et al.* [T2K Collaboration], Phys. Rev. Lett. **107**, 041801 (2011) [arXiv:1106.2822 [hep-ex]].

[13] K. Abe *et al.* [T2K Collaboration], Nucl. Instrum. Meth. A **659**, 106 (2011) [arXiv:1106.1238 [physics.ins-det]].

[14] K. Abe *et al.* [T2K Collaboration], Phys. Rev. D **88**, no. 3, 032002 (2013) [arXiv:1304.0841 [hep-ex]].

[15] Yoshinari Hayato,
Seminar of neutrino interaction with nucleus and their simulation,
http://www-he.scphys.kyoto-u.ac.jp/nufrontier/files/hayato-20140111.pdf

[16] K. Abe *et al.* [T2K Collaboration], Phys. Rev. D **90**, no. 5, 052010 (2014) [arXiv:1407.4256 [hep-ex]].

[17] K. Abe *et al.* [T2K Collaboration], Nuclear Instruments and Methods in Physics Research, A 659 (2011) 106–135

[18] Y. Fukuda *et al.* [Super-Kamiokande Collaboration], Nucl. Instrum. Meth. A **501**, 418 (2003).

[19] T2K.org (http://www.t2k.org/)

[20] K. Ieki, doctor thesis, Kyoto University (2014)

[21] C. Andreopoulosa *et al.* T2K technical note 175

[22] O.Benhar, N. Farina, H. Nakamura, M. Sakuda, R. Seki. Phys. Rev. D **72**, 053005 (2005)

[23] Andrew.P. Furmanski T2K technical note 184

[24] K. Abe *et al.* [T2K collaboration], Phys. Rev. D **87**, 012001 (2013)

[25] Y. Hayato, Acta Phys. Polon. B **40**, 2477 (2009).

[26] S. Agostinelli *et al.*, Nuclear Instruments and Methods in Physics Research A **506**, 250-303 (2003).

[27] Hamamatsu Photonics data sheet,
http://www.hamamatsu.com/resources/pdf/ssd/s12571-025_etc_kapd1042e.pdf

[28] Kuraray Co. Scintillator Fiber Products (1994)

[29] Research Center for Electron Positron Science, Tohoku University,
http://www.lns.tohoku.ac.jp/fy2011/home/pamphlet/e2010.pdf

[30] P. de Perio, T2K technical note 113

[31] http://omega.in2p3.fr/index.php/products/spiroc.html